DESIGN AND VALIDATION OF AN LED-BASED SOLAR SIMULATOR FOR SOLAR CELL AND THERMAL TESTING

A Thesis

presented to

the Faculty of California Polytechnic State University,

San Luis Obispo

In Partial Fulfillment

of the Requirements for the Degree

Master of Science in Aerospace Engineering

by

Matthew J. Gunther

December 2020

COMMITTEE MEMBERSHIP

TITLE: Design and Validation of an LED-Based Solar Simulator for Solar Cell and Thermal Testing

AUTHOR: Matthew J. Gunther

DATE SUBMITTED: December 2020

COMMITTEE CHAIR: Kira Abercromby, Ph.D.
Professor of Aerospace Engineering

COMMITTEE MEMBER: Amelia Greig, Ph.D.
Assistant Professor of Mechanical Engineering
Center for Space Exploration and Technology Research (cSETR)
The University of Texas at El Paso

COMMITTEE MEMBER: Eric Mehiel, Ph.D.
Associate Dean, College of Engineering

COMMITTEE MEMBER: Daniel Wait
Lecturer, Aerospace Engineering

ABSTRACT

Design and Validation of an LED-Based Solar Simulator for Solar Cell and Thermal Testing

Matthew J. Gunther

An LED-based solar simulator has been designed, constructed, and qualified under ASTM standards for use in the Cal Poly Space Environments Laboratory. The availability of this simulator will enhance the capability of undergraduate students to evaluate solar cell and thermal coating performance, and offers further research opportunities. The requirements of ASTM E927-19 for solar simulators intended for photovoltaic cell testing were used primarily, supplemented by information from ASTM E491-73 for solar simulators intended for spacecraft thermal vacuum testing. Three main criteria were identified as design goals - spectral match ratio, spatial non-uniformity, and temporal instability. An electrical design for an LED-based simulator to satisfy these criteria was developed and implemented, making use of existing lab equipment where possible to minimize cost. The resulting simulator meets the minimum Class C spatial non-uniformity and Class C temporal instability requirements of ASTM E927-19, but falls short of the spectral match ratio needed for Class C in this category. This is shown to be due to a calibration issue that is easily amended via software. The simulator was used to conduct the same laboratory procedure for solar cell I-V curve testing as performed by undergraduate students, showing excellent promise as a course enhancement.

ACKNOWLEDGMENTS

Thanks to:

- Dr. Kira Abercromby, for her wisdom and support in conducting this research
- Dr. Amelia Greig, for approving this topic and continuing to support it from afar
- Dr. Pauline Faure, for the loan of soldering equipment to use at home in the course of the COVID-19 pandemic
- Brandon Goddard, for building and providing a desktop PC for dedicated control of the simulator
- My family, for nourishing my budding aerospace interests with sci-fi stories, LEGOs, and make-believe - your love and support made me who am I today
- Holley Shugart, for her endless love and patience as I've dealt with the stress of grad school
- Andrew Guenther, for uploading this template

TABLE OF CONTENTS

LIST OF TABLES

LIST OF FIGURES

Chapter 1

INTRODUCTION

Solar cell performance is integrated into the Cal Poly Aerospace Engineering Department's Space Environments courses, but is dependent on weather conditions affecting sunlight when measuring cell characteristics. The effects of surface coating on radiative heat absorption are taught by comparing different metal cylinders under sunlight, which is again dependent on the weather. The inclusion of a solar simulator in this laboratory would simplify the conduct of these courses and increase the accuracy of results obtained by students. In addition, the reliable light would open up research opportunities in solar cell and coverglass materials and design, in investigating the performance of MLI and thermal coatings, and in the simulation of non-Earth orbital conditions. Currently, heat input within the Space Environments Lab's vacuum chambers is limited to heat plates, which do not extend beyond conduction and IR. In contrast, heat loads from incident solar radiation in the ultraviolet (UV) and visual portions of the spectrum are prominent in the space environment. Previously, the inclusion of solar simulators in the aerospace department's vacuum chamber laboratory has been prohibited by the high costs of commercial simulators.

This work adapts the general design principles of Kim et. al. in [26] and Bazzi et. al. in [9] to Cal Poly's Space Environments Lab. The desired cost is less than $1000, achieved by utilizing spare equipment and identifying low cost components. In particularly, advantage has been taken of improvements in LED technology that make this light source both cheap and reliable in comparison to costly arc lamps.

Chapter 2

BACKGROUND

2.1 Radiation Physics

As befits a work focused on solar irradiation, the various quantities of radiant energy transfer are used throughout. They are defined here for clarity and consistency. Table 2.1 provides the radiometric unit's name, its unit in the SI system, the symbol used to represent it in this work, its mathematical definition, and any other relevant equations. The variable conventions laid out in Koshel [29] have been followed herein.

Table 2.1: Radiometric Quantities

Name	Symbol	SI Unit	Definition	Other Expressions
Radiant Energy	Q	Joule J	$Q = \int \Phi \ dt$	
Radiant Flux (Power)	Φ or P	Watt $W = \frac{J}{s}$	$\Phi = \frac{dQ}{dt}$	$\Phi = \int E \cos\alpha \ dA$ $\Phi = \int I \ d\Omega$ $\Phi = \int \int L \cos\theta \ dA \ d\Omega$
Irradiance (Exitance)	E (M)	$\frac{W}{m^2}$	$E = \frac{d\Phi}{dA_{target}}$ $M = \frac{d\Phi}{dA_{source}}$	$E = \frac{I \cos\theta}{r^2}$ $E = \int L \cos\theta \ d\Omega$
Radiant Intensity	I	$\frac{W}{sr}$	$I = \frac{d\Phi}{d\Omega}$	$I = \int L \ dA$
Radiance	L	$\frac{W}{m^2 \ sr}$	$L = \frac{\partial^2 \Phi}{\partial\Omega \ \partial A_{proj}}$	
Solid Angle	Ω	Steradian sr	$d\Omega = \frac{dA_{sphere}}{r^2}$	$d\Omega = \sin\theta \ d\theta \ d\phi$ $\Omega = 4\pi \sin^2 \frac{\theta_0}{2}$

Energy in the form of electromagnetic waves propagates through space without requiring a medium. Power, or Flux, is the rate of energy transfer. Irradiance is the amount of power incident on a surface. Similarly, exitance is the amount of power

emitted from a surface. Solid angle, measured in steradians, is the three-dimensional counterpart to the standard two-dimensional angle. A measurement in steradians is defined by a conical shape. A hemisphere sweeps through 2π steradians; this is the solid angle visible from a point on a flat surface. Intensity is the amount of power emitted into or passing through a solid angle. Flux from a light source expands spherically as it travels through space. Consequentially, irradiance is inversely proportional to the square of the distance traveled. Intensity, however, remains constant. Radiance combines elements of both irradiance and intensity. Light sources emit electromagnetic radiation across their surface area, but also emit that radiation with an angular distribution. An expression for radiance is a function both of angular and spatial coordinates, defining a light source's emission characteristics in one statement.

Other quantities present in Table 2.1 are: incidence angle, α or θ; half-angle of a cone of solid angle Ω, θ_0; projected area, $A_{proj} = A\cos\theta$; area of a spherical cap subtended by a solid angle Ω, A_{sphere}; spherical coordinate system polar and azimuthal angles, θ and ϕ, respectively; and radius or distance, r.

Electromagnetic radiation is characterized either by its wavelength, λ, or its frequency, f, which are related to each other and the speed of light, c, by the wave equation,

$$c \;=\; f\lambda \tag{2.1}$$

The energy of a photon, Q, is given by the Planck-Einstein relation,

$$Q \;=\; hf \tag{2.2}$$

where h is Planck's constant. Thus, the higher a photon's energy, the higher its frequency of electromagnetic oscillation, and correspondingly the smaller its wavelength must be.

An ideal radiation emitter, or blackbody, emits thermal radiation in terms of radiance as described as a function of wavelength, λ, and temperature, T, by Planck's law,

$$L_{\lambda,b}(\lambda, T) = \frac{2hc^2}{\lambda^5(e^{\frac{hc}{\lambda k_B T}} - 1)} \tag{2.3}$$

where k_B is Boltzmann's constant [26]. Typically, this function is evaluated at a given temperature for a wide range of wavelengths, producing a spectral irradiance curve. Any quantity evaluated to show its variance with wavelength is called a spectral quantity, represented by appending a λ subscript to that quantity's symbol (i.e $L_{\lambda,b}$ for spectral radiance of a blackbody). Note that this adds a factor of m^{-1} to the units of a quantity evaluated in this fashion - $L_{\lambda,b}$ has units of $\frac{W}{m^3\ sr}$ instead of $\frac{W}{m^2\ sr}$.

Another useful form of Planck's Law results from manipulating Eq. 2.3 to give spectral radiant exitance instead of spectral radiance [6].

$$M_{\lambda,b}(\lambda, T) = \frac{2\pi hc^2}{\lambda^5(e^{\frac{hc}{\lambda k_B T}} - 1)} \tag{2.4}$$

Matter at room temperature emits thermal radiation primarily in the infrared region. At extremely hot temperatures (thousands of Kelvin) matter emits more and more of its thermal radiation at lower wavelengths, since this corresponds to higher energy photons. In this range, it emits a significant amount of energy in the visible spectrum of light. Since the temperature influences the perceived color (from red at lower temperatures to white at higher), the equivalent blackbody temperature is also called the color temperature.

2.2 The Sun

The Sun emits radiation similarly to a blackbody at 5800 K. The actual spectral irradiance of the sun compared to that of an ideal blackbody of this temperature calculated with Planck's Law (Equation 2.4) is shown in Figure 2.1. This spectral irradiance curve is that of sunlight in a vacuum, known as the air mass zero (AM0) spectrum. The data for Figure 2.1 is taken from ASTM standard E490-00a, and it is to this standard that the simulator design of this thesis has been compared. The standard is a compilation of measurements from satellite observatories [5].

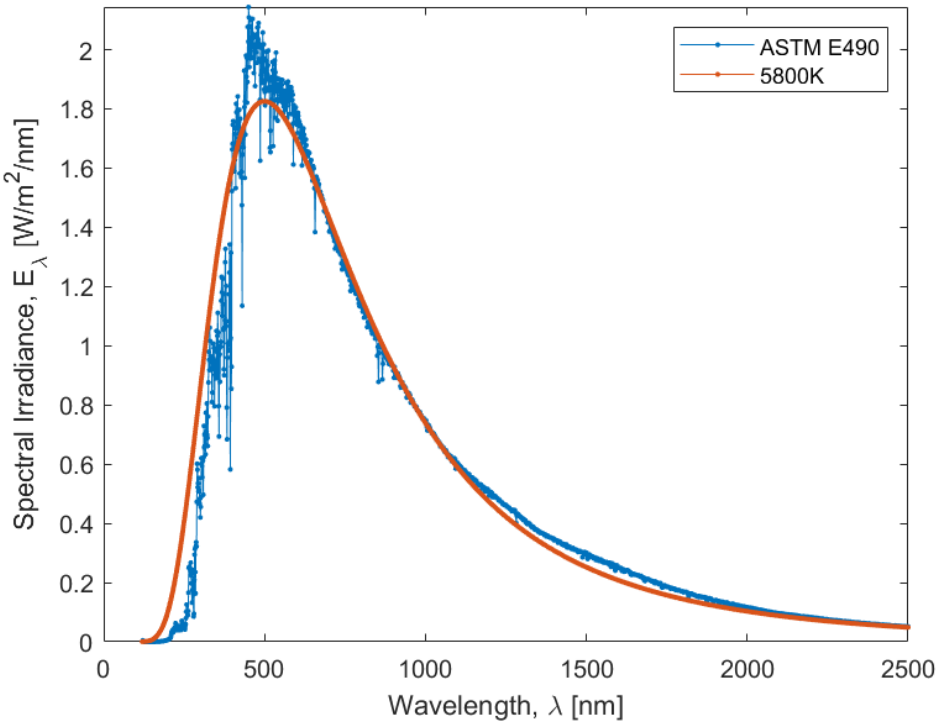

Figure 2.1: Comparison of ASTM E490 E_λ to a 5800K Blackbody [5]

Note that the exitance curve of a blackbody given by Equation 2.4 was scaled for Figure 2.1 by first converting to power by multiplying by the Sun's surface area, and then used to calculate irradiance at a distance from the Sun equal to Earth's average orbital radius (1 AU). The Sun's total power output is distributed across such a

large surface area at this distance that incident photons can be assumed perfectly collimated, and irradiance on a flat surface can be assumed constant. The total irradiance integrated over all wavelengths is 1366.1 $\frac{W}{m^2}$, and is known as the solar constant, represented by *S0* [5].

Sunlight that passes through Earth's atmosphere is attenuated, especially in specific absorption bands corresponding to different gases. Standards such as AM1.5 exist to describe the spectral characteristics of this light, and are used in the design of solar power farms on Earth's surface. The focus of this thesis is on the simulation of the space environment, so AM0 has been used as the target spectrum. However, calibration of the simulator and comparison to the lab's current solar cell testing procedure requires adjusting for the differences between the extraterrestrial and Earth surface spectrums.

2.3 Radiometric and Photometric Units

The terminology summarized in the previous section is that of radiometry, which defines and measures radiation based on its electromagnetic characteristics. Photometry focuses instead on the visual response of the human eye to radiation. As a consequence, photometry does not use units based on the Joule, but instead is based on the definition of the candela [29]. Radiometric and photometric units are distinguished by the use of an "e" subscript (i.e. Φ_e) to denote radiometric, and the use of a "v" subscript (i.e. Φ_v) to denote photometric. Additionally, the two systems can be distinguished by prefixing the quantity in question with "radiant" for radiometric and "luminous" for photometric units. A summary of the differing names is given in Table 2.2. The standards for qualifying solar simulators are defined in radiometric units, but due to the extremely large market for LEDs in interior and exterior

lighting fixtures, all LEDs that emit light in the visible portion of the spectrum use photometric units for their datasheet specifications. Thus, conversion between the two systems is a necessary step in the design of an LED-based solar simulator.

Table 2.2: Radiometric and Photometric Units [29]

Radiometric	**Photometric**	
Radiant Flux	Luminous Flux	lumen, $lm = cd\ sr$
Irradiance	Illuminance	lux, $lx = \frac{lm}{m^2}$
Radiant Intensity	Luminous Intensity	candela, $cd = \frac{lm}{sr}$
Radiance	Luminance	nit, $nt = \frac{lm}{m^2 sr}$

As per the SI standard [11], the candela, cd, is defined by setting the luminous efficacy of monochromatic radiation of frequency 540×10^{12} Hz to a constant $K_m = 683\ \frac{lm}{W}$, where the lumen, $lm = cd\ sr$. However, this conversion is only valid at the specified frequency. This corresponds to what the human eye perceives as green light, and it is to this frequency that the eye is most sensitive. The ISO and CIE jointly maintain a standard sensitivity curve for photopic, or color, vision, $V(\lambda)$ [14]. This is the curve with which conversions were made between lumens and Watts in this work, as it is valid for bright, sunlit conditions. It is depicted in Figure 2.2 using data from CIE S 010/E:2004 [14][27]. The $V(\lambda)$ curve is normalized to 1 at exactly 555 nm. However, $540 \times 10^{12}\ Hz \approx 555.17\ nm$, so instead of the exact value of $K_m = 683 \frac{lm}{W}$, the adjusted factor is 683.002. [14] states that the difference is immaterial in practical applications.

The equation to convert any spectral radiometric unit to its corresponding photometric quantity is given in [14], using flux as an example, as

$$\Phi_v = K_m \int_0^\infty \Phi_{e,\lambda}\ V(\lambda) d\lambda \tag{2.5}$$

Spectral quantities do not require the integration over wavelength, and use the conversion (again with flux as an example)

$$\Phi_{v,\lambda} = K_m \; \Phi_{e,\lambda} \; V(\lambda) \tag{2.6}$$

This second form is more easily rearranged to convert from photometric to radiometric units, and is conducive to the use of vector variables in Matlab.

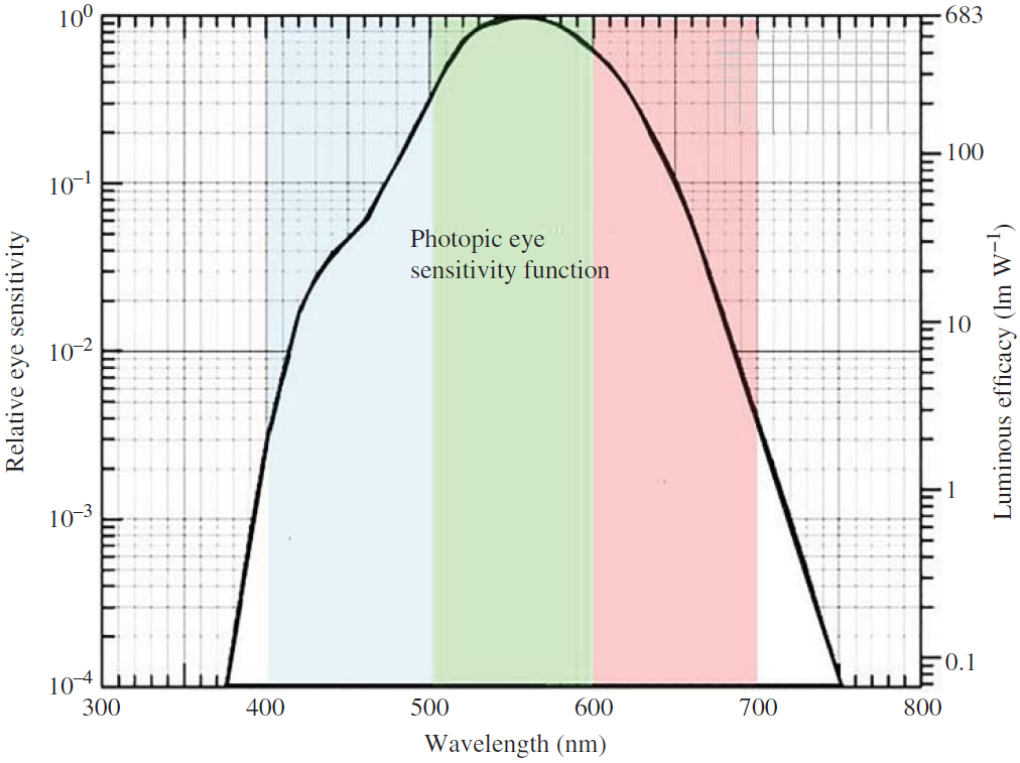

Figure 2.2: Photopic Eye Sensitivity Function, V_λ [27]

2.4 Optics and Étendue

The transfer efficiency, η, of an optical system is given by

$$\eta = \frac{\Phi_{source}}{\Phi_{target}} \tag{2.7}$$

In the field of heat transfer, this ratio is often called the view factor. Such calculations take advantage of the simplifying assumption that radiation is emitted diffusely, independently of angle, in order to equate the transfer efficiency to the geometric view factor, which can be computed for known surface shapes [47]. This geometric view factor is represented as $F_{i \to j}$, meaning the fraction of the field of view from a surface i that is subtended by another surface j. However, this equivalency breaks down when radiation is not emitted perfectly diffusely. Since LEDs emit directionally, and it is desirable to use spectrally reflective surfaces to maximize transfer efficiency, in this thesis transfer efficiency and geometric view factor cannot be equated [29].

An important quantity in optics is étendue [29], which is intimately related to solid angle and geometric view factor. Étendue is a French word roughly meaning "extent." Geometrical extent is sometimes used to refer to étendue. Étendue is defined as area multiplied by solid angle multiplied by the index of refraction squared, integrated over the entrance to an optical system [29]. It has units of $[m^2\ sr]$, and is represented by ξ:

$$\xi = n^2 \int \int \cos\theta \ dA \ d\Omega \tag{2.8}$$

Since it accounts for two spatial dimensions and two angular dimensions, it can be considered a volume in phase space [29]. The value of considering étendue is apparent from the definition of radiance. Since radiance is the derivative of flux with respect to surface area and solid angle, it can be equivalently stated that radiance is equal to the derivative of flux with respect to étendue: $L = n^2 \ \frac{\partial \Phi}{\partial \xi}$, where $d\xi = n^2 \ \int cos\theta \ dA \ d\Omega$. Correspondingly, flux can be calculated as $\Phi = \int \frac{L}{n^2} \ d\xi$.

It can be proven through multiple methods that étendue must be conserved for a lossless optical system [29]. In a real optical system, étendue can only increase, never decrease, as a consequence of increasing entropy. It can change form, however, which is the basis behind many optical devices. A light beam can be concentrated into a

smaller area while its angular spread increases, or a light beam can be collimated while increasing its spatial area. Sunlight at Earth's orbital distance from the Sun is nearly perfectly collimated, so it can be deduced that it is important to minimize the spatial area of the light source in a solar simulator, while also choosing sources which emit into as narrow a solid angle as possible. This minimizes the étendue entering the optical system, allowing leeway for imperfections in transferring collimated radiation to a target surface.

2.5 Theory of Solar Cell Operation

Solar cell testing is one of the primary purposes of the simulator designed herein. Predicting the performance of a cell under the simulator versus under actual sunlight is critical. Solar cells and photodiodes are nearly identical semiconductor devices. Solar cells have a larger surface area, intended to generate power, while photodiodes are smaller, intended for uses such as receiving optical signals. Both devices are composed of at least two semiconductor layers. When these two layers are sandwiched together, they create a p-n junction at their interface. Charges diffuse and equalize at this interface to create an area of zero net charge - the depletion region. An electric field is applied across this region due to the charges on either side. This electric field mobilizes charge transfer in the opposite direction of diffusion. The device behaves as a diode, such that an applied current can only overcome the depletion region from one direction [31], called the foward bias direction.

The operating principle of solar cells is that a current is generated when the semiconductor is bombarded with electromagnetic radiation. The absorption of a photon creates an electron-hole pair, as the electron gains enough energy from the photon to jump into a higher energy band, leaving behind a hole [27]. The current flows

in the reverse bias direction, opposite the direction that an applied current can pass through the depletion region. Intuitively this makes sense - if the photogenerated current could pass through the depletion region, it would result in an internal short circuit. But since it is blocked by the depletion region, the current can only flow through an external current loop. A solar cell can be electrically modeled as a current source in parallel with a diode. Inefficiencies can be modeled as a parallel shunt resistance, R_{SH}, and a series resistance, R_S, with whatever load the cell is connected to [31]. This model is shown in Figure 2.3.

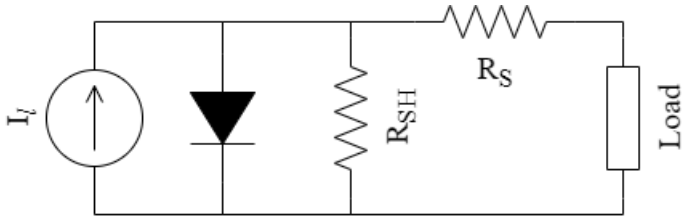

Figure 2.3: Simple Solar Cell Circuit Model

The total current out of the cell, I, is equal to the photogenerated current, I_l, minus the current across the diode and the current dissipated in the resistors. The diode current can be expressed with the Shockley diode equation, and the current dissipated in the resistors can be rewritten in terms of voltage and resistance, such that the governing solar cell current equation is [31]

$$I = I_l - I_0(e^{\frac{q(V+IR_S)}{nkT}} - 1) - \frac{V + IR_S}{R_{SH}} \tag{2.9}$$

where I_0 is the saturation current, q is the elementary charge, V is the voltage across the cell, n is the diode ideality factor, k is Boltzmann's constant, and T is the cell temperature. Saturation current, shunt resistance, and series resistance can be predicted based on the semiconductor base material, the doping elements, and geometry using solid state physics principles, but it is more common to experimentally determine these and other unknown parameters, such as the diode ideality factor, by

conducting an I-V sweep [31]. To conduct such a test, the semiconductor device is short-circuited, and then either voltage or current is measured while varying the other under constant illumination, allowing the unknowns to be determined with nonlinear regression. This constant illumination requirement is a motivation to use a solar simulator with known output characteristics.

The remaining unknown that is not determined by such a sweep is the dependence of I_l on the incident radiation characteristics. The total photogenerated current can be found from the spectral response, SR, in generated current per incident radiant flux $[\frac{A}{W}]$, which is a function of wavelength [31]. An example of a spectral response curve is given in Figure 2.4.The spectral response is closely related to the external quantum efficiency, EQE, which is the likelihood that an incident photon will create an electron-hole pair based on its wavelength [31], measured in $[\frac{electrons}{photon}]$:

$$EQE \ = \ \frac{hc}{q\lambda} SR \ = \%1239.8 \frac{SR}{\lambda} \% \tag{2.10}$$

where h is Planck's constant in $[\frac{m^2 kg}{s}]$, c is the speed of light in $[\frac{m}{s}]$, and q is the elementary charge in $[C]$.

Ultimately, the knowledge of a cell's spectral response curve combined with the knowledge of a solar simulator's spectral power curve allows the prediction of how much current will be generated under test conditions. Conduction of a test with knowledge of one of these curves allows the inference of information about the other. A known solar cell can be used to test the spectral power curve of an unknown simulator. After determining its spectral power curve, the simulator can then be used to test solar cells with unknown spectral response curves. This process is integral to the validation of the simulator presented herein.

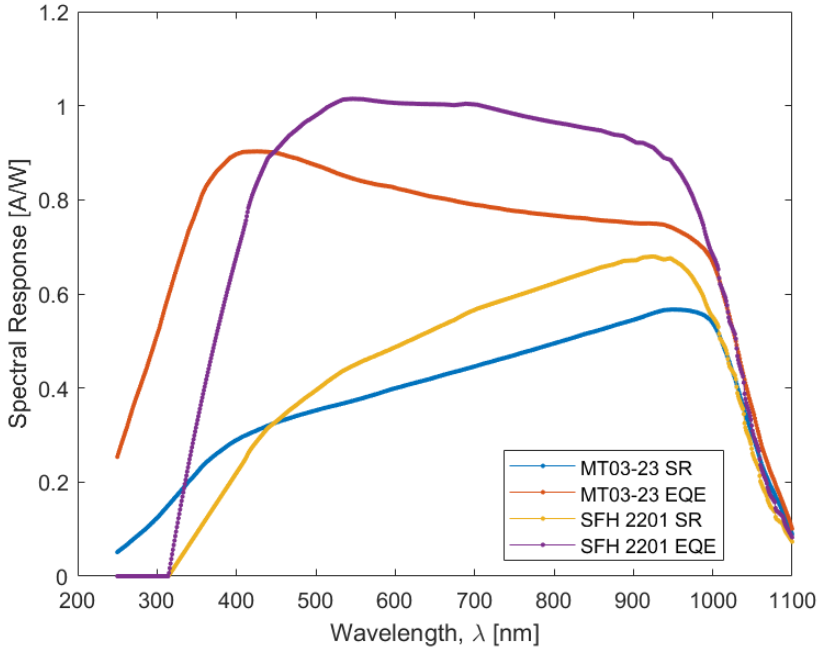

Figure 2.4: Photodiode SR and EQE Curves [41][51]

2.6 Role of Thermal Vacuum Testing in Spacecraft Design

For space applications, the effect of incident solar radiation is not limited to power generation via solar cells and arrays. In the spectral response curve of Figure 2.4 above, the drop-off at low wavelengths in spectral response curves represents photon energy in excess of the p-n junction's band gap being converted to heat through electron thermalization, while the drop-off at high wavelengths represents absorbed photons with lower energy than the band gap producing heat rather than useful current. Solar arrays tend to absorb large quantities of heat as a result. The cells heat up to extremely high temperatures, decreasing their efficiency. The development of appropriate coatings and materials to both prevent heat absorption and to emit heat is central to space power engineering.

Testing such materials and their integration into spacecraft is the realm of thermal vacuum testing. Two typical tests are thermal cycling and thermal equilibrium.

Thermal cycling is used to test the adequacy of a thermal control system to regular sunlight-eclipse cycles, such as those seen by spacecraft in low Earth orbit. Thermal equilibrium testing is used to represent the thermal environment seen by satellites in higher Earth orbits, with rare eclipses, and in interplanetary orbits. In all cases, the goal is the accurate representation of the space environment.

The thermal space environment is dominated by solar radiation. Other factors are the radiation emitted by the spacecraft, the background radiation environment of deep space, and, within proximity to a planet or other body, the albedo of reflected sunlight and the blackbody radiation of the body itself. Heat rejection of a spacecraft surface can be effectively modeled by heating the component in a vacuum to its expected on-orbit temperature, and surrounding it in a cryogenically cooled shroud to model the absorptive characteristics of deep space. For this purpose, adding heat with simple resistive elements is usually adequate. In order to assess the thermal equilibrium of a spacecraft or thermal control system, it is important to calculate the predicted rate of heat absorbed from solar radiation, and match this rate with the rate of heat input from resistive heating elements. However, to experimentally verify the heat absorption characteristics of a system, resistive heating elements introduce a test-like-you-fly exception, and the solar radiation input should be simulated if low error is required. A facility equipped with a solar simulator can make use of it to increase the accuracy of the previous testing schemes.

Chapter 3

OVERVIEW OF SOLAR SIMULATION TECHNOLOGY

Roughly equivalent international standards have been established for the classification of solar simulators by the International Organization for Standardization (ISO), ASTM International, Japanese Industrial Standards (JIS), and the International Electrotechnical Commission (IEC). ASTM standards are available to Cal Poly students through the university library, and have been used in past projects in the Space Environments Laboratory. ISO, JIS, and IEC standards are not so easily accessible, as the library has not purchased access to their databases. Thus, this work has utilized ASTM standards. Two documents are particularly relevant: ASTM E927-19 provides classification guidelines for solar simulators for solar cell testing, and ASTM E491-73 provides classification of simulators for spacecraft thermal balance testing [7][6].

3.1 Solar Simulator Standard for Photovoltaic Cell Testing

ASTM E927-19 [7] sets out three parameters to be calculated in order to classify a simulator. The spectral match, R_{SM}, quantifies how closely the output power matches the solar spectral power curve over specific wavelength bands. The spatial non-uniformity of irradiance, S_{NE}, characterizes the variation in the output power over the test plane. Finally, temporal instability of irradiance, T_{IE}, quantifies the variation in the output power over time. These three parameters are nondimensionalized as percentages, relative to either the measured maximum or an accepted value, as appropriate. Guidelines have been established to label a simulator as either class A, B, C, or U (unclassified) in each category. A simulator meeting class A in each can

be called a AAA simulator. The classifications are given in Table 3.1. Notably, this standard does not require that the test plane be within a vacuum chamber. Conducting solar cell testing in ambient conditions on a tabletop or similar surface enables faster testing, since vacuum pump-down time is eliminated. However, ASTM E491-73 does require vacuum conditions for thermal testing, so the design developed herein is ideally operable in two configurations: one projecting to a tabletop and the other projecting inside a vacuum chamber. Due to the additional complexity involved in projection within a vacuum chamber, the scope of this thesis is limited to the tabletop configuration. Care has been taken to make future modifications as simple as possible.

Table 3.1: ASTM E927-19 Solar Simulator Classification [7]

Classification	**Spectral Match**	**Spatial Non-Uniformity**	**Temporal Instability**
Class A	$0.75 \leq R_{SM} \leq 1.25$	$S_{NE} \leq 2\%$	$T_{IE} \leq 2\%$
Class B	$0.60 \leq R_{SM} \leq 1.40$	$S_{NE} \leq 5\%$	$T_{IE} \leq 5\%$
Class C	$0.40 \leq R_{SM} \leq 2.00$	$S_{NE} \leq 10\%$	$T_{IE} \leq 10\%$
Class U	$R_{SM} > 2.00$	$S_{NE} > 10\%$	$T_{IE} > 10\%$

The spectral match of a solar simulator is calculated in reference to the AM0 standard given in ASTM E490-00a, which was shown previously in Figure 2.1. A spectroradiometer must be used to measure the spectral irradiance of the simulator in 10 nm increments across the normalization interval, given at the bottom of Table 3.2. This table also lists wavelength intervals over which the spectral irradiance is integrated, giving a total for each "bin" that is compared to the corresponding integral of the AM0 standard. The nature of the monochrometer and optical detector comprising the spectroradiometer is unimportant, as per guidelines in ASTM E973-16 and ASTM

Table 3.2: ASTM E927-19 Target R_{SM} (Using ASTM E490-00a) [7][5]

Wavelength Interval, nm	Ratio of Interval Irradiance to All Intervals, %
$350 \leq \lambda < 400$	4.67
$400 \leq \lambda < 500$	16.80
$500 \leq \lambda < 600$	16.68
$600 \leq \lambda < 700$	14.28
$700 \leq \lambda < 800$	11.31
$800 \leq \lambda < 900$	8.98
$900 \leq \lambda < 1100$	13.50
$1100 \leq \lambda < 1400$	12.56
Normalization Interval	$350 \leq \lambda < 1400$

G138-12 [7]. Spectral match, R_{SM}, is calculated by the following equation[7]:

$$R_{SM,\lambda 1-\lambda 2} = \frac{\frac{\int_{\lambda 1}^{\lambda 2} E_{meas,\lambda}}{\int_{350nm}^{1400nm} E_{meas,\lambda}}}{\frac{\int_{\lambda 1}^{\lambda 2} E_{ASTM,\lambda}}{\int_{350nm}^{1400nm} E_{ASTM,\lambda}}} \tag{3.1}$$

The spatial non-uniformity characteristic, S_{NE}, depends on the definition of the previously mentioned test plane. A 10 cm x 10 cm area has been chosen as a reasonable goal for this simulator, which should be sufficient for the current needs of the lab as well as future research.

To calculate spatial non-uniformity, the test plane is divided into a spatial matrix with a minimum of 64 test positions, which need not be square [7]. A square grid is straightforward to implement, however. To significantly decrease the time required to test all 64 positions, a linear array of at least 8 detector cells was chosen as a design goal. S_{NE} is calculated as the percent variation between the maximum and minimum values recorded across the spatial matrix, according to the following equation [7]:

$$S_{NE} = 100 \, \frac{max \, \mathbf{I}_S - min \, \mathbf{I}_S}{max \, \mathbf{I}_S + min \, \mathbf{I}_S} \tag{3.2}$$

For the final characteristic, temporal instability, a time period of data acquisition, t_{DAQ}, must be determined. No guidelines are given in ASTM E927-19 for the selection of this time, so it must be chosen with regard to the intended nominal operations of the simulator. For this work, it was decided that temporal instability be calculated for multiple t_{DAQ}. One long test at a high sampling frequency was subsampled to obtain temporal instability at a shorter t_{DAQ}. Similarly to spatial uniformity, T_{IE} is calculated as the percent variation between the maximum and minimum values recorded during data acquisition using the equation [7]:

$$T_{IE} = 100 \, \frac{max \, \mathbf{I}_T - min \, \mathbf{I}_T}{max \, \mathbf{I}_T + min \, \mathbf{T}_S} \tag{3.3}$$

Further details on the procedure for calculating these characteristics is provided in Appendix A.

3.2 Solar Simulator Standard for Thermal Vacuum Testing

ASTM E491-73 gives similar instructions for the characterization of solar simulators for thermal balance testing in vacuum facilities [6]. Overall, the requirements are more strict. There must be a three-dimensional test volume defined instead of a flat plane test area. Additional characteristics are used to define the accuracy of the solar simulator and vacuum chamber in simulating the space environment. Varying requirements are also given for simulator classification based on the geometry and material characteristics of the test article. One scenario detailed is that of a rotating test item. Most of these additional considerations are outside the scope of this thesis,

but will be important to future work undertaken to modify this simulator for use with the lab's vacuum chambers.

Class A, B, and C requirements are based on seven characteristics, as shown in Table 3.3, except for the spectrum, which is specified in Table 3.4.

Table 3.3: ASTM E941-73 Solar Simulator Classification [6]

Test Volume Characteristics	**Class A**	**Class B**	**Class C**
Uniformity of Irradiance, E_u	3%	5%	$> 5\%$
Stability of Irradiance, E_t	1%	3%	$> 3\%$
Solar beam divergence angle	$< 2^\circ$	$< 4^\circ$	$> 4^\circ$
Reflected irradiance	$< 2\%$ of incident	$< 5\%$ of incident	$> 5\%$ of incident
Radiation-environment temperature	<80K	≤100K	>100K
Chamber pressure	10^{-6} torr	10^{-5} torr	$< 10^{-4}$ torr

Irradiance measurements do not have to be made in vacuum to characterize the solar beam. This allows calculations to be made in this work to classify the simulator under both ASTM E927 and ASTM E491. Detectors can be thermal or photoelectric; thermal types are recommended [6]. Photoelectric detectors must have their variance with wavelength characterized (i.e. SR or EQE), and the spectrum of the simulator must be measured first so that irradiance can be properly calculated. Thermal type detectors, in contrast, must be spectrally flat over the 250-2500 nm range, and do not require extra calibration steps. To simplify the testing process for this thesis, however, the decision was made to use a photoelectric detector that complies with ASTM E927-19 as well as E491-73.

The spatial non-uniformity S_{NE} discussed in [7] is referred to as the uniformity of irradiance in [6], and represented by E_u. Multiple planar scans can be used to obtain these measurements over the volume. Multiple detectors in a line or array may be used to shorten the total testing time. E_u is calculated by the equation:

$$E_u = \pm 100(\Delta \frac{E_{min} + \Delta E_{max}}{2\bar{E}}) \tag{3.4}$$

where ΔE_{min} and ΔE_{max} are the differences between the mean irradiance and the smallest and largest measured values for irradiance, respectively (Note the factor of two compared to Eq. 3.2). The mean total irradiance, $\bar{E}$, is defined by

$$\bar{E} = \frac{\int_v E(r, \theta, z) dV}{\int_v dV} \tag{3.5}$$

where $E(r, \theta, z)$ is the irradiance at a position in the test volume and $\int_v dV$ is the volume integral of the test volume. $E(r, \theta, z)$ would be calculated by a form of Eq. 4.2, which is discussed in Chapter 4.

The temporal instability T_{IE} discussed in [7] is referred to as the stability of irradiance in [6], and represented by E_t:

$$E_t = \pm 100(\frac{\Delta E_{t,min} + \Delta E_{t,max}}{2\bar{E}}) \tag{3.6}$$

(Again, note the factor of two compared to Eq. 3.3).

The spectral match R_{SM} discussed in [7] is referred to simply as the spectrum in [6]. It must be determined using spectral irradiance measurements with a spectrometer or similar device. Measurements must be taken over all relevant wavelengths, depending on the absorption characteristics of the test article. 250-2500 nm is given as a standard range that is generally applicable, which overlaps the 350-1400nm range given in [7].

The ratio of the solar simulator irradiance to reference irradiance must be used to classify the simulator spectrum according to Table 3.4 over the general 250-2500 nm range using the equation:

$$Ratio = \frac{E_{\lambda,SSI}}{E_{\lambda,AM0SI}} \tag{3.7}$$

where $E_{\lambda,SSI}$ is the measured irradiance per wavelength interval of the solar simulator, and $E_{\lambda,AM0SI}$ is the irradiance over the same wavelength interval of standard AM0 solar irradiance given in ASTM E490-00a [6].

Table 3.4: ASTM E491-73 Class A and B R_{SM} Tolerances [6]

Wavelength Interval	**Measuring Bandwidth**	**Number of Bands**	**AM0SI per Interval**	**Tolerable Ratio**
Class A				
250-400 nm	10 nm	15	115 $\frac{W}{m^2}$	0.60-1.40
400-700 nm	10 nm	30	516 $\frac{W}{m^2}$	0.80-1.20
700-1000 nm	50 nm	6	306 $\frac{W}{m^2}$	0.60-1.40
1000-2500 nm	100 nm	15	363 $\frac{W}{m^2}$	0.60-1.40
Total		66	1300 $\frac{W}{m^2}$	$\frac{2}{3}$ of bandwidths per interval must meet tolerance.
Class B				
250-400 nm	50 nm	3	115 $\frac{W}{m^2}$	0.35-1.65
400-700 nm	100 nm	3	516 $\frac{W}{m^2}$	0.50-1.50
700-1000 nm	150 nm	2	306 $\frac{W}{m^2}$	0.35-1.65
1000-2500 nm	500 nm	3	363 $\frac{W}{m^2}$	0.20-1.80
Total		11	1300 $\frac{W}{m^2}$	Eight bandwidths must meet tolerance.

A general method of measuring the simulator's spectrum with a typical spectroradiometer is outlined in the standard; unfortunately, such equipment is prohibitively expensive and currently not available on campus. The basic process, however, is applicable to any type of spectrum evaluation.

The solar beam divergence angle, shown in Figure 3.1 is defined as the maximum angle between the center of the apparent solar source as viewed from the test plane and the solar beam principal axis, measured in degrees [6]. Related is the subtense angle, also shown in Figure 3.1, which is defined as the angle between two edges of the apparent solar source, as viewed from a point on the test plane. The maximum solar beam divergence angle is found at the edges of the test plane. The divergence angle determines the decrease in irradiance due to the beam spreading out as it propagates from the top of the test volume to the bottom. Large divergence angles lead to increased innacuracy of shadow geometry.

The standard recommends using a theodolite to measure these various angles, though any accurate angular measurement system would suffice [6]. Measurements must be

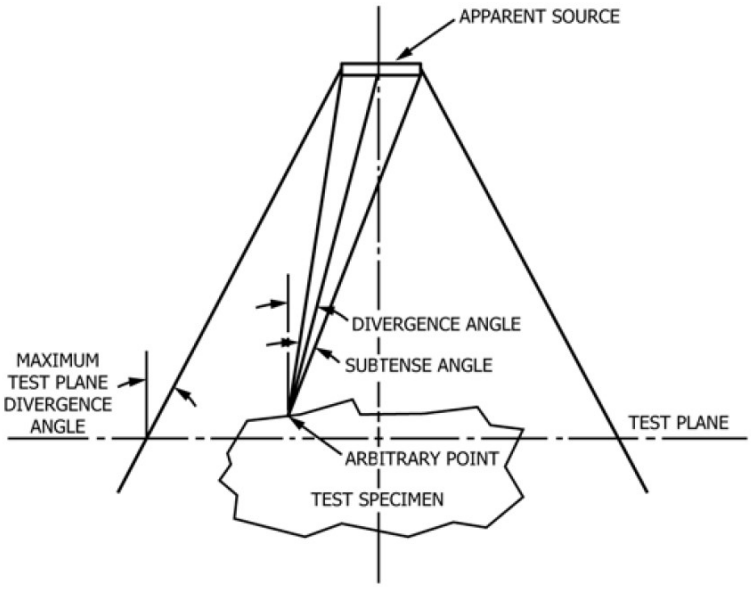

Figure 3.1: Solar Subtense and Divergence Angles [6]

taken in this fashion or similar at least at the top and bottom of the test volume, with intermediate measurements as necessary. The reported values for divergence and subtense angle are the worst cases measured.

Reflected irradiance is defined as the sum total of radiant energy entering the test volume from all sources besides the first pass of the solar beam, and includes both specular and diffuse reflections. This irradiance could, for example, be reflected onto the chamber walls and then back to the test article. The geometry and surface materials of the test article significantly impact the reflected irradiance, so this characteristic varies from test to test [6].

Another measure of erroneous radiant energy is the radiation-environment temperature, defined as the equivalent temperature in Kelvin of a blackbody surface surrounding the test volume that would provide the same radiant energy exchange as the actual test volume has with the chamber walls (or cooling shroud, if present).

The chamber pressure, measured in torr, is that nominally attainable within the test volume by the vacuum pumping system. A secondary concern of vacuum conditions is the deterioration of optical elements, especially mirrors, due to outgassed contaminants. It is suggested for future modifications that the chamber and any test articles undergo a bakeout with any optical elements covered/removed, before uncovering/replacing them to conduct the desired test. A simpler solution is to locate any optical elements outside the vacuum chamber. ASTM E491 suggests several methods of monitoring outgassed contaminant during testing - mass spectrometers, witness plates, quartz crystal microbalances, or similar [6]. Of these, witness plates are by far the simplest and most budget-friendly.

Additional details on the measurement of these characteristics is provided in Appendix B. ASTM E491-73 also provides guidance for writing operating procedures for solar simulator facilities, which has been valuable while documenting this work.

3.3 Traditional Light Sources

Carbon arc lamps were one of the first types to be used in solar simulators [57]. They use two carbon rods as electrodes in free air. These lamps have a close spectral match to the sun's spectrum, but multiple drawbacks. Carbon arc lamps have a very short operational time before the rods must be replaced, have low temporal stability, and overproduce blue light. The arc also exhibits high instability during startup.

Quartz tungsten halogen lamps are inexpensive and have high radiant power output. They are a form of incandescent lamp where a tungsten filament is surrounded by high-pressure halogen gas, such as bromine. This gas causes a halogen cycle whereby any evaporated tungsten is chemically redeposited onto the filament, extending the lamp's lifetime over a traditional incandescent bulb. However, these lamps have a spectrum that is too weak in the UV and blue regions, and too strong in the infrared [57]. Their other advantages have led to the use of quartz tungsten halogen in multi-source simulators to provide the infrared portion of the spectrum.

Mercury xenon lamps were widely used in early solar simulators. These lamps consist of two electrodes in a high-pressure bulb containing a mix of xenon gas and mercury. Documentation of the JPL 25-ft space simulator reveals some of the drawbacks of these lamps: they tend to create ozone, are prone to explosion, and release mercury vapors [18][22]. They were replaced in that facility by xenon arc lamps. Other problems with mercury xenon lamps are the presence of narrow bands of high spectral energy emission and very high ideal operating pressures.

Xenon arc lamps are commonly used in modern solar simulators [57][31]. They consist of two electrodes in a high-pressure xenon gas bulb, and the light is generated by a plasma cloud at the cathode. In the UV and visible ranges, xenon arc lamps have an excellent spectral match with the sun, with an equivalent blackbody temperature of around 5400 K, and have a very small arc area, which makes them easy to collimate [31]. These lamps do have strong spectral peaks in the near infrared region, however, and are very expensive compared to most other options. Additionally, like mercury xenon lamps, xenon arc lamps operate under very high pressure and pose a corresponding explosion hazard.

Metal halide arc lamps take advantage of compact source iodide (CSI) to produce highly directional intensity distributions, reducing the need for secondary optics [57]. The bulb is filled with argon or xenon as well as mercury and some type of halide - the most common is sodium iodide. These lamps offer good luminous efficacy, decent spectrum match, long operational lifetimes. The cost is lower than for xenon arc lamps, but higher than quartz tungsten halogen. Metal halide lamps do overproduce IR and underproduce UV, much like quartz tungsten halogen lamps. Along with quartz tungsten halogen lamps, metal halide arc lamps are a common alternative to xenon arc lamps.

3.4 Comparison of LEDs to Traditional Light Sources

Compared to the traditional types of arc lamp used in solar simulation, many LEDs have a significantly higher radiant efficiency [10][31]. The most efficient arc lamps fall in the 10-20% range, while LEDs range from 30-50%. The spectral power distribution of arc lamps ranges from the UV to the IR range, usually approximating a blackbody curve, but punctuated with strong emission peaks and valleys determined by the

chemical composition of the arc plasma [31]. LEDs have a much narrower spectral distribution. Multiple wavelengths of LED are necessary to approximate a blackbody curve; the exact number depends on the closeness of the desired match and the width of the wavelength bins. The total emitted power of LEDs is much lower than arc lamps, which often emit in the kW range. LEDs, however, are much smaller, especially considering the large parabolic or elliptic reflectors that usually accompany arc lamps.

LED thermal management is simpler; arc lamps are often water cooled, while LEDs can be sufficiently cooled with passive or active convection via a finned heat sink [10][26][9]. Both light sources require specialized power supply regulators, though those of LEDs tend to be somewhat simpler. Arc lamps are significantly more expensive per unit, ranging from hundreds to thousands of dollars, compared to LEDs at a few dollars or even cents per unit. It must be kept in mind, though, that large numbers of LEDs ($50-100) are needed to equal the output of one arc lamp. Lastly, arc lamps have much shorter lifetimes, typically requiring replacement after a few thousand hours of use, while LEDs can be operated for tens of thousands to hundreds of thousands of hours before deteriorating, depending on their operating temperature [57]. This increased lifetime more than makes up for the large number of LEDs needed in terms of cost, offering an enormous lifetime cost benefit. A summary of the comparison between LEDs and traditional light sources is presented in Table 3.5.

Overall, LEDs offer compelling advantages, primarily in long-term cost and compactness. Neither option is without its complications, but the decision was made to use LEDs as the primary light source in this work, supplemented by an incandescent IR lamp.

Table 3.5: Comparison of LEDs to Traditional Light Sources

Light Source	Spectrum	Stability	Lifetime	Cost	Safety Risk
Halogen, Incandescent	UV - Weak, IR - Heavy	High	Moderate	Low	High
Arc	Very Good	Moderate	Moderate	High	Very High
LED	One - Poor, Many - Good	High	Very Long	Very Low	Low

3.5 Expected Hazards and Mitigation

The addition of a solar simulator to the space environments lab could introduce a few hazards not already present due to the vacuum and UV equipment currently in use. An excellent overview of hazards attendant to space environment solar simulation is given in ASTM E491-73 [6]; the sources and mitigations of hazards accompanying this work's solar simulator are outlined in Table 3.6.

Table 3.6: Solar Simulation Hazard Overview [6]

Potential Hazard	Mitigation
Implosion of Vacuum Windows	Wear safety glasses, set screens or shields around ports
Excessive Heating of Vacuum Windows	Monitor window temperature while irradiated, keep windows free of contaminants, set screens or shields around ports
Ozone	Avoid UV radiation of $100< \lambda <240$ nm, generate UV radiation of $240< \lambda <315$ nm, monitor ozone concentration
High Voltage	Insulated wiring, discharge capacitors
High Current	Adequate cable size, good ventilation
Erythema	Avoid UV of 240-270 nm and 290-320 nm, cover exposed skin, apply sunscreen
Conjunctivitis	Avoid UV below 320 nm (similar to erythema), wear dark glasses or goggles with side shields
Retinal Burns	Avoid arc lamps, wear dark glasses or goggles

3.6 Supporting Equipment

Besides the light source and possible vacuum chamber, solar simulators also consist of equipment to supply power, manage thermal loads, and control light output. Arc lamps require specialized power supplies to prevent unstable plasma behavior [57]. Typical electrical to radiant power conversion efficiencies are 10-20% [31][10], so for large simulators it is immediately obvious that matching the 1360 $\frac{W}{m^2}$ solar constant requires many kilowatts of electrical power. Coupled to this high power requirement is the waste heat produced. Large solar simulators require thermal control systems with many kilowatts of capacity.

The 10cm x 10cm system proposed here covers 0.01 m^2 of area, necessitating 13.6 W of optical power. Assuming an electrical efficiency of 30-50%, as is typical for LEDs [27][10][31], an estimate for minimum required power is 50 W, with a 35 W thermal load. However, this assumes that all of the emitted power will make it to the test pane, which is not realistic. A transfer efficiency of 50% is optimistic; it is not unreasonable to expect a lower transfer efficiency of 10-20% in the worst case [29]. Thus, the simulator should be designed with the expectation that it may consume 500 W of electrical power, and may have to manage a heat load of about the same. The design work herein attempts to minimize total power input.

3.7 Examples of Large Solar Simulator Facilities

Many large-scale solar simulators in various configurations have been included in vacuum chamber systems for spacecraft thermal testing. The JPL 25-ft Space Simulator mentioned earlier includes a 20-ft wide solar beam, as illustrated in Figure 3.2. The light source was origninally mercury-xenon arc lamps, but was refitted with higher-

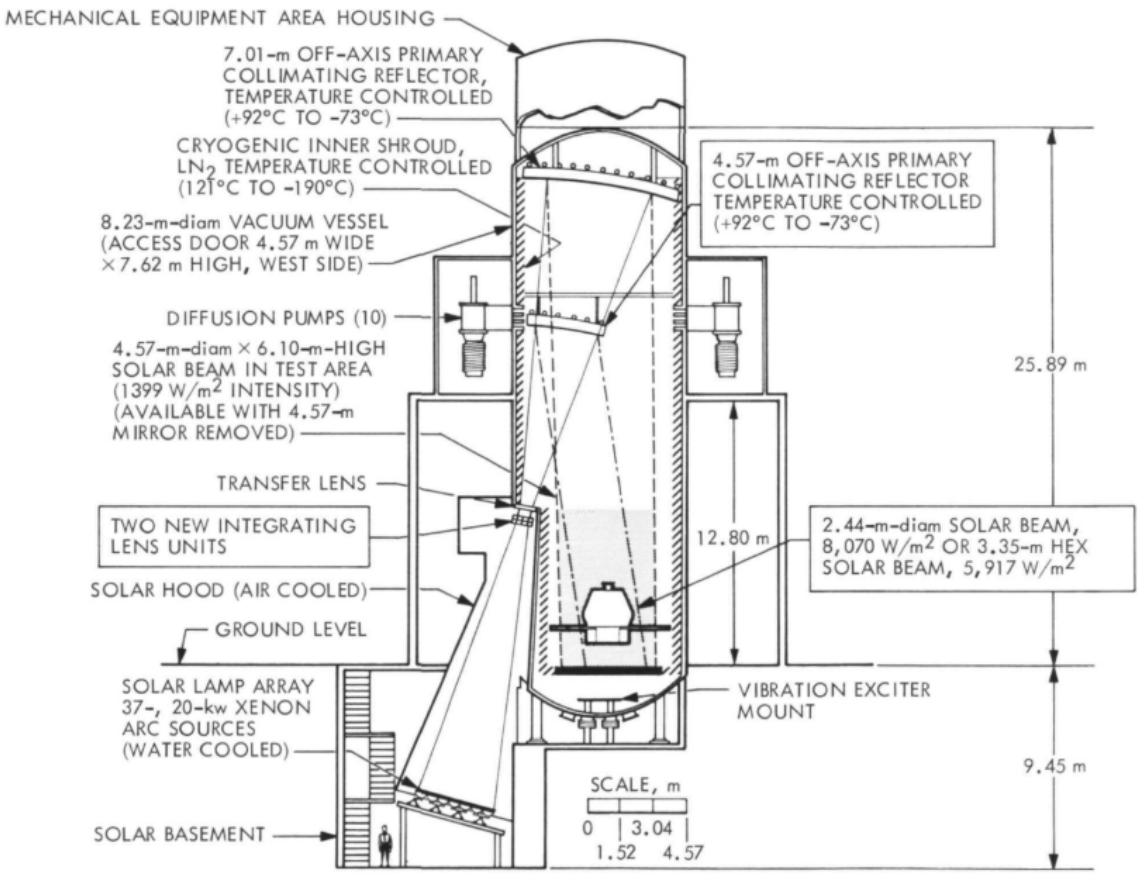

Figure 3.2: JPL 25-ft Solar Simulator Facility [22]

powered water cooled xenon arc lamps in the early 1960s [18][22]. The attendant vacuum chamber is a 27 x 85 ft cylinder with a liquid nitrogen cooling shroud. The solar beam provides up to 314 $\frac{W}{ft^2}$ with a spatial uniformity of +/- 5% and a maximum divergence angle of 1° through a cylindrical test volume of 20 ft diameter and 25 ft height. Similar large Class A solar simulators are present in multiple other NASA facilities, such as Goddard Space Flight Center and Lewis Research Center, as well as in facilities around the world such as those operated by IBAG in Germany, NIICHIMMASH in Russia, and the University of Bern in Switzerland [57].

Besides spacecraft thermal testing, solar simulators have also been increasingly used to test solar electricity generation devices for use on Earth's surface. These fall into two broad categories - concentrating and non-concentrating. Concentrating solar

simulators share the large, power-hungry light sources of the above simulator designs, but concentrate this radiant power into a very small surface area, achieving irradiances of dozens to hundreds of times the solar constant. Concentrating simulators of a wide variety of designs for these purposes have been constructed by Lewis Research Center, Marshall Space Flight Center, MIT, Spectrolab, and Solarec the US; JMI Institute in Japan; DFVLR in Germany; the Indian Institute of Technology in India; and ETH-Zurich in Switzerland, from 1960 to the present [57].

Chapter 4

LED OPERATION AND USE IN SOLAR SIMULATION

4.1 History of LED Development and Adoption

LEDs were developed in the 1950s and began selling commercially in the 1960s as semiconductors were extensively studied and tested [27]. The first LEDs emitted light in the near-infrared region.Further development produced the first LEDs to emit visible red light.Advances in semiconductor technology then produced yellow LEDs, and, in the 1990s, intensely bright blue LEDs. These trends can be seen in Figure 4.1. A major innovation at this time that resulted in the modern lighting industry was the application of phosphorus powder to a blue LED die [27]. Excited by the intense blue radiation, it phosphoresces strongly in the yellow region of visible light. The combination of blue and yellow is perceived as white to the human eye, and with careful adjustment has resulted in LEDs that sufficiently mimic daylight. Household lighting fixtures utilizing these LEDs have made incandescent and compact fluorescent bulbs nearly obsolete.

The range of LEDs operating at high quantum efficiency has expanded to include nearly all of the visual spectrum, excluding the region corresponding to intense green, known as the "green gap", which can be visualized in Figure 4.2 [27].

Today, UV LEDs have become economical enough to enjoy widespread usage in ozone production, germicidal treatments, and curing epoxies [27]. LEDs have found use in grow lights tuned to produce the wavelengths of light that are most readily absorbed by chlorophyll. Fiber optical communication has seen widespread adoption of LEDs as an optical source, since the semiconductor junctions respond to electrical inputs

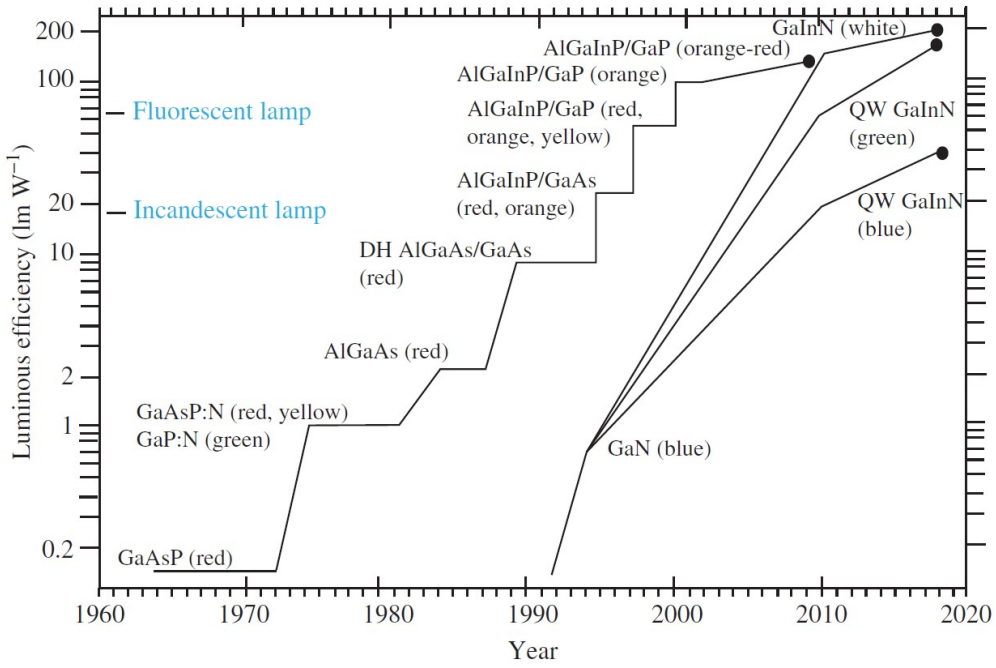

Figure 4.1: History of Luminous Efficacy in LED Development [27]

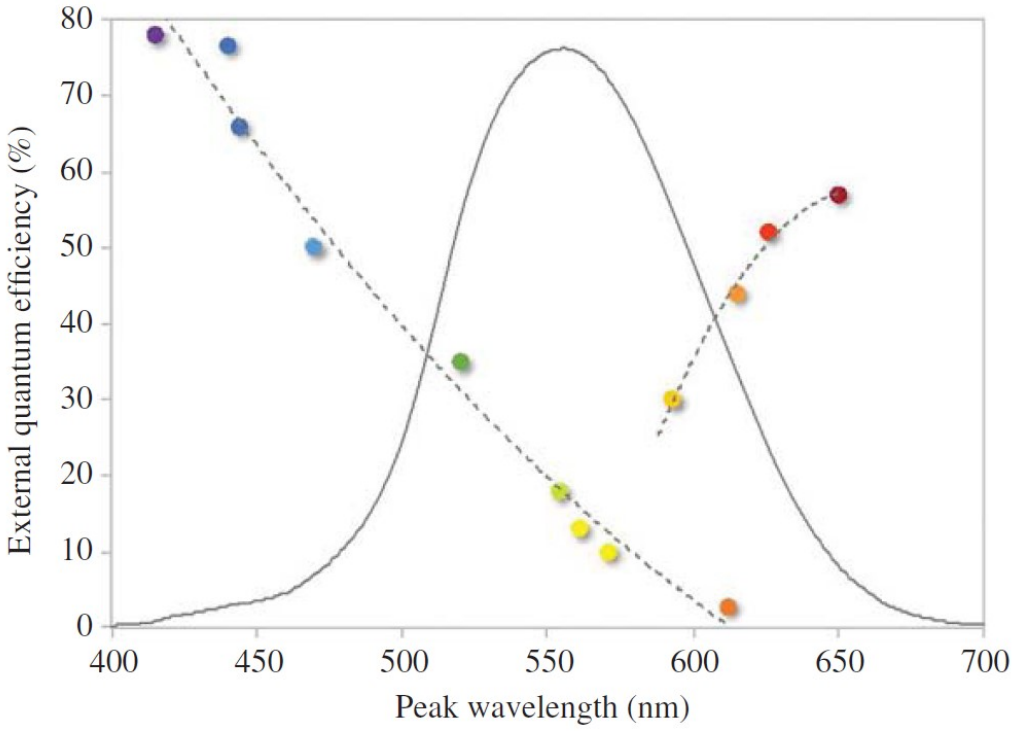

Figure 4.2: The "Green Gap," Shown With the V_λ Curve [27]

in nanoseconds, allowing for extremely fast pulses [10]. LEDs can be tuned to emit coherent waves, and are commonly used as laser sources.

Some recent research in LED technology has focused on improving manufacturing methods. The size of LED packages has continually decreased. Chip-on-board (COB) manufacturing allows dozens of individual LED dies to be placed next to each other, effectively concentrating them into a much smaller package. Another recent trend in research is the pursuance of shorter and shorter UV wavelengths. Currently, the shortest wavelengths are just above 200 nm [27]. Research is also being conducted into the development of broadband LEDs. One of the first commercially-available LEDs of this type is Ushio Opto-Semiconductor's Spectro Series, which uses a combination of multiple types of phosphorus to emit over the whole visible and some of the NIR spectrum [56]. The indoor lighting industry has been continually working to pack more apparent brightness into smaller packages with as high of an electrical efficiency as possible. High-power white LEDs operating in the 1-3 A range have become common [27].

4.2 Light Generation Across Semiconductor Junctions

LEDs are in many ways the reverse of a solar cell. They are composed of a p-n semiconductor junction, which is bonded together and forms a charge-depletion region at the junction, establishing an electrical field across it just as solar cells do. Unlike photovoltaic cells, however, LEDs are biased in the forward direction. Electrons flowing through the LED, if they have sufficient potential energy in the form of voltage greater than the band gap, must "fall" down the band gap to recombine in the depletion region [27]. This excess energy is released as photons. In fact, sufficiently forward biasing solar cells causes them to emit light, acting as large-area LEDs (typical silicon

solar cells emit IR light when operated in this fashion). Similarly, LEDs respond to incident light in the same way that photodiodes do, generating a small amount of reverse-biased current. This duality can be exploited in optical communications to send and receive signals simultaneously with one semiconductor device.

The wavelength of a released photon is determined by the LED's band gap energy, which is the difference in quasi Fermi levels of the p and n region [27]. Slight variations in excess electron energy cause the wavelengths to form a roughly Gaussian distribution about the mean, or peak, wavelength. LEDs are thus mainly specified by their peak wavelength, and further categorized by the full width at half maximum, $FWHM$, which is the distance between wavelengths on each side of the peak where the emitted power falls to half that emitted at the peak. LEDs, as diodes, conform to the Shockley diode equation in the ideal case:

$$I = I_0(e^{(\frac{qV}{k_B T})} - 1) \tag{4.1}$$

where q is the elementary charge of an electron, k_B is Boltzmann's constant, T is the junction temperature, V is voltage, and I_0 is the reverse saturation current, which is the only current present under large negative values of V [27]. A simple way to model LEDs electrically is as a constant voltage drop. Above the required threshold voltage determined by the band gap, LEDs have effectively zero equivalent resistance, and must be operated via current-control. The dependence of emitted radiant power on voltage, current, and temperature of the LED is highly nonlinear, and it is typical for manufacturers to include graphs of these relationships in their datasheets. An example is shown in Figure 4.3.

Light is not emitted isotropically from an LED surface. An ideal LED is a perfect Lambertian emitter, meaning that the irradiance decreases according to the cosine

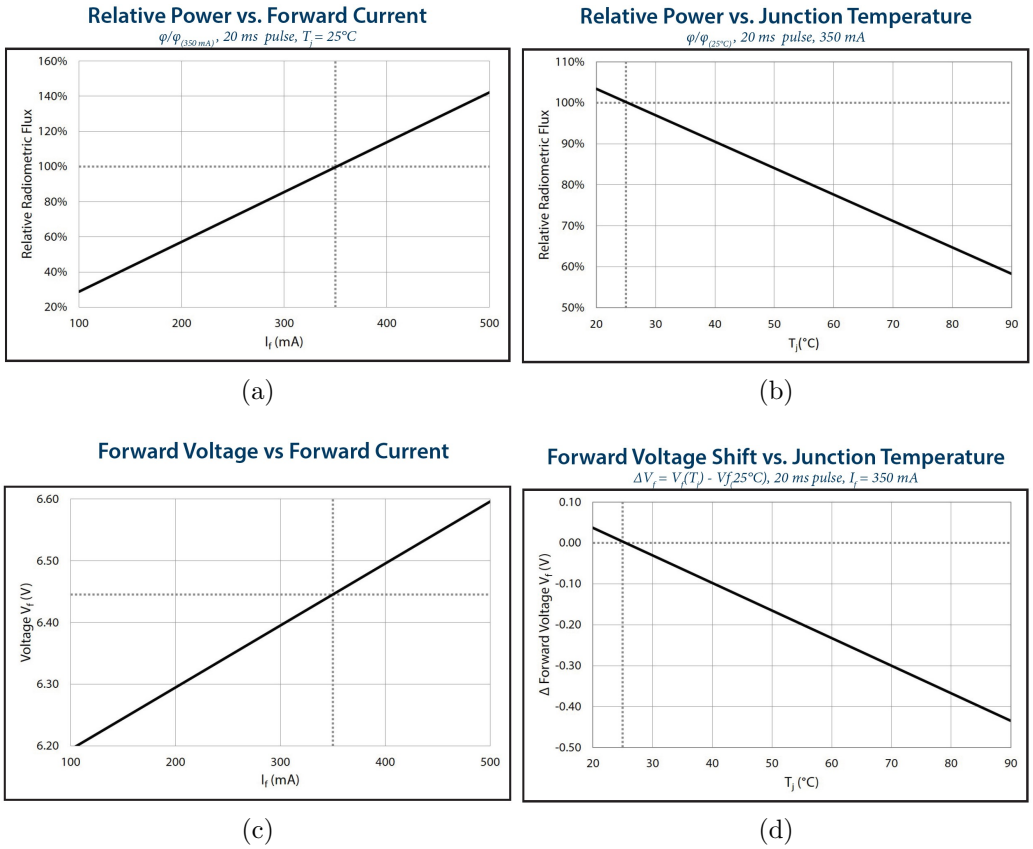

Figure 4.3: Luminus XST-3535-UV LED Performance Curves [39]

of the angle from the surface normal. Non-ideal LED irradiance distributions can be roughly modeled [43] with the equation:

$$E = E_0 \cos^m(\theta) \tag{4.2}$$

where θ is the angle from the centerline of irradiance, the peak value of irradiance E_0 occurs at the centerline ($\theta = 0°$), and m is a parameter determined by the viewing half-angle, $\theta_{\frac{1}{2}}$ (not to be confused with θ), which is the angle between $\theta = 0°$ and the angle at which the intensity decreases to half its maximum value. For an ideal Lambertian emitter, $m = 1$, corresponding to $\theta_{\frac{1}{2}} = 60°$, but for many common LEDs, $m > 30$ [43]. $\theta_{\frac{1}{2}}$ is usually reported in datasheets by LED manufacturers. The

parameter m in Eq. 4.2 is calculated as [43]

$$m = -\frac{ln(2)}{ln(\cos(\theta_{\frac{1}{2}}))} \tag{4.3}$$

An example angular irradiance distribution is shown in Figure 4.4, in both polar and rectangular coordinates.

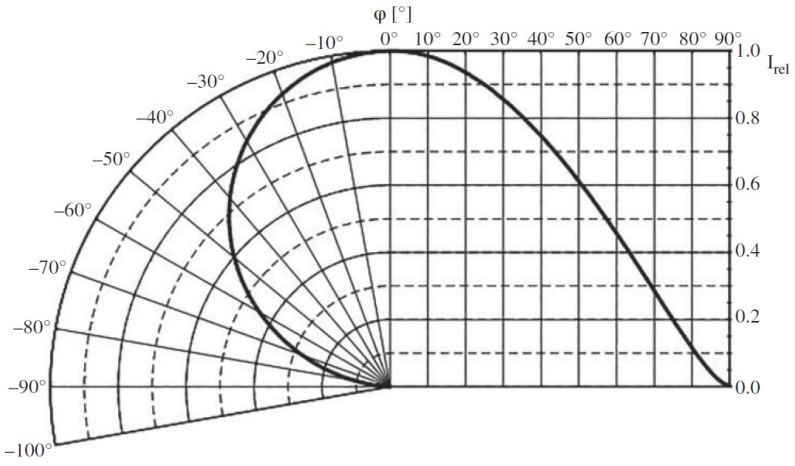

Figure 4.4: Angular Irradiance Distribution for LED With $\theta_{\frac{1}{2}} = 115°$ [27]

Not all LEDs can be modeled by Eq. 4.2. Some LEDs emit primarily in a hollow cone shape, and are called batwing LEDs because their intensity distributions show two strong peaks [44]. Side-emitting LEDs are similar, but, as the name suggests, emit the vast majority of their radiation out of the sides of the die, at right angles to the surface normal [44]. Additionally, the method of construction and case materials distort the angular distribution away from a perfect sinusoid. Datasheets typically include a graph of the measured angular distribution, as well as a graph of spectral power and values for electrical power consumed, nominal current and voltage, total radiated power, $FWHM$, and $\theta_{\frac{1}{2}}$.

4.3 Typical Parameters of Modern LEDs

By comparing datasheets from online retailers [32][40][33] and the websites of large-volume manufacturers such as Osram, Cree, and Lumileds [50][15][34], an idea of current trends in commercially available LEDs has been obtained. These LEDs mostly fall into two categories: high- and low-power. Low-power LEDs usually are designed to operate on less than 10 V with a few hundred mA. High-power LEDs are usually designed to run at 30-60 V with 2-3 A of current. Correspondingly, low-power LEDs consume from less than a hundred to a few hundred mW, while high-power LEDs can consume 10-100 W.

Evaluating the efficiency of the LEDs in converting electrical power to radiant power is complicated by the fact that only LEDs that emit primarily in the UV or IR regions report their radiant power in Watts; all visible color and white LEDs report the luminous power output instead, using lumens. Thus, the commonly reported efficiency in LED datasheets is lumens per watt, called luminous efficacy, which is a measure that varies inherently with wavelength. To compare the luminous efficacies of LEDs of different colors or apparent equivalent blackbody temperatures is impossible without use of the spectral luminous efficiency function, $V(\lambda)$, which means that an integration step is required.

The radiant efficiencies of color LEDs in the visible spectrum are roughly comparable, and tend to be on par with the radiant efficiency of white LEDs. UV and IR LEDs tend to be less efficient. Overall, efficiencies range between roughly 10-50%. Most high-efficiency white LEDs have luminous efficacies of 100-200 $\frac{lm}{W}$, while efficient violet and deep red LEDs typically have luminous efficacies closer to 1-10 $\frac{lm}{W}$ due to the decreased sensitivity of the human eye to these wavelengths. Generally, the more electrically efficient an LED is, the more expensive it is. This sometimes, but not

always, correlates with high luminous efficiencies - the ambiguity arises from the V_λ curve. For a low-cost simulator for university use, the cutting edge of efficiency is unlikely to be worth the higher price tag. The space environments lab is well equipped with power supplies, making electrical power draw less of a limiting factor than cost.

UV and IR LEDs typically emit only tens of mW of total radiant power, though a few high-power versions are available that emit in the 100-1000 mW range. Color LEDs range widely over the hundreds of mW range in total power output. Color LEDs at either edge of the visual spectrum usually emit 10-100 lm. Color LEDs in the middle of the visual spectrum are usually rated around 100 lm, with some high-powered ones emitting around 1000 lm. White LEDs range widely in total luminous power output, from the low tens of lm to over 30,000 lm. Again, extremely high power outputs are extremely expensive, and unlikely to be worth their cost. For the purposes of this thesis, LEDs were judged favorable the higher their ratio of watts (or lumens) to dollars.

The cheapest LEDs tend to be low-powered with low luminous efficacies, and are sold for a few cents per unit. The vast majority of color and white LEDs are sold for between $\$1 - 10$ per unit, while extremely high-power, UV, and NIR LEDs can be found from $\$20 - 50$ per unit. A few extremely specialized types of LEDs, such as those in the deep UV and far IR ranges, as well as the highest-power LEDs of any wavelength range, are sometimes over \$100 per unit. Searching has shown that at least one option exists for an LED of nearly any peak wavelength in the 275-1600 nm range for under \$20 per unit. IR LEDs of wavelength 1600-2500 nm proved difficult to find for under \$100.

Many different form factors of LED are available. Surface-mounted is one of the smallest packages offered, usually measuring a few mm on each side. A slightly larger common package is a simple integrated metal-core printed circuit board (MCPCB).

While surface-mount LEDs have their electrical connections on the bottom surface, and are intended to be assembled with reflow soldering, LEDs on MCPCB typically have electrical connections on the top surface, and are more easily soldered by hand [40]. The increase in top surface area means these LED packages measure about a centimeter on a side if square, and up to 2 or 3 cm across if in a round configuration. A round MCPCB is common for COB LEDs. Another popular configuration is a "star," a slightly larger MCPCB with three or six tabs in a star-like shape. This configuration would be the most difficult to integrate into a tightly-packed array if some star packages were not offered with three identical LEDs on the same MCPCB, called a "3-up."

Surface mount and MCPCB are intended to be mounted on flat surfaces with a low-resistance thermal path to a heat sink. There are also through-hole LEDs, which are vastly more common in craft, DIY, and microcontroller-centered applications. This form is also very small, typically 5 mm in diameter, and is usually a clear or colored acrylic cylinder with electrical wires extending out of the bottom, making it easy to mount on a breadboard or connect to a simple circuit. The durability of the acrylic casing and the ease of electrical connection are the primary factors contributing to the popularity of this packaging. Unfortunately, these through-hole LEDs are universally low-powered, and have poor angular distributions. Some higher-end through-hole LEDs are manufactured with metal casings, and have excellent angular distributions.

Angular irradiance distributions vary widely, as they are primarily determined by whether or not the LED is packaged with a small lens or not. Through-hole LEDs include a lens by default, but these tend to be cheaply made and rarely have narrow viewing angles. These angles can vary from 30-100°, though some expensive through-hole LEDs have glass ball lenses and viewing angles $< 10°$ [55]. Surface-mount LEDs are sometimes manufactured with a small included lens, and sometimes not. Without

a lens, these LEDs have wide viewing angles of 60-120°, but with lenses can be found with viewing angles between 5-30°. Surface-mount LEDs with included lenses are more expensive, but only tend to exceed $20 per unit at the lowest viewing angles. LEDs mounted on MCPCB are sometimes included with lenses, and have similar viewing angles as surface-mount LEDs. However, lenses for standard forms of MCPCB are sold for $\$1 - 10$ apiece separately, and can be easily mounted to the MCPCB with adhesive tape. Lenses compatible with the star form factors are particularly common.

The overwhelmingly vast majority of commercially available color LEDs have an $FWHM$ of 10-20 nm. White LEDs are available in color temperatures (equivalent blackbody temperatures) of 1500-8000 K [32]. These white LEDs have a peak at 450 nm with an $FWHM$ typical of color LEDs, and then have a second peak of varying shape and power based on the color temperature, usually centered around 650 nm with an $FWHM$ of 50 nm. NIR LEDs of wavelengths longer than 900 nm tend to have higher $FWHM$s, usually of 50 nm. Far into the NIR range, around 2000 nm, an $FWHM$ of 100 nm is typical [55]. UV LEDs usually have a narrow $FWHM$, similar to color LEDs. A small number of expensive broadband LEDs in the visible and NIR range exist. These broadband LEDs have spectral power distributions analogous to white LEDs, with a strong peak at 450 nm. Broadband visible LEDs, however, have a second peak with an $FWHM$ of 100-200 nm centered somewhere between 600-700 nm. Broadband NIR LEDs have a second peak with an $FWHM$ of 250 or more nm, centered between 800 and 1000 nm.

4.4 Existing LED-Based Simulator Designs

Designing a solar simulator using LEDs as the sole light source has been possible for over a decade. A handful of papers detail different designs, and some commercially available models exist, such as Oriel's VeraSol Class AAA simulator [31]. Most commercial models such as this are designed to match the AM1.5 spectrum. Information on LED arrays for photovoltaic device testing and indoor lighting is plentiful, but LED-based solar simulators for thermal and vacuum chamber use seem to be a comparative rarity.

Bliss et. al. in [10] describe a solar simulator for photovoltaic testing providing irradiation of one solar constant over a 20 x 20 cm area. The UV and visible spectrum light was supplied by several hundred LEDs of 8 different colors, with NIR radiation supplied by halogen lamps. [10] also discussed a revised design using additional LED colors for the NIR region as well. The prototyped simulator was experimentally verified using an IEC standard analogous to ASTM E927-19. This design achieved class A temporal stability with 15 min warm up period, class B spectral match to the AM1.5G spectrum, class C non-uniformity over the full 20 x 20 cm test plane, and class B non-uniformity over the center 10 x 10 cm area of the test plane. LabVIEW was used with a personal computer to controleach LED string. An diagram of the simulator is shown in Figure 4.5

Another LED-based simulator for photovoltaic testing is outlined in Kolberg et. al. [28]. A test prototype with 6 different LED colors was used to experimentally verify the principles behind a large array designed to match the AM1.5G spectrum using much more color variety. The theoretical spectrum comparison is shown in Figure 4.6. The temporal stability of this prototype was shown to be 0.3% after a warm-up

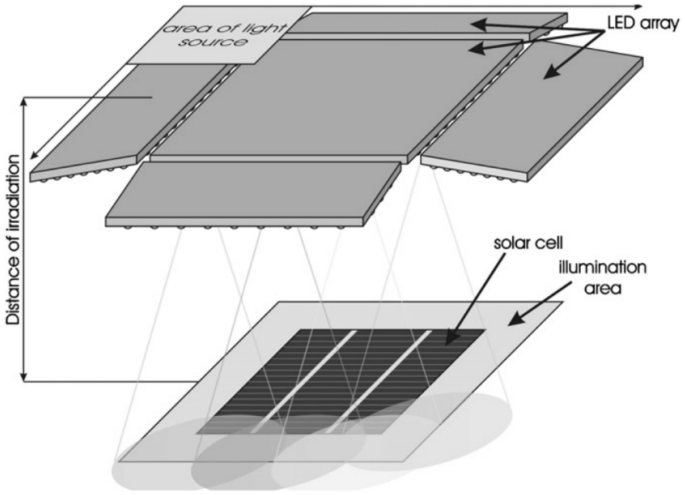

Figure 4.5: Bliss et. al. Solar Simulator Array Design [10]

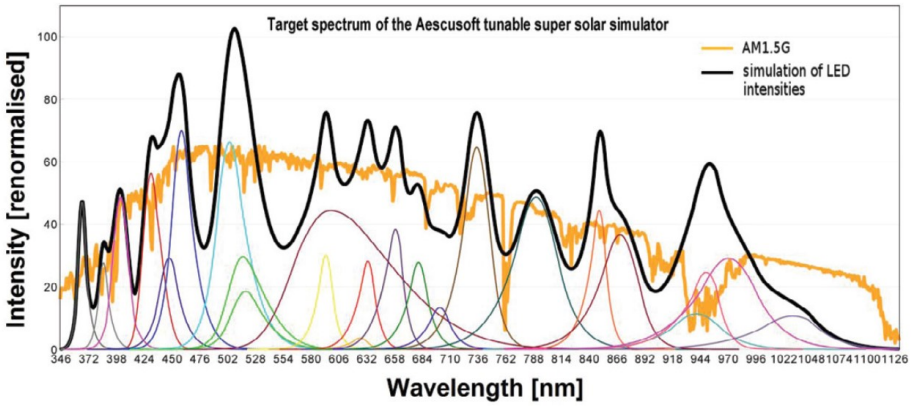

Figure 4.6: Kolberg et. al. Spectrum Comparison [28]

time of 5 min. Each LED was controlled by a separate custom-built current regulator circuit, with software-controlled voltages.

Similar simulators have been constructed for photovoltaic testing at Tokyo University of Agriculture and Technology in Japan and Myong Ji University in Korea, with test areas of 20.5 x 20.5 and 22 x 55 cm respectively [57]. The Myong Ji University simulator is listed as having a total power output of 144 W.

A detailed account of the design process for an LED-based solar simulator specialized for testing of space-rated triple-junction solar cells was given in Kim et. al. [26]. This

design is of particular interest because it was the only one found that used AM0 as the reference spectrum. This simulator provided illumination of one solar constant over a 10 x 30 cm test plane, so chosen to be representative of one side of a 3U CubeSat [26]. The desired classification was class C under ASTM E927-10. The use of this previous revision of the standard is significant because it required only 36 test positions for evaluation of spatial non-uniformity, whereas the current revision, E927-19, requires a minimum of 64 [7].

Four colors of LED were used for the UV and visible spectrum: UV, blue, cyan, and neutral-white. Halogen lamps were used for the NIR portion, similar to [10] above. The LEDs were set in a hexagonal distribution with a center point, equivalent to a tesselated triangular distribution. This arrangement has been shown by multiple analyses of LED arrays for uniform irradiance distribution to be more efficient than other regular distributions such as a square grid [26][43]. A cost breakdown was calculated for the LEDs, halogen lamps, heat sink, machined housings, and some structural equipment costs, with a grand total of just under $600, providing a rough guideline for this work. Notably, however, the control system and power supply components were not included in the cost. An illustration of the simulator is shown in Figure 4.7.

Another detailed LED-based simulator design process was given by Bazzi et. al. in [9], with special attention given to the current control system. 6 colors of LED were chosen: UV, blue, cyan, green, neutral white, and warm white. The reference spectrum of AM1.5G was chosen, as the focus of the design was terrestrial photovoltaic testing. The simulated spectrum met class B spectral match requirements, and an extended design utilizing multiple colors of NIR LEDs was shown to have the potential to improve the spectral match to class A [9].

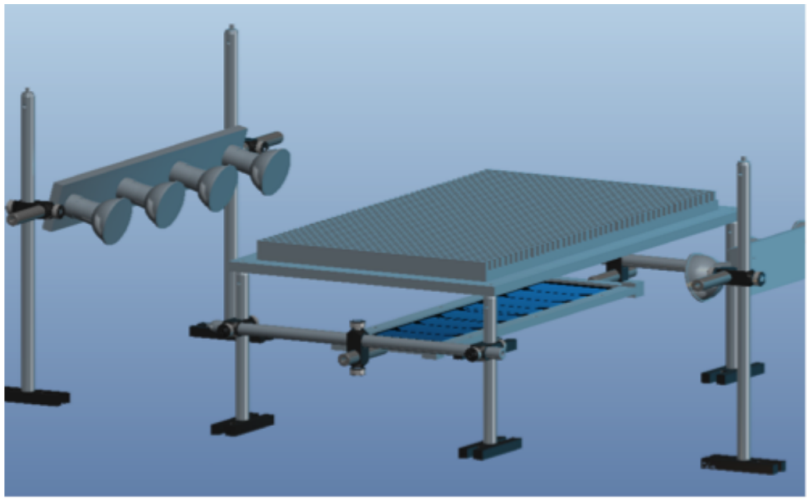

Figure 4.7: Kim et. al. Solar Simulator Layout [26]

A desired test plane of 15 x 15 cm was established, and used to calculate required total power to achieve one terrestrial solar constant on the wavelength range 400-1100 nm. ASTM E927-05 was used for classification, so it is again noted that this older standard required 36 spatial test positions instead of the current minimum of 64. The geometry was designed by first using previous research such as [43] to limit the optimization space to geometric patterns, and simulating several options to find a roughly optimal solution. A hexagon with one central point resulted in the most uniform predicted irradiance distribution, in agreement with [26] and [43]. Detail of this configuration is shown in Figure 4.8.

The resulting simulated spatial non-uniformity met class C requirements over the central 10 x 10 cm portion of the test area. Current-mode control was implemented through Matlab/Simulink. Hall effect sensors were used to measure the current in each string. An experimental prototype was constructed, and spatial non-uniformity was photographically evaluated. Class C requirements were met on the central 10 x 5 cm region of the test plane. In addition, the total required power was reported to be 45 W, and the total cost to be $1500.

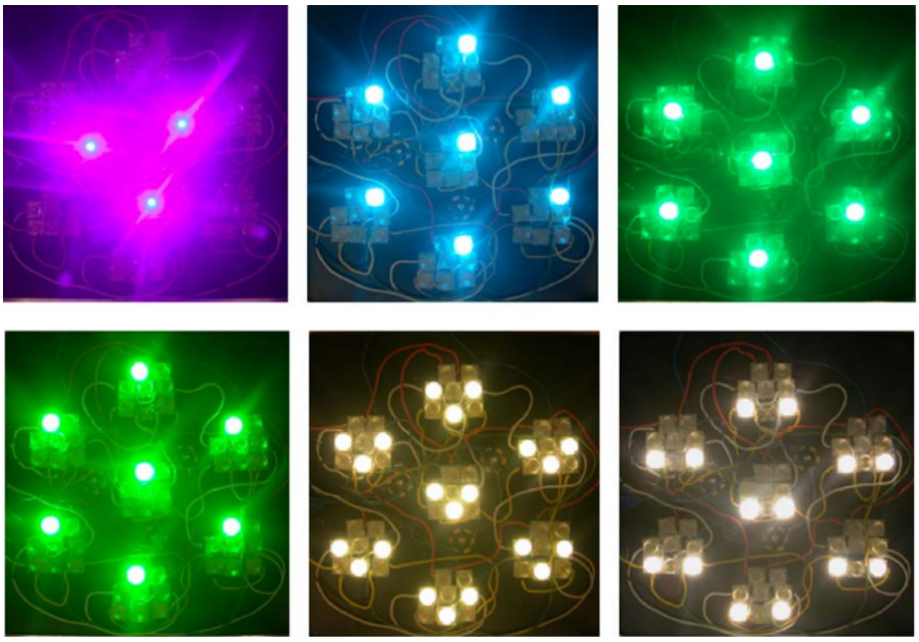

Figure 4.8: Detail of Bazzi et. al. Prototype Simulator LED Array [9]

In addition to these discussions of solar simulation with LED arrays, valuable insights are available from literature on the design of LED arrays in general, for purposes such as indoor lighting fixtures.An in-depth investigation of spatial non-uniformity was conducted by Moreno et. al. in [43], using the optical model described by Eqs. 4.2 and 4.3 previously. The focus of this paper was to calculate the required spacing of various array geometries to ensure a maximally flat condition at the center of the irradiated area, calculated by setting the second derivative of irradiance equal to zero at this point. Lastly, Yang et. al. in [58] outlined a control system for an LED array that used unique pulse width modulation frequencies for each LED, so that a single monitor cell could track the brightness of each one individually by decomposing the signal. This information was used to adjust each LED's brightness individually to maintain a set irradiance distribution, but is equally applicable to a set spectrum.

Chapter 5

SIMULATOR DESIGN

5.1 Spectrum and LED Selection

The first step in designing this LED-based simulator was naturally to choose the LEDs. To do so, the relevant wavelength range and spectral bins had to be determined. As mentioned in section 3.2, the range required for ASTM E491 includes the range required for ASTM E927, so the wavelengths of interest are thus 250-2500nm. The measurement bandwidths of Table 3.4 for Class B translate to the bins shown in the first column of Table 5.1. The spectral match requirement from ASTM E491 is shown for each bin. Recall that the E927 requirement is $0.40 <= R_{SM} <= 2.00$ for all bins. Table 5.1 also shows the corresponding irradiance from each bin, obtained by numerically integrating the AM0 spectrum of ASTM E490 [5], as well as this irradiance normalized to the integral over the whole 250-2500nm range.

It was determined that, in lieu of high-resolution spectroradiometry, choosing one LED per bin was the most straightforward way to ensure that the spectral match could be tuned appropriately. Due to a lack of affordable, high-power options, it was decided the 300-350 nm bin could remain unfilled, since a good spectral match classification is still achievable without it. The bins line up almost exactly with those of ASTM E927 in the UV and visible region, but are slightly different in the IR. However, it was also determined that high-power IR LEDs above 1000 nm are prohibitively expensive, compared to the ease of using an incandescent lamp already present in the space environments lab facility. This is due to the very low power output of these LEDs. In the 1000-1500 nm range, the two best options found would

have either required 21 individual LEDs for over $900, or 42 LEDs for over $500. In the 1500-2000 nm range, the best option found would have required 56 LEDs for just under $700. Considering the total number of LEDs of all wavelengths in the final design was 56, this is clearly disproportional.

By instead using an incandescent bulb at no extra cost, the IR bins will all be determined by the same light source's spectrum, so the exact bin boundaries are less important, and the blackbody-approximating nature of incandescent lighting should provide a reasonable spectral match in the infrared regions. The seven LEDs chosen for the wavelength bins are also shown in Table 5.1. Each was chosen for a good combination of desirable peak wavelength, high output power, and low cost. Additionally, the Luminus 280 nm UVC LED minimizes the risk of erythema and conjunctivitis due to the location of its peak wavelength at the minimum of the spectral relative effectiveness of UVC light at causing these conditions. This curve, produced from data in [6], is illustrated in Figure 5.1, along with the lower and upper bounds of the 250-300 nm wavelength bin. The 280nm wavelength is also ideally situated to prevent ozone generation, as can be seen in Table 3.6.

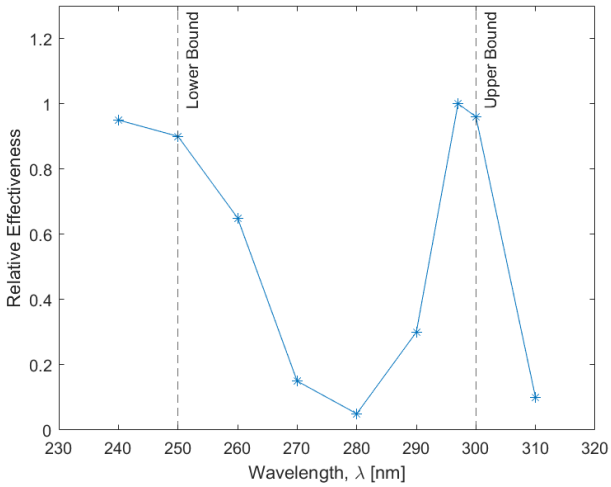

Figure 5.1: Effectiveness of UVC in Causing Erythema and Conjunctivitis [6]

Table 5.1: ASTM E491 Spectrum Design Bins [6]

Wavelength Bin (nm)	**E491 R_{SM} Requirement**	**E490 Integrated Irradiance ($\frac{W}{m^2}$)**	**E490 Irradiance as % of Total**	**Light Source Chosen**
250-300	0.35-1.65	12.66	0.96	Luminus XST-3535-UV 280nm [39]
300-350	0.35-1.65	39.22	2.98	
350-400	0.35-1.65	52.64	3.99	Luminus SST-10-UV 385nm [38]
400-500	0.50-1.50	186.21	14.13	Cree XLamp XP-G3 Royal Blue
500-600	0.50-1.50	184.89	14.02	Lumileds Luxeon C Green
600-700	0.50-1.50	159.00	12.06	Cree XLamp XP-G3 Photo Red
700-850	0.35-1.65	180.36	13.68	Luminus SST-10-FR Far Red
850-1000	0.35-1.65	130.80	9.92	Lumileds Luxeon IR 940nm
1000-1500	0.20-1.80	236.92	17.97	Philips 125W Incandescent, 2700K
1500-2000	0.20-1.80	96.72	7.34	Philips 125W Incandescent, 2700K
2000-2500	0.20-1.80	38.92	2.95	Philips 125W Incandescent, 2700K
Total	8 must qualify	1318.31		

In Kim et al [26], Matlab's *fmincon()* function was used to optimize the spectral match, using a cost function of the mean square distance between the simulator's spectral irradiance function, E_λ, and AM0 as given in ASTM E490-00a. The normalized spectral irradiance curves of each LED were used to calculate "intensity multipliers" that scaled the normalized curves to the optimal value to match AM0 at one solar constant when combined and integrated. A similar approach was implemented here: *fmincon()* was used to minimize the cost

$$J = \Sigma(R_{SM} - 1).^2 \tag{5.1}$$

as a function of constants multiplied to each E_λ curve so that each wavelength bin's spectral match would be as close as possible to 1. The IR lamp was modeled as a blackbody at 2700K using Eq. 2.4. Because the test plane is located close to the light source, the spectral distribution will not change between the exitance of the lamp and the irradiance on the test plane due to atmospheric absorption (this requires distances on the order of km). The normalized exitance and irradiance curves can be considered equivalent as a result.

The calculated optimized spectral irradiance compared to the AM0 spectrum is shown in Figure 5.2, along with the individual normalized E_λ curves. The boundaries of the wavelength bins are also highlighted. At first glance, the spectra appear markedly different. However, note that, as designed, there is one peak in each of seven wavelength bins. The irradiance integrated across each of these intervals is the quantity of interest, so the apparent difference in spectra is not so drastic as it first appears.

Using the optimized multipliers, the scaled spectral irradiance curves were integrated to find the total output from each LED wavelength. Eq. 3.1 from ASTM E927 was then used to calculate the theoretical spectral match, shown in Table 5.2 for both

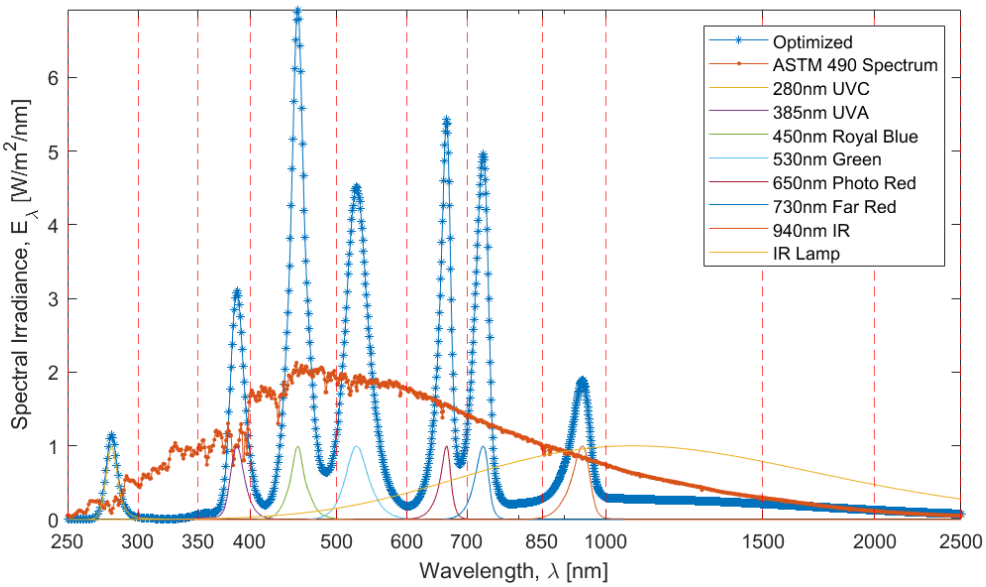

Figure 5.2: Theoretical Optimized E_λ of Simulator

E491 and E927. Eq. 3.7 from ASTM E491 does not include the normalization step of Eq. 3.1, but since only the ratio between the simulator and the AM0 spectrum is relevant, the results of both equations are the same. The difference in the bins used results in the disparities in Table 5.2. Note that the IR lamp's output is not finely adjustable, as this optimization assumed - the spectral match of all bins above 800 nm is likely to be somewhat different when measured experimentally.

5.2 Array Geometry and Spatial Uniformity

Given the test plane of 10x10 cm^2 area and the total irradiance used to normalize the E_λ integrals, the required output power for each LED was calculated. As a first-order estimate of the number of LEDs needed, the optical transfer efficiency of the system was assumed to be $\eta = 40\%$, as recommended in [29]. The wavelength needing the most individual LEDs was 530 nm (Green), with a total of four required. The final number of LEDs was initially chosen to fit a hexagonal array pattern for good spatial

Table 5.2: Predicted R_{SM} of Simulator

E491 Bin (nm)	R_{SM}	**E927 Bin (nm)**	R_{SM}
250-300	1.01		
300-350	0.03		
350-400	1.01	350-400	1.01
400-500	1.00	400-500	1.00
500-600	1.00	500-600	1.00
600-700	1.00	600-700	1.00
700-850	1.00	700-800	1.33
850-1000	1.00	800-900	0.34
1000-1500	0.54	900-1100	0.91
1500-2000	0.87	1100-1400	0.55
2000-2500	1.28		
# Qualifying	>8 (Class B)		7 (Class U)

uniformity. Unfortunately, the hexagon with a center point analyzed in [26], [9], and [43] was not possible due to the need to incorporate the IR lamp into the array of LEDs. A hollow ring was the next best option according to the results of [43]. It was decided that at twice as many LEDs as required, the simulator should have a wide enough max power margin for future versatility. For simplicity of construction, the same number of LEDs should be used for each wavelength. Thus, it was decided to construct the LED array out of eight LEDs of each of the seven wavelengths - a total of 56 in all.

Numerical simulations of a hollow ring of eight LED locations, or "nodes," each containing one LED of each of the seven wavelengths, were conducted. Moreno et. al. [43] provides a general expression for the irradiance across an x, y plane separated by a distance z from the plane of an LED located at coordinates (x_0, y_0):

$$E(x, y, z) = \frac{z^m L_{LED} A_{LED}}{[(x - x_0)^2 + (y - y_0)^2 + z^2]^{(m+2)/2}} \tag{5.2}$$

where L_{LED} is the LED's radiance, A_{LED} is the LED's surface area, and m is determined by the LED half angle according to Eq. 4.3. The equivalency

$$L_{LED} A_{LED} = \frac{\Phi_{LED}}{2\pi} \qquad [\frac{W}{sr}] \tag{5.3}$$

was used to modify the numerator of Eq. 5.2 for this work, since the LED datasheets provide radiant power output but not radiance information. Recall that 2π steradians is the solid angle of a hemisphere - the total solid angle that an LED emits into. Thus, dividing power by 2π is equivalent to multiplying radiance by surface area, and the result is the maximum intensity value ($\theta = 0°$). The cosine law scaling of intensity with angle is accounted for by the value of m.

For the specific geometrical conditions of a coplanar ring of point sources, the following expression derived from Eq. 5.2 and given in [43] for the irradiance from a ring of $N > 3$ LEDs was used:

$$E(x,y,z) = z^m \frac{\Phi_{LED}}{2\pi} \Sigma_{n=1}^{N} [[x - \rho\ cos(\frac{2\pi n}{N})]^2 + [y - \rho\ sin(\frac{2\pi n}{N})]^2 + z^2]^{-(m+2)/2} \quad (5.4)$$

where ρ is the radius of the ring. Figure 5.3 shows an example result of this equation.

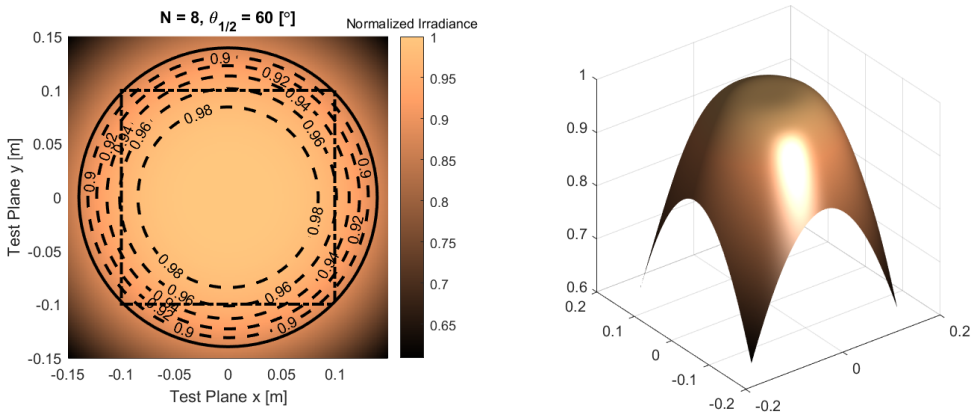

Figure 5.3: Normalized Irradiance of a Ring of 8 LEDs

A rough estimate of the radius was used for preliminary sizing. The actual radius of the array of LED nodes was determined by the size of the IR lamp, which must fit in the center. The structural materials used to mount the LED nodes were designed using imperial units due to a lack of metric options. The final radius was $rho = 3.65$ in, or ≈ 9.27 cm. The maximally flat condition for z-spacing, radius, and half-angle for a ring of LEDs given in [43] is

$$\rho_0 = \sqrt{\frac{2}{m+2}}\ z \quad (5.5)$$

For this simulator, the LED half-angles and radius are the input variables, so rearranging for height and substituting the definition of m gives

$$z = \frac{\rho}{\frac{2}{\frac{-ln\ 2}{ln(cos\ \theta_{1/2})}+2}} \tag{5.6}$$

Using this equation, the ideal array mounting heights shown in Table 5.3 was calculated for each LED based on the $\theta_{1/2}$ given in its datasheet.

Table 5.3: Ideal Array Height Above Test Plane

LED	$\theta_{1/2}$ [°]	z **[cm]**
280 nm UVC	30	17.12
385 nm UVA	65	10.98
450 nm Royal Blue	65	10.98
530 nm Green	85	9.91
650 nm Photo Red	62.5	11.16
730 nm Far Red	45	13.11
940 nm IR	30	17.12

Since all the LEDs will be mounted at the same height, a value or compromize must be chosen from among the options of Table 5.3. The range of ideal heights is significant - simply using an average value is unwise. The maximum required z-spacing of 17.12 cm was chosen for the actual design because, at distances closer than the ideal, the irradiance of a ring becomes just that - a bright ring with a dark center. In contrast, at distances further than the ideal, the flatness decreases, and the edges begin to grow darker relative to a bright center. It is important to maintain maximum brightness at center of the test plane by remaining at or above the ideal height. Setting the array below the ideal height of even one LED risks altering the uniformity of the spectral match across the test plane by introducing a dark spot in the irradiance of that LED wavelength and not others. The downside of choosing the maximum height is that

transfer efficiency is guaranteed to decrease (irradiance is proportional to the inverse square of distance), and a valuable future modification to this simulator would be the addition of a small optic to each LED to focus them all to the same $\theta_{1/2}$.

The predicted irradiance distribution calculated with Eq. 5.2 resulting from all 56 LEDs at the eight node locations with z-spacing of 17.12 cm is shown in Figure 5.4. The IR lamp is also included in this calculation. Since the bulb is mounted in a reflective housing, it does not radiate isotropically as a blackbody, but rather in a manner similar enough to the Lambertian distribution of LEDs that it can be modeled as one, with $\theta_{1/2} = 45°$, and radiant power output equal to its electrical power consumption of 125 W multiplied by the typical 10% efficiency of incandescent bulbs [31].

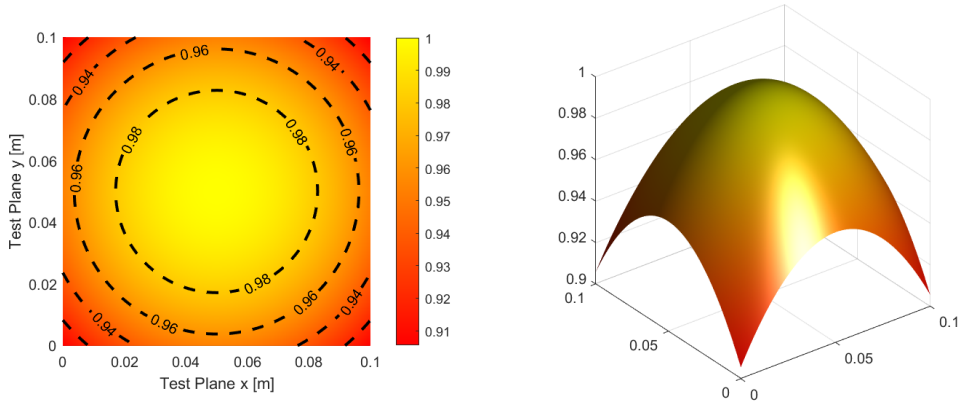
Test Plane y [m]
Test Plane x [m]
0.96
0.94
0.98
0.96
0.94
0.98
0.96
0.94
0.98
0.96
0.94

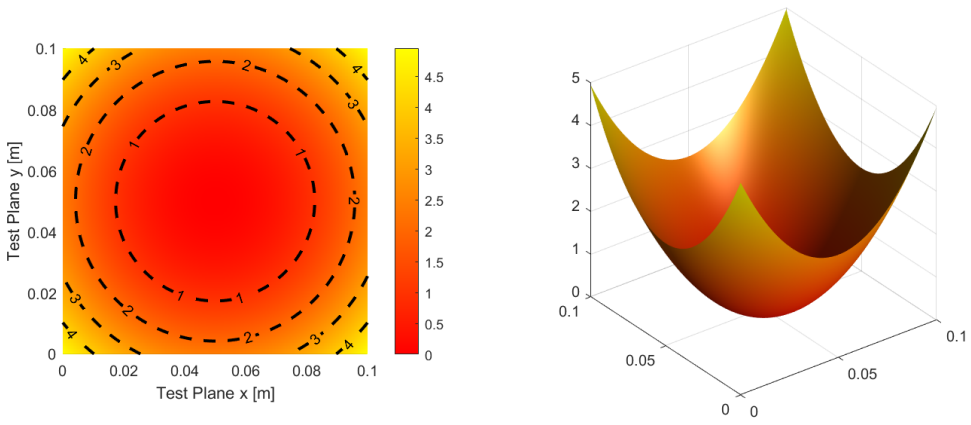

Figure 5.5: Predicted Spatial Non-Uniformity

Using Eqs. 3.2 and 3.4, the predicted spatial uniformities shown in Table 5.4 were calculated.

Table 5.4: Predicted Spatial Uniformity Classification

	E491, Eq. 3.4	**E927, Eq. 3.2**
S_{NE}	4.88%	4.96%
Classification	Class B	Class B

5.3 Temporal Instability and Pulse Width Modulation

Based on the method used in Yang et. al. [58], it was determined that pulse width modulation (PWM) of the LED currents would not only allow straightforward software control of irradiance, but through the use of spectral analysis provide a method of evaluating the spectral match with a resolution equal to the LED FWHM without requiring the use of a spectroradiometer. By pulsing each wavelength of LEDs at a unique frequency, the PWM frequency can be correlated with the wavelength of optical radiation.

ASTM standards E927 and E491 discuss both steady-state and pulsed solar simulators. The criteria for qualifying as a steady-state simulator for E927 is that the average irradiance be steady over time periods longer than 0.1 s [7], while for E491, the time period must be longer than the thermal time constant [6]. From the time period requirement of E927, it can be seen that any such PWM waveform must have a frequency much higher than 10 Hz. Ultimately, temporal instability depends on random noise, the response time of the control law, and the summed PWM waveforms of the LEDs. The best possible temporal instability is difficult to predict, but the instability was relatively simple to measure experimentally and can be fine-tuned with the control law if necessary.

IEEE Standard 1789-2015 [23] provides recommended practices for pulsed LED lighting in order to avoid adverse health effects. The flicker fusion threshold for most people is between 60-100 Hz - below this frequency, flicker is visible, while above, it is invisible to the human eye [23]. Visible flicker is relatively well known as presenting a risk of inducing seizures in those with photosensitive epilepsy. Invisible flicker can cause negative effects such as migraines, headaches, and stress - indoor flourescent lighting prior to the 1990s was a common cause of these symptoms in office workers [23]. The common adaption of high-frequency electronic ballasts for flourescent lighting largely eliminated these complaints. However, LED lighting that flickers at household AC power frequencies of 120 Hz has reintroduced such hazards, and standards such as IEEE 1789 exist to ensure minimization of these risks [23]. The recommended operating practices of IEEE 1789 are given in Figure 5.6.

Since each LED in this simulator design will pulse at a different frequency, the effective modulation percentage is not 100%, as it would be if just one LED wavelength was operating. It is expected to be in the range 25-75%, since, as can be seen in column four of Table 5.1, the four visible LEDs each comprise about equal percentages of the

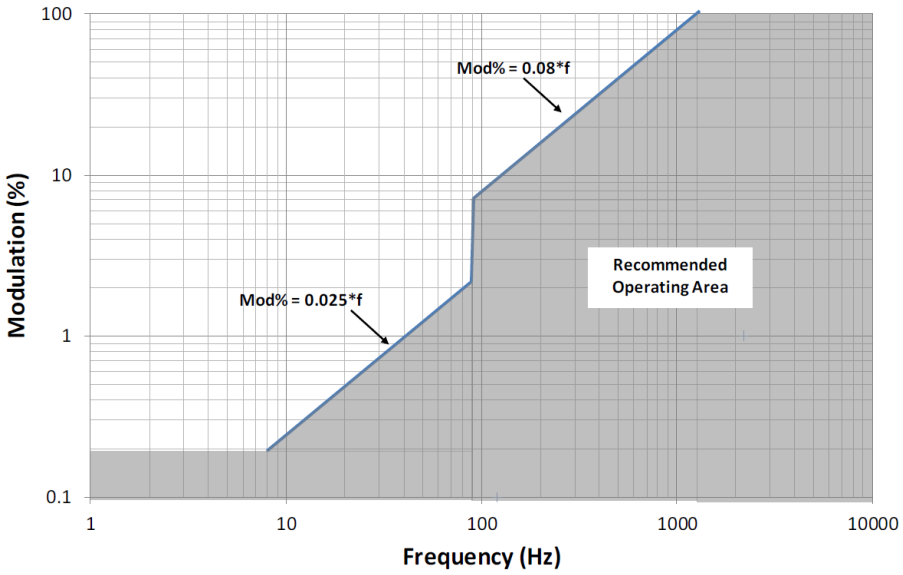

Figure 5.6: IEEE Standard 1789-2015 Recommendations [23]

power in the visible spectrum. Accordingly, the lowest recommended LED frequency for this system would be 1000 Hz according to Figure 5.6.

NXP Semiconductors' PCA9685 PWM controller IC [49] was chosen for its ability to programmatically select the PWM frequency, its maximum frequency of 1526 Hz, its I^2C control, and low cost. It was initially hoped that all of the simulator's PWM signals would have frequencies between 1000-1500 Hz. Unfortunately, during testing of the simulator, the DAQs used were discovered to have a peak in random noise at 3000 Hz, extending down to 1000 Hz. Additionally, the PCA9685's selectable frequencies are logarithmically spaced, favoring low frequencies, and there are in fact fewer than seven distinct available frequencies above 1000 Hz.

A combination of both of these effects drove the chosen PWM frequency range to 431-755 Hz in implementation; these are shown in Table 5.5. This could put the simulator on either side of the line in Figure 5.6. Protective dark safety glasses, shown to be necessary in Table 3.6 previously, are also important to protect against the effects of this system's particular flicker characteristics. This is because the negative health

effects of flicker are much less severe if the light source's illuminance can be decreased [23], such as by wearing dark glasses. Additionally, due to small variations in each PWM chip's internal reference clock, the measured output frequencies differ slightly from the commanded ones; this is also shown in Table 5.5.

Table 5.5: LED PWM Frequencies

LED	Commanded Frequency (Hz)	Measured Frequency (Hz)
280 nm UVC	431	435
385 nm UVA	465	465
450 nm Royal Blue	503	496
530 nm Green	549	544
650 nm Photo Red	604	581
730 nm Far Red	671	636
940 nm IR	755	-

In order to analyze the periodic irradiance pulses using discrete voltage data points from a photodiode, a fast fourier transform (FFT) must be used. By the Nyquist sampling theorem, all the information in a periodic signal can be recovered by sampling it at twice its frequency. Thus, for the desired PWM max frequency of 1.5 kHz, the signal must be sampled at at least 3 kHz. The space environments lab contained several currently unused NI USB-6008/6009 DAQ units [45][46]. The 6008 models have a maximum aggregate sampling frequency of 10 kHz, and the 6009 has a maximum aggregate sampling frequency of 48 kHz. 10 kHz was thus chosen as the default sample acquisition frequency, to have a comfortable margin above the 3 kHz minimum. Since the frequencies were ultimately decreased to 431-755 Hz, the margin is even greater.

When taking the FFT of a voltage waveform sampled at frequency F_s, after adjustment and scaling, the output is a number of voltage values corresponding to the

Fourier series coefficients, ranging from the DC component at index 0 to the Nyquist frequency, $Ny = \frac{F_s}{2}$ [12]. The frequency spacing (or resolution) between the output points is given by [12] as

$$\Delta f = \frac{F_s}{N} \tag{5.7}$$

where N is the number of data points used. To compute the number of data points required for a desired frequency resolution, rearrange Eq. 5.7 for N. To produce an FFT with $\Delta f = 1$ Hz with $F_s = 10$ kHz, $N = 10,000$. This corresponds to 1 second of time history, which means that there will be about this much lag between a change in the data and its full reflection in the FFT. As a result, a proportional control law with 1 Hz updates was implemented, so that an increase or decrease in brightness from one command will be reflected in the FFT by the next time the control law updates. Faster updates could lead to oscillations without a change to PD or PID control and careful adjustment of gains, which is a potentially unnecessary complication over simple proportional control.

A generic PWM voltage waveform is shown in Figure 5.7. It has nonzero high and low voltages V_H and V_L respectively, transitioning between the two states at time t_p during a period of $2T$. The duty cycle, D, is defined by the ratio of time spent at V_H to time spent at V_L, as $D = \frac{t_p}{T}$. The PWM wave can be represented as a piecewise defined function

$$f(t) = \begin{cases} V_H & -t_p < t < t_p \\ V_L & otherwise \end{cases} \tag{5.8}$$

To understand this function's FFT representation, its Fourier series was calculated. By first noting that it is an even function, the Fourier cosine series was used:

$$f(t) \approx \frac{a_0}{2} + \Sigma_{n=1}^{\infty} a_n \, cos\frac{n\pi t}{T}, \quad a_n = \frac{2}{T}\int_0^T f(t) \, cos\frac{n\pi t}{T} dt \tag{5.9}$$

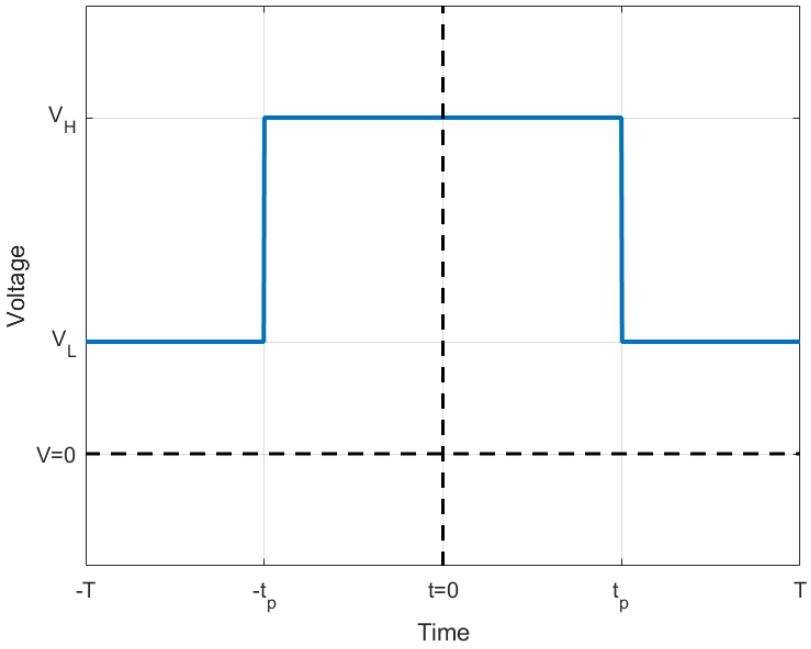

Figure 5.7: Generic PWM Waveform, With $P = 2T$ and $D = \frac{t_p}{T}$

After substituting Eq. 5.8 into Eq. 5.9, integrating, and using $P = \frac{1}{f}$ to replace T with $\frac{1}{2f}$, the following expression was obtained:

$$f(t) \approx V_H D + V_L(1-D) + \Sigma_{n=1}^{\infty} \frac{2}{n\pi}(V_H - V_L)\ sin(n\pi D)\ cos(2n\pi ft) \qquad (5.10)$$

Due to the vertical discontinuity at the transition between low and high voltages, it is composed of an infinite series of terms. The coefficients of this cosine series will appear as outputs of the FFT, and these are tabulated in Table 5.6. Column 3 shows the

Table 5.6: FFT Coefficients of PWM Waveform

	FFT Coefficient	$V_L = 0$	**Sum of PWM**	**Voltage Form**
A_0	$V_H D - V_L(1-D)$	$V_H D$	$V_0 + \Sigma V_k D_k$	$V_0 = A_0 - \Sigma V_k D_k$
A_1	$\frac{2}{\pi}(V_H - V_L)\ sin(\pi D)$	$\frac{2}{\pi} V_H sin(\pi D)$	$A_k = \frac{2}{\pi} V_k sin(\pi D_k)$	$V_k = \frac{\pi A_k}{2sin(\pi D_k)}$
A_n	**Generic coefficient:** $\frac{2}{n\pi}(V_H - V_L)\ sin(n\pi D)$			

coefficients under the condition $V_L = 0$. Column 4 then shows the coefficient when, instead of only analyzing one PWM signal, the analysis is of a composite waveform composed of an arbitrary number of PWM signals along with a constant offset. This corresponds to the conditions of this thesis, where multiple pulsed LEDs illuminate a photodiode along with an incandescent bulb. The final column then shows the expression in column 4 solved for the voltage responsible for producing that FFT coefficient. This final column comprises the equations implemented with LabView as part of the control loop.

5.4 Electrical Power and Control

Electrical power design was carried out to balance peak power needs with average power draw. It was desired for the current through the LEDs during a pulse to equal the max allowable constant current for the LEDs. This ensured that the duty cycle can approach 100% without risk of damaging the LEDs. The forward voltage drop at this current was obtained from the LED datasheets, and multiplied by eight (the number of LEDs in each string). However, since the 280 nm UVC LED string resulted in a total voltage drop of close to twice that of the rest, that string was split into two substrings of four LEDs each.

The voltage drop of the LED strings, now totaling eight in number, is shown in Table 5.7 along with the peak (pulse) currents. A common 30 V power supply for each string was an obvious choice. The remaining voltage not dropped across the LEDs was assumed to cross a single current-setting resistor, with resistance calculated to produce the desired current. These resistances are also shown in Table 5.7. The two 280 nm LED strings were each given their own resistor, since otherwise the current balance between them would be determined by the nonlinear characteristics of the

LEDs. These resistors were constructed of multiple smaller resistors in series, each with an appropriate power dissipation rating. The handheld multimeter available could only measure these resistances to 0.1 Ohm precision, but this results in only 5% uncertainty in the current, which is acceptable.

Lastly, the total peak current, also shown below, and power consumptions were calculated. The peak power consumption was predicted to be 290 W, while the average power consumption based on the expected duty cycle to produce the desired total irradiance was 90 W. The overall radiant efficiency of the system, based on the individual LEDs at their respective duty cycles and currents, was predicted to be 20%.

Table 5.7: LED String Power Calculations

LED	**LED Current (A)**	**String Voltage (V)**	**Resistor Voltage (V)**	**Resistor Chosen (Ohm)**	**Predicted Duty Cycle (%)**
280 nm UVC (x2)	0.50	26.4	3.6	7.2	60.3
385 nm UVA	1.50	27.2	2.8	1.8	5.1
450 nm Royal Blue	2.00	25.6	4.4	2.1	13.6
530 nm Green	1.05	24.4	5.6	5.3	87.0
650 nm Photo Red	1.50	21.2	8.8	5.8	18.9
730 nm Far Red	1.50	23.6	6.4	4.2	35.5
940 nm IR	1.00	23.2	6.8	6.7	29.7
Total Current: 9.55 peak, 2.98 ave.					

An Agilent 6038A DC power supply [3] available in the lab was chosen as the main power source based on availability and its output capabilities. The average power draw was well within its ability, though not the peak power draw. To mitigate this,

a 50 mF capacitor bank was sized to smooth the current draw required of the supply, and constructed of spare high-voltage components. Both are shown in Figure 5.8. For ease of measurement, it was decided that the negative voltage terminal of the power supply be used as a ground reference for all devices. A circuit diagram of the power supply and the LED strings is shown in Figure 5.9.

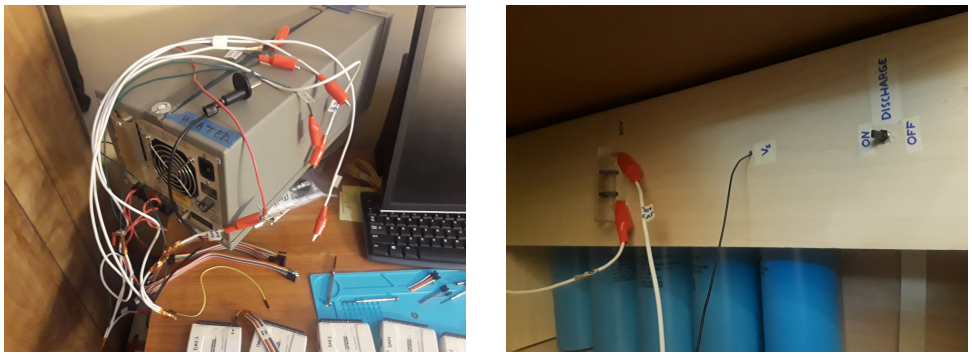

(a) (b)

Figure 5.8: (a) Agilent 6038 DC Load, (b) 50 mF Capacitor Bank

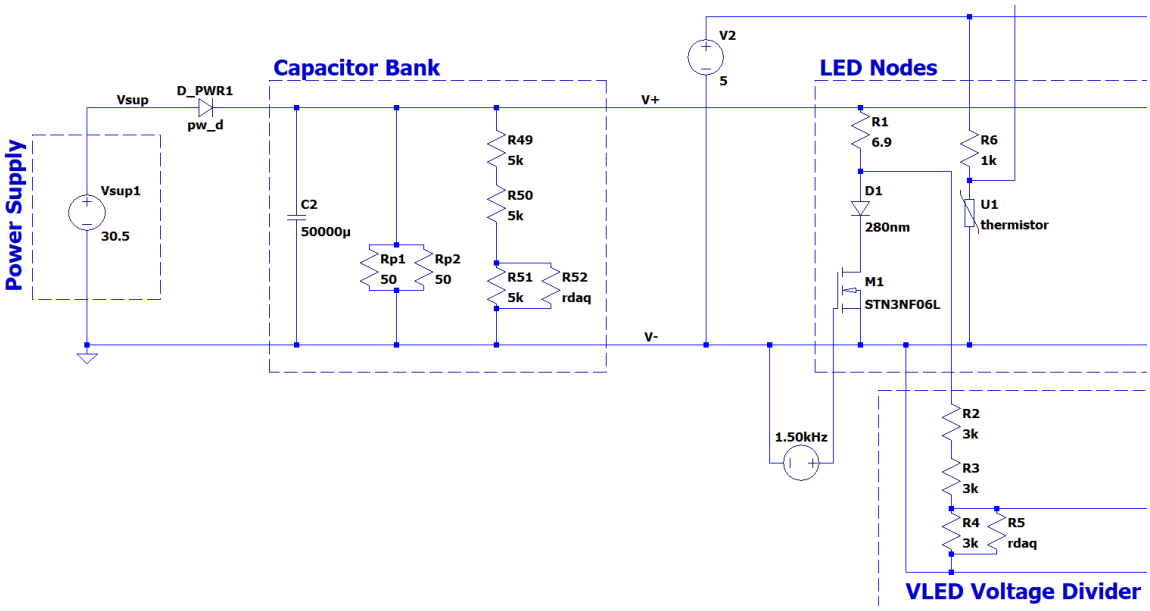

Figure 5.9: Diagram of Power Circuitry

Control of the LED duty cycle was implemented with a PID block in LabView, taking column 5 of Table 5.6 as the process variable and commanding a change in LED duty cycle as the output. The loop was set to update at a frequency of 1 Hz. Proportional

gain was set to 1, with integral and derivative gains of 0. This appeared to provide satisfactory behavior during testing. The output duty cycle was constrained to 15-85%. At duty cycles higher or lower than this, the duration of the shorter pulse (on or off, depending on whether D is close to 0 or 1 respectively) is short enough that it risks not being picked up properly at the DAQ 10 kHz sampling rate. The rate of duty cycle change was limited to a maximum of $\pm 5\%$ in an effort to limit fluctuations due to noise. The PCA9685 chips received I^2C commands from a Microchip MCP2221A USB to I^2C converter packaged on an Adafruit breakout board. LabView's Python blocks were used to call custom wrapper functions for Adafruit's CircuitPython libraries [2], which include classes for the MCP2221A as well as the PCA9685. A desktop PC was assembled for the simulator by Brandon Goddard, running Windows 10, LabView 2019, and Python 3.8.

5.5 PCB Design, Structure, and Assembly

In order to mount the various components chosen, PCBs were designed using AutoDesk EAGLE and ordered from JLCPCB [25]. Three designs were created: an LED node, a power distribution board, and a spatial array. The planning phase for soldering all components to the boards occurred in the early months of 2020. It was planned that the Cal Poly Electrical Engineering Department's reflow ovens would be used to assemble these boards quickly. Unfortunately, the COVID-19 pandemic required a change in plans as the campus transitioned to a virtual spring quarter. All components were instead soldered to the boards by hand by the author at home. This rapid adjustment would have been impossible without the generous loan of a soldering iron, hot air gun, and smoke absorber from the Cal Poly CubeSat lab by Dr. Pauline Faure. A photo of the author's home soldering setup is shown in Figure 5.10.

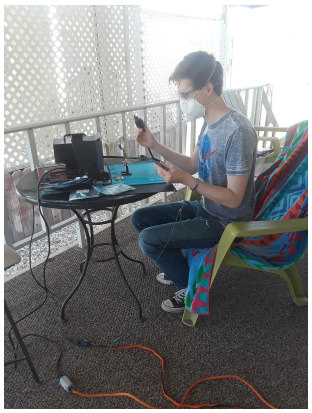

Figure 5.10: Home Soldering Setup

The LED node was designed to hold one each of the seven different LED wavelengths. Its circuit diagram and schematic are shown in Figure 5.11 along with an image of a fully assembled board in5.12. For passive thermal control, a finned aluminum heat sink was mounted to the back of each board. Since this heat sink was mounted via a screw in the center of the node, the LED locations were set as a ring surrounding it, within the footprint of the heat sink. For symmetry, an extra LED location was added, for a total of eight. This location was assigned the footprint of the 530 nm Green LED, since this was the least powerful and expected to operate at the highest duty cycle. Future work on the simulator can add another set of eight green LEDs, allowing a higher total irradiance output.

A thermistor was also added to the LED node near the green LED, because in addition to operating at a high duty cycle, this LED die was the smallest. The high power density is likely to make its operating temperature the highest of all the LEDs on the node. Thus, it was the best location from which to make temperature readings. The LabView software was programmed to turn off the simulator automatically if the temperature rises above 100° C, to prevent damage to the LEDs.

While assembling the LED nodes, it was discovered that the datasheet of the 940 nm IR LED had been misread, and the central pad of the LED die was erroneously

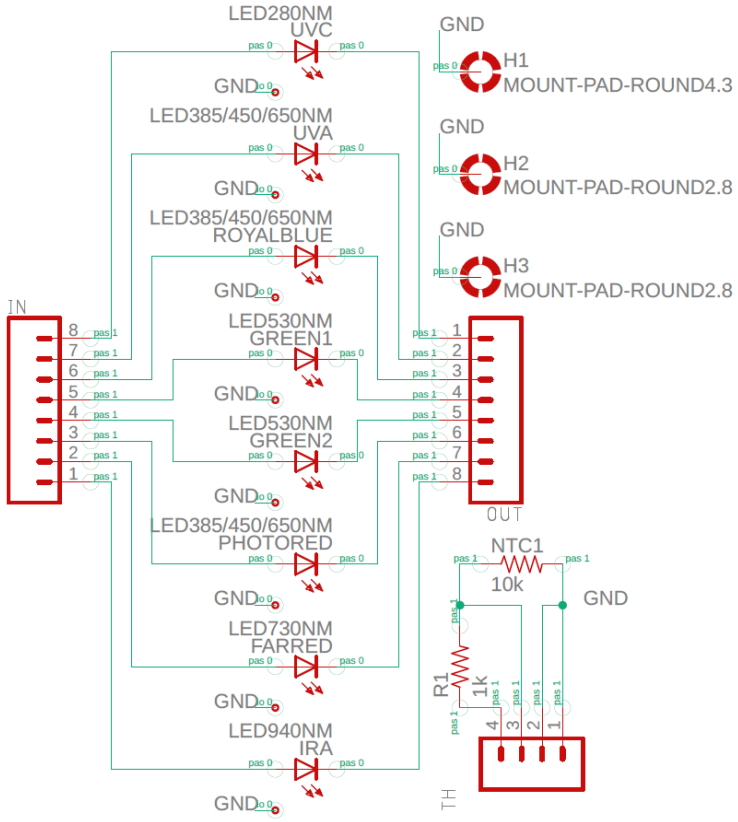

(a)

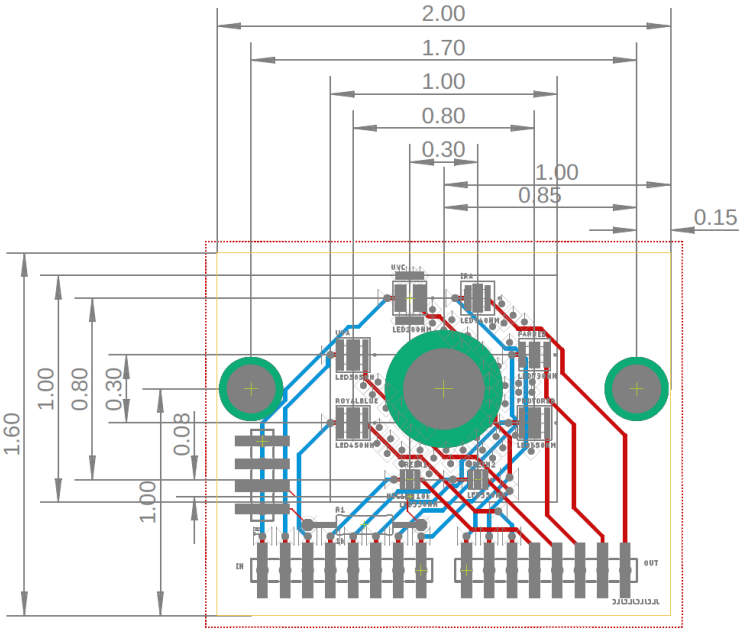

(b)

Figure 5.11: Design of LED Node: (a) Schematic, (b) PCB

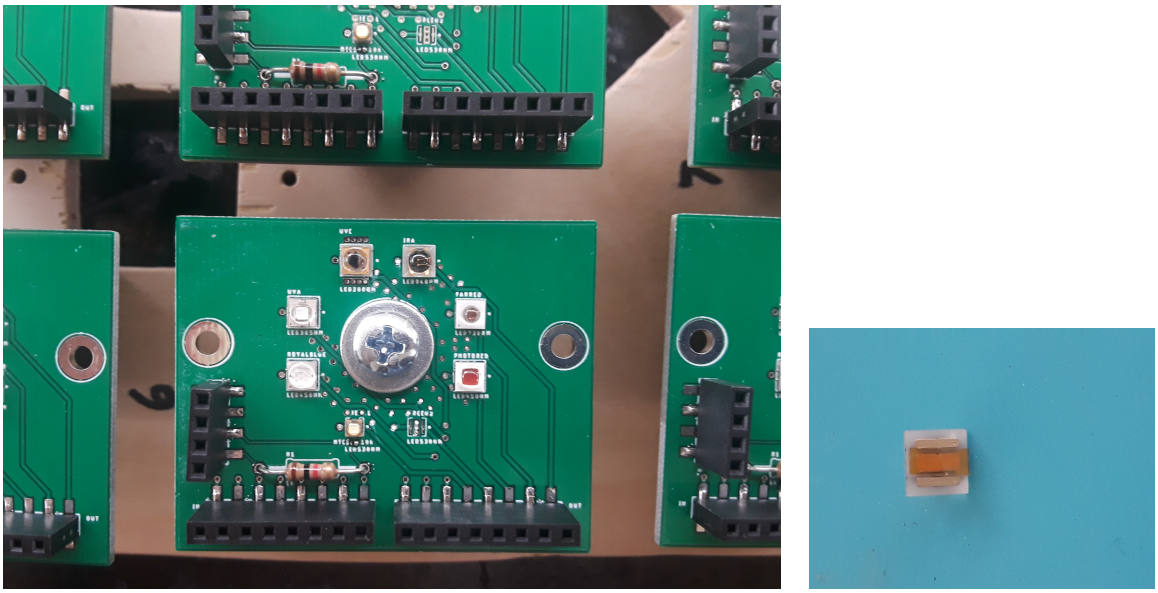

(a) (b)

Figure 5.12: (a) Assembled LED Node, (b) Kapton Tape Fix for IR LED

connected to ground on the PCB. This issue was fixed by affixing a small strip of Kapton tape, shown in Figure 5.12(b), to the central pad before resoldering, severing this connection. Since multiple thermal vias were included in the board, it is not anticipated that this fix will cause the IR LEDs to overheat.

The power board schematic and board layout are shown in Figures 5.13 and 5.14, respectively. This PCB contains seven of the PCA9685 PWM controller chips as well as seven MOSFETs to serve as voltage-controlled switches for the LED strings. Eight connections exit the board however, as the 530 nm Green line is split to accomodate the two instances on the LED nodes. It was originally intended that the power supply positive voltage (30V) attach to a screw terminal at the power board (This was changed to be the negative voltage terminal of the power supply instead, as discussed in the next paragraph). The wires of the LED strings return to this power board after passing through the LED nodes, and are split in parallel. One set is used for measuring the LED voltage drop, while the other was intended to connect to

the current-setting resistors and then to the negative voltage terminal of the power supply (GND).

Unfortunately, this author's unfamiliarity with transistors led to a flaw in the design - the MOSFETs were on the "high" side of the voltage, close to the 30V terminal. However, their gates were driven by logic-level voltage at 5 V. Thus, if the MOSFETs turned fully on, the small voltage drop across them meant that the gate-source voltage difference would be negative - a situation that would turn the MOSFETs off again. This would not allow enough voltage to be applied across the LED strings to turn them on. To work around this issue, the polarity of the power supply connection was switched, so that the 30V terminal was attached to the current-setting resistors, and the GND terminal to the power board. The MOSFETs were resoldered such that they were now on the "low" voltage side, and could fully turn on the LED strings. This was accomplished by bending one of the MOSFETs' pins, applying a strip of Kapton tape to cover one of the pads, bridging a via next to each MOSFET to one of the other pins, and soldering jumper wires directly to the pin which had been disconnected via the Kapton. The power board is shown in Figure 5.15(a) before and (c) after the fix.

Figure 5.15(b) shows damage that occurred to chip PWM7, controlling the 940 nm IR LED string. Pin A0 (bottom left in image) broke off as the chip was being soldered in place. This is one of the pins used to define the I^2C address. A small blob of extra solder was used to attempt to bridge it to pin A1, since those address bits happened to be equal. During testing, PWM7 was at best unreliable, but usually did not acknowledge I^2C commands at all. Thus, the irradiance of the 940 nm IR LED string is not present in the results. A spare PCA9685 chip was bought to use in a breadboard prototype. Desoldering it from the breakout board it is currently

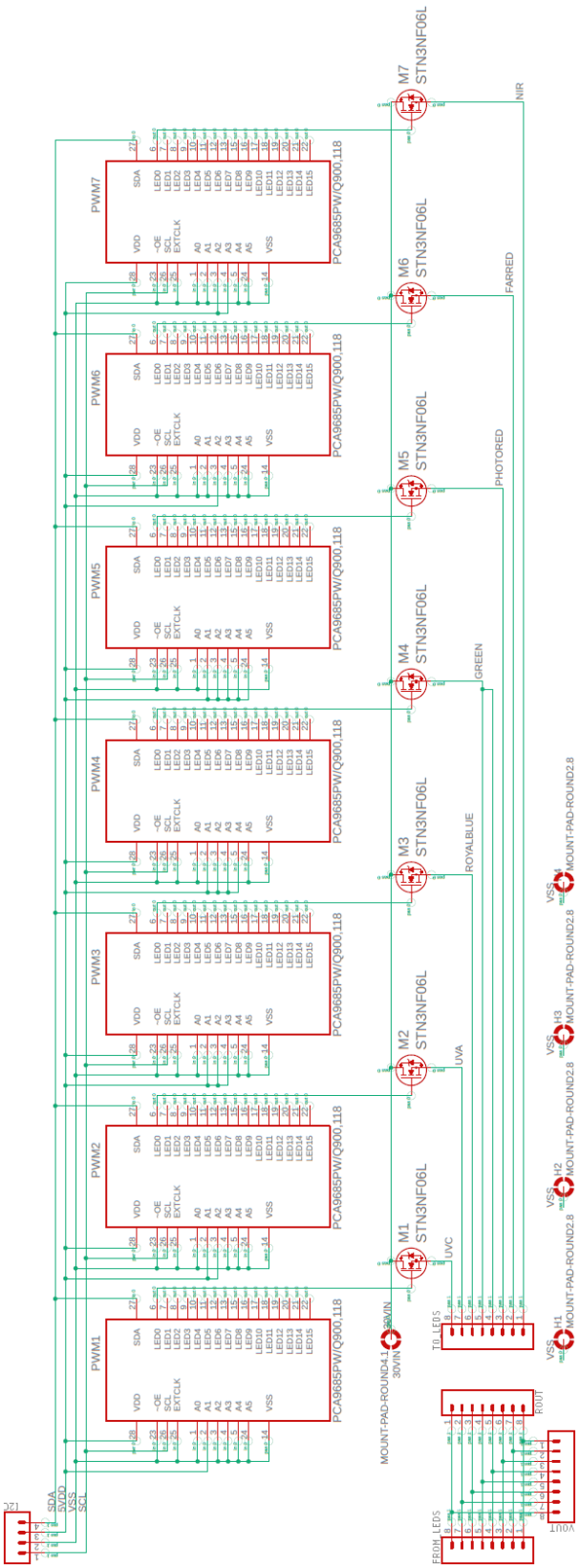

Figure 5.13: Power Board Schematic

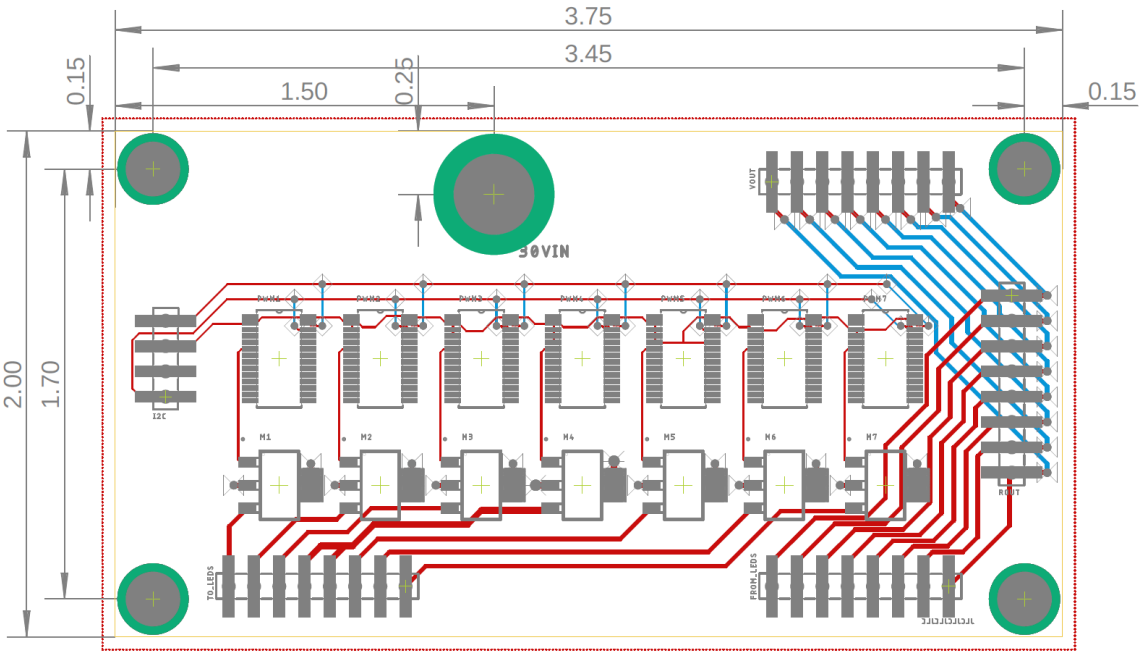

Figure 5.14: Power Board PCB Design

mounted on and resoldering it to the power board in place of PWM7 is the simplest way to resolve this problem in the future.

The schematic and board layout of the spatial array are shown in Figure 5.16 along with a picture of the assembled board in Figure 5.17. Osram SFH 2201 photodiodes [51] were used for the spatial array because they had the largest active area for a reasonable price, as well as enhanced blue and UV sensitivity The dimensions of the active area drove the selection of a 25x25 position spatial matrix. Over a 10 cm x 10 cm plane, each spatial matrix test position spans 4 mm on a side. A detector solar cell needs to cover at least half the test position area. To cover at least half the area with the above spatial matrix, a square cell must have a side length of at least ≈ 2.83 mm. The SFH 2201 is 2.85mm square, efficiently satisfying this requirement, since the 25x25 grid was chosen to fit it.

A linear array was desired, but unfortunately the outer package dimensions of the photodiode were too large to fit 25 within a 10 cm line. Two staggered lines were used

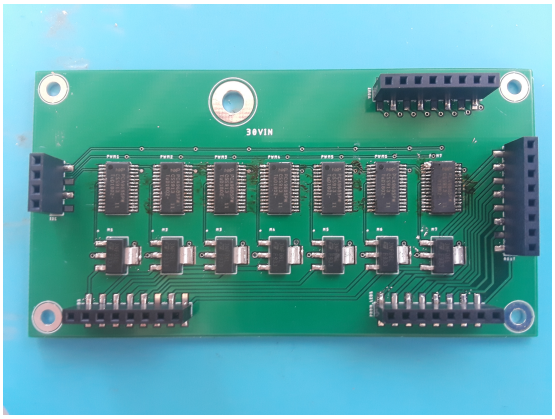

(a)

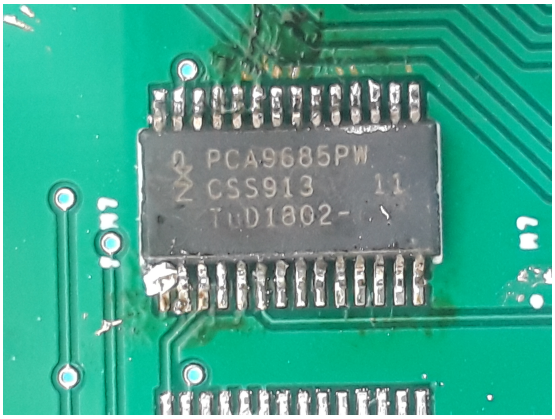

(b)

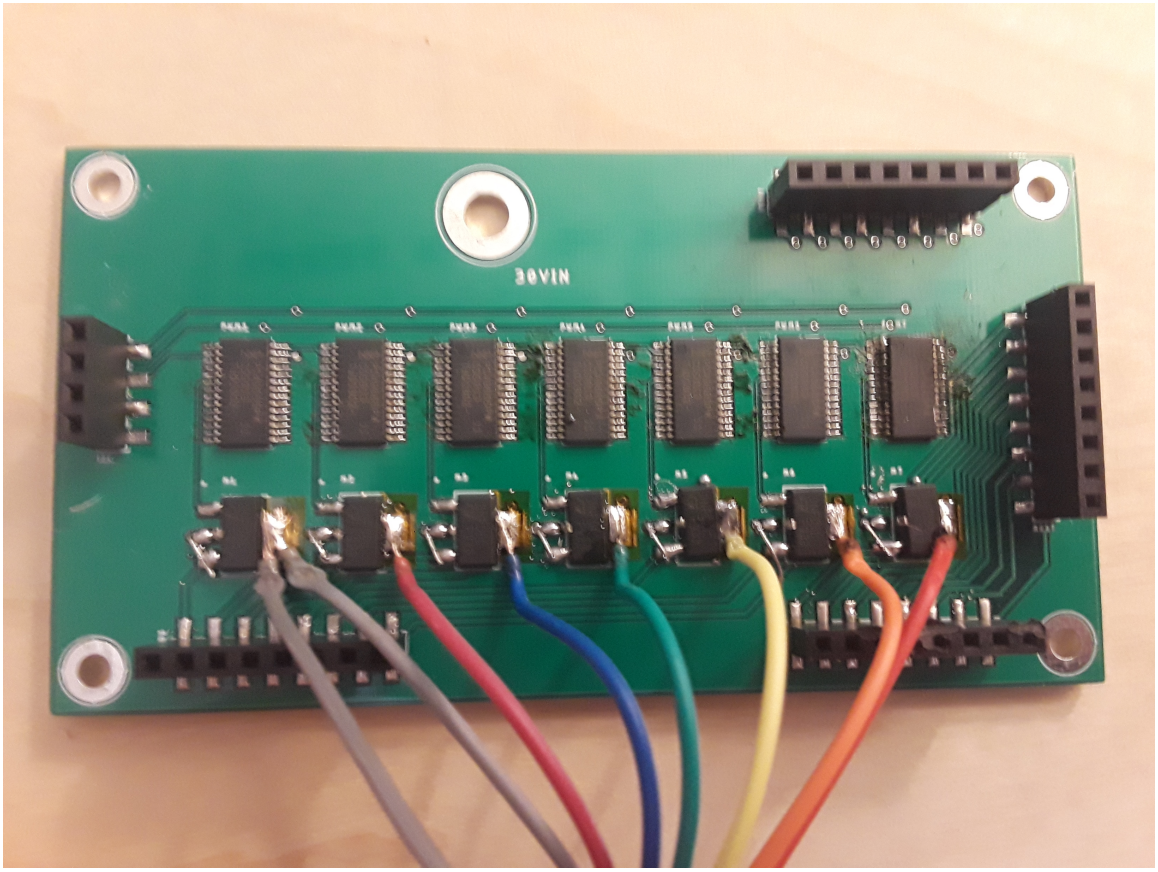

(c)

Figure 5.15: Power Board Design: (a) Before Rework, (b) Damage to PWM7 PCA9685, (c) After Rework

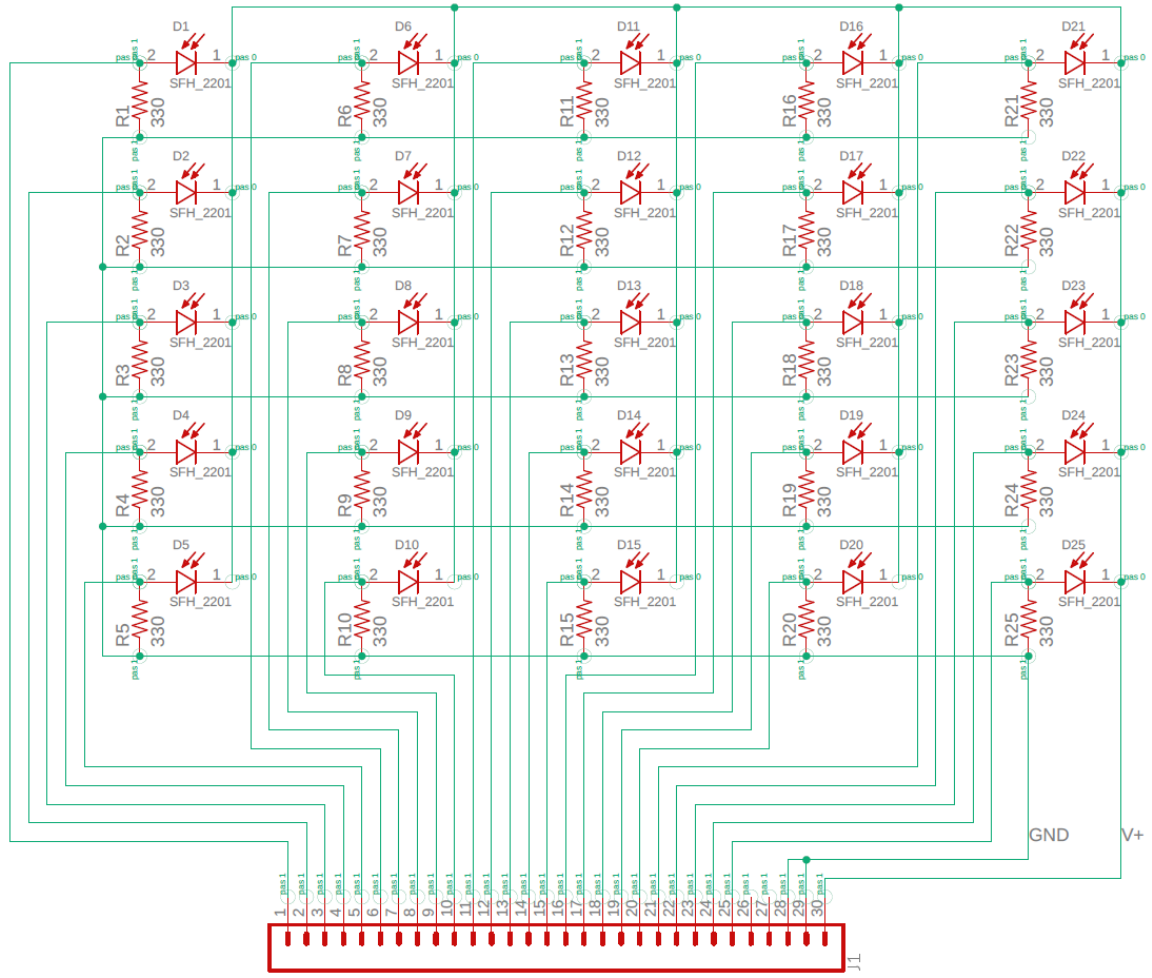

(a)

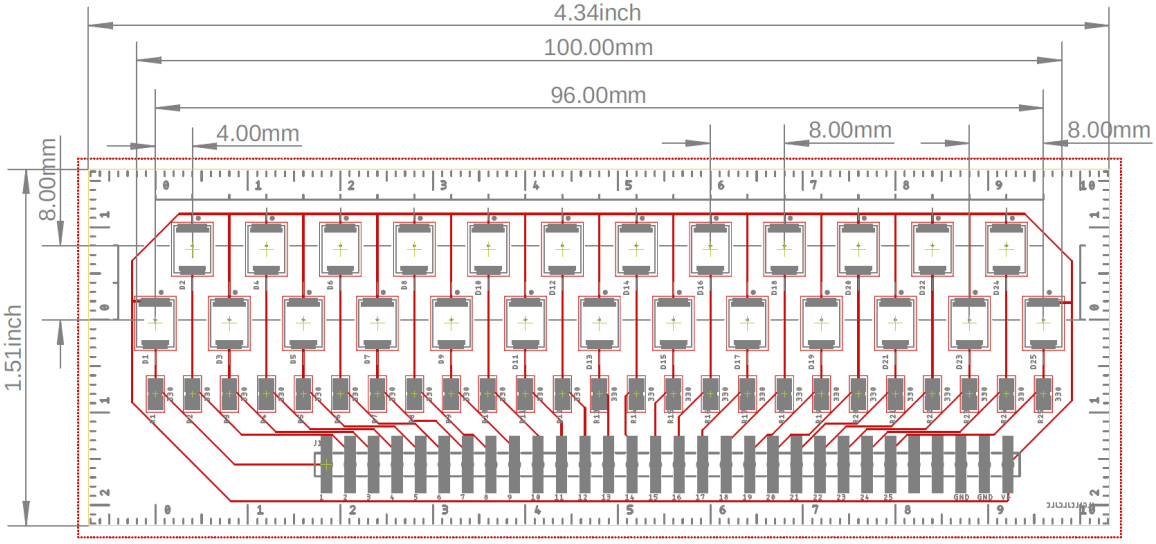

(b)

Figure 5.16: Spatial Array Design

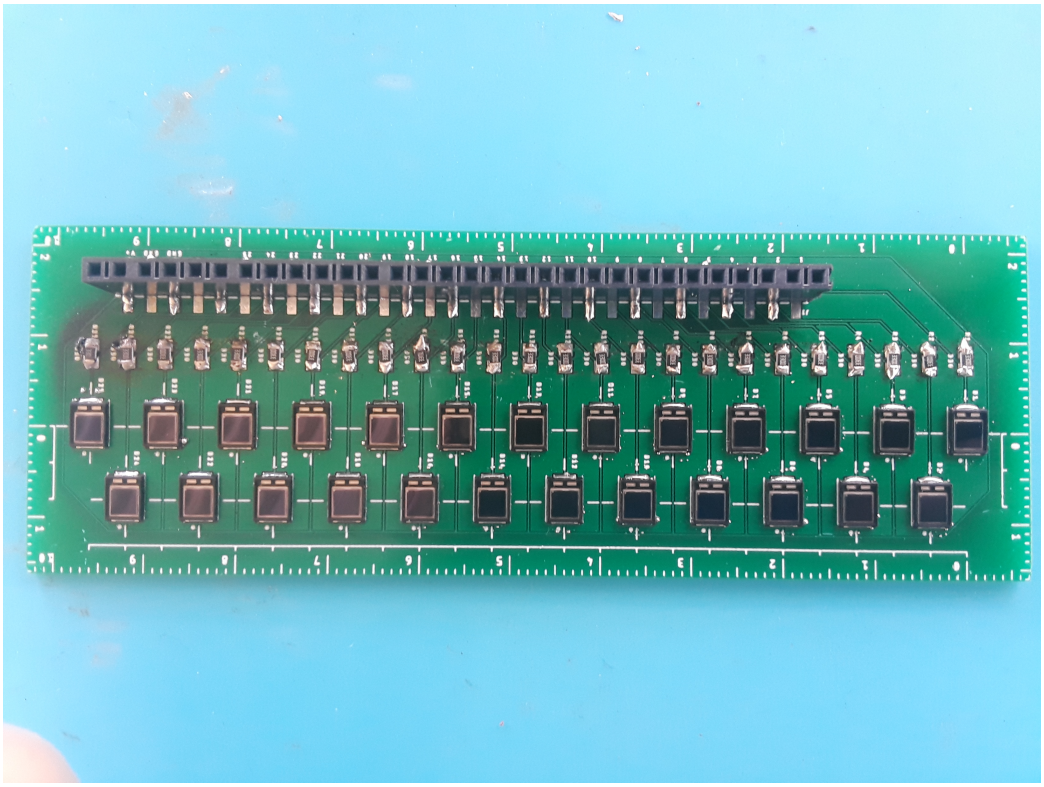

Figure 5.17: Assembled Spatial Array

instead, requiring the data from diodes in odd-numbered positions to be adjusted two positions ahead during data analysis. Each line places its photodiodes at the center of half the 25 test positions, and they are offset by one test position location. The separation between the two lines is two test position locations' worth. Printed markings were added to the board - one set to denote a millimeter ruler, and the other to mark the centers of the photodiode positions for alignment with a grid during testing.

The photodiodes were connected with reverse bias of 5 V to increase their response time [51]. Based on the expected irradiance, the photodiodes' surface area, and the spectral response curve given in [51], a predicted current range was estimated, and used to size resistors to convert this current into voltage for the DAQs. Amplification of the photodiodes' response was deemed not necessary. However, during later

analysis, a revised prediction of irradiance, due to correction of an error in the implementation of Eq. 5.2, was obtained, showing that the irradiance on the photodiode would be much less than the previous estimate. The corresponding photocurrent was thus significantly lower, and the previously determined resistance was far too low to produce voltage in the range required by the DAQ. A single extra resistor was added between the GND header and the jumper wire connecting to it, to increase the resistance seen by all the photodiodes.

For thermal control at the test plane, the most straightforward approach was to mount the entire simulator on a large metal base plate to serve as a heat sink. A wooden mounting plane for the LED nodes, power board, MCP2221A, and current-setting resistors was hand-cut - its dimensions are given in Figure 5.18. Threaded rods were used to create supports to allow height adjustment. The calculated 17.1 cm ideal height was measured and marked on the rods. The assembled structure can be seen in Figure 5.19

As an important risk reduction measure, a wooden irradiance shield was constructed to fit over the simulator during operation. Small gaps in the bottom on two sides allow all necessary wires to enter and exit, but the majority of the irradiance is contained inside. This allows operation of the simulator without requiring test personnel to wear gloves and long sleeves, unless they must manipulate equipment inside the shield or adjacent to the wire gaps. It also decreases the risk of injury, if an individual without eye protection inadvertently observes the simulator during operation. The operational simulator with the irradiance shield in place is shown in Figure 5.20.

In the future, the interior of this shield needs to have a low-reflectivity coating applied to minimize reflected irradiation. The suitability of a paint for this purpose depends on its spectral reflectance, emittance, and absorptance. Low values of reflectance and emittance would be necessary from 250-1000 nm due to the high energy concentrated

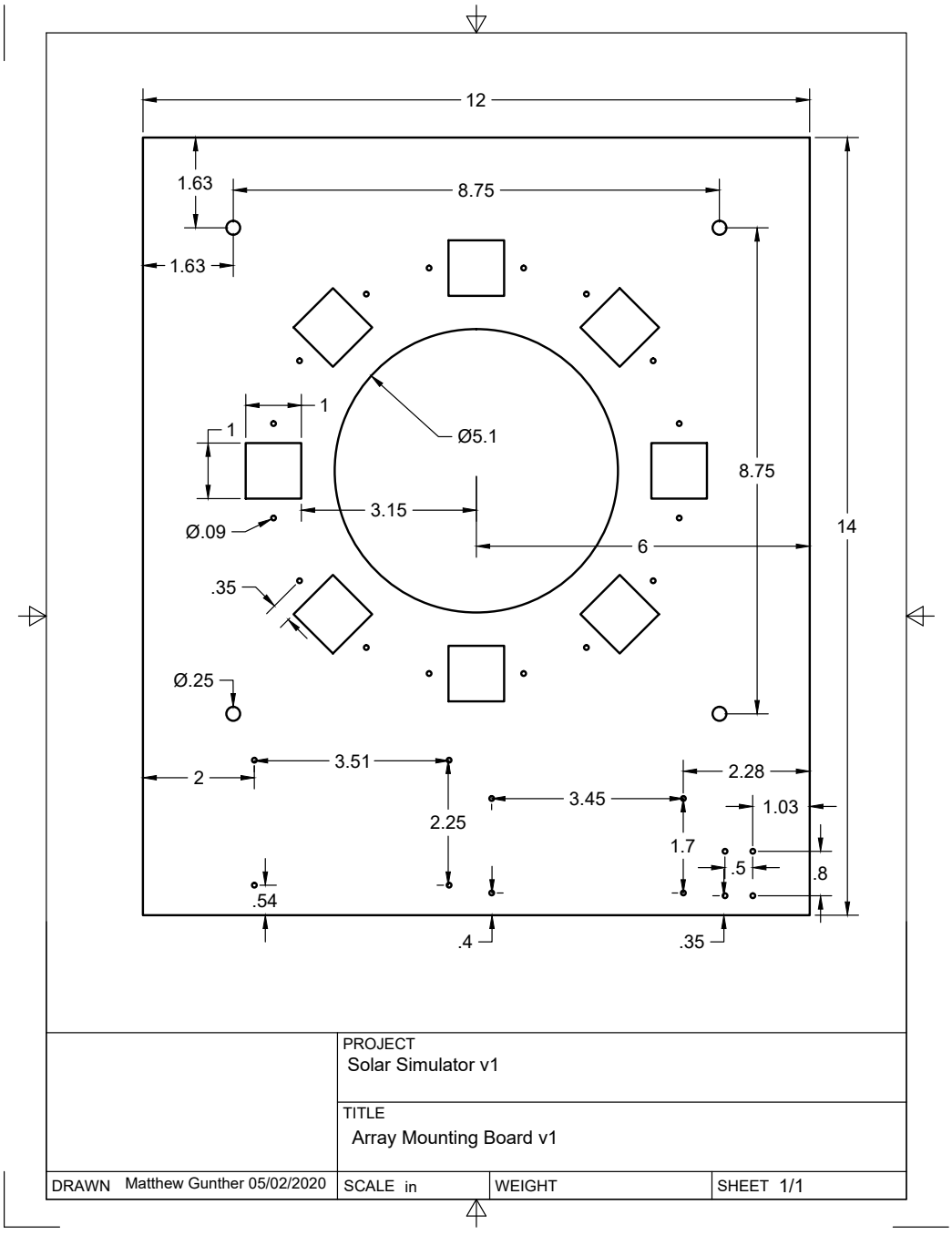

Figure 5.18: Dimensions of Array Mounting Board

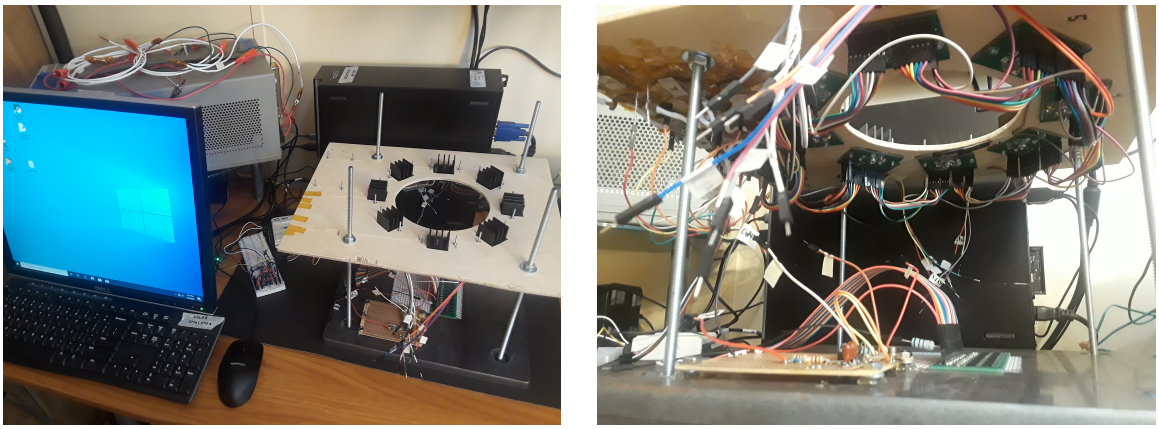

(a) (b)

Figure 5.19: Assembled Structure

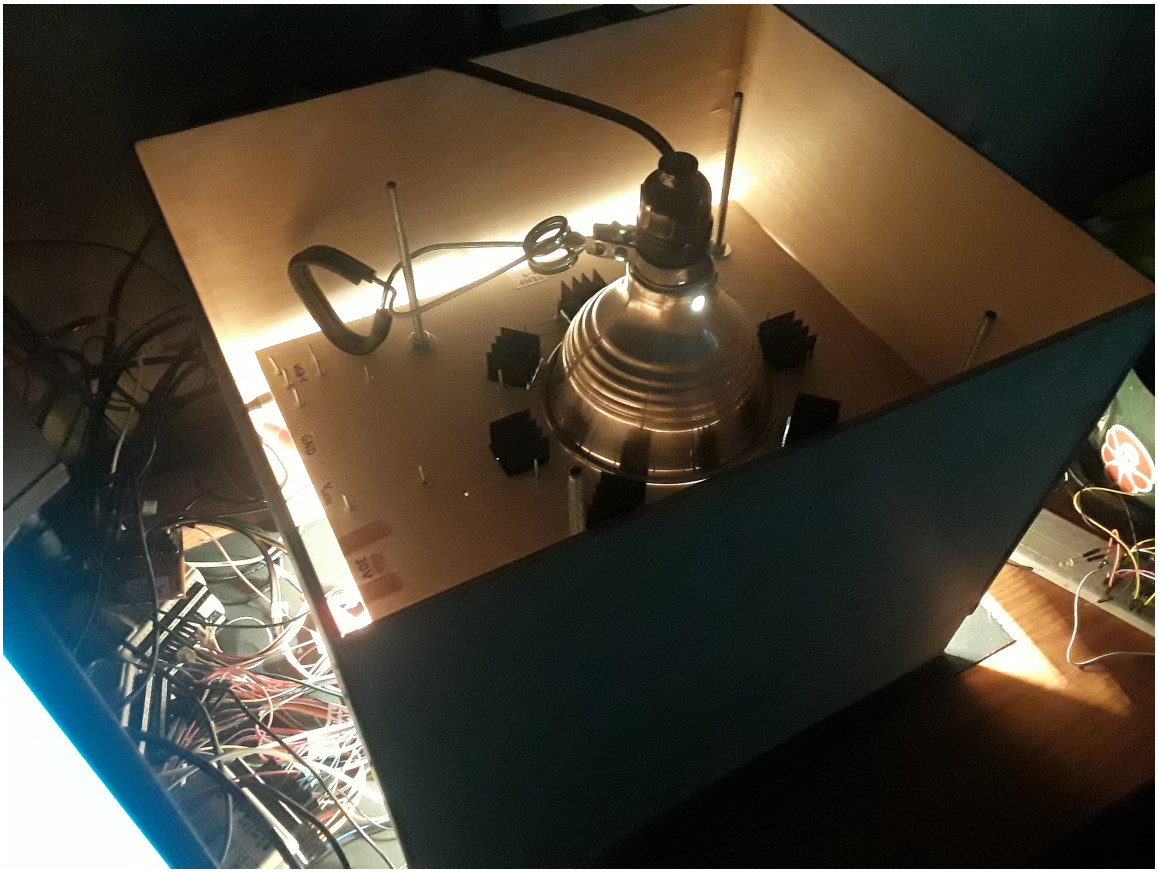

Figure 5.20: Simulator Operating, Including Irradiance Shield

in this wavelength range, but a higher emittance in the far UV and NIR ranges would be acceptable due to the low power of the simulator in these regions.

The total cost of the required purchases to assemble this simulator was just over $1000. Significant savings resulted from using existing surplus equipment and components, such as the DAQs and PC. Most components were found at reasonable prices. It is of note that the 280 nm UVC LEDs cost just under $300 by themselves, making them the single most expensive component. LEDs in this wavelength range are much more expensive than the others chosen. LEDs in the 300-350 nm range tend to be even more expensive; adding these to the simulator would have increased the total cost by about $400. Similarly, adding any LEDs above 1000 nm could easily have resulted in a price jump of over $500. LEDs of any wavelength between 380 and 940 nm however, are incredibly affordable, and adding many more wavelengths in this range (and more corresponding PWM frequencies) would be a robust way of increasing the potential spectral match of an improved version of this simulator design.

Chapter 6

TESTING AND RESULTS

6.1 Testing Methods and Apparatus

See Appendix D for the operational procedure used during all tests. For R_{SM} classification testing, a second photodiode was chosen ensure the 280 nm UVC LED would be picked up, since the SFH 2201's spectral response is not defined below 400 nm [51]. Linear extrapolation was used to infer the spectral response for the 385 nm UVA LED. A Marktech MT03-23 photodiode [41] was selected due to its enhanced UV sensitivity; its spectral response is given down to 250 nm. However, due to the much smaller active area of the photodiode, using a resistor as a current-to-voltage converter was not practical. An op-amp in an inverting transimpedance amplifier configuration was implemented to ensure a voltage signal within the DAQ input range. This circuitry was constructed on a spare through-hole prototyping board from the environments lab; the diagram and assembled board are shown in Figure 6.1

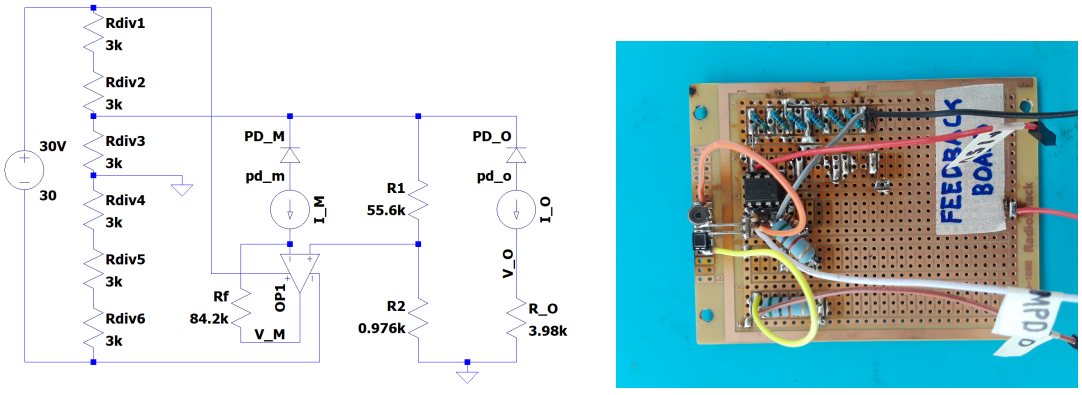

(a) (b)

Figure 6.1: Photodiodes on Feedback Board

The feedback board was mounted on the metal base plate of the simulator next to the test plane such that the photodiodes were located directly below one of the LED nodes, shown in Figure 6.2. Both photodiodes were also chosen for having fast response times, $<2\mu$s, under 1% of the minimum pulse duration of 200 μs at 15% duty cycle for the 940 nm IR LED at 755 Hz.

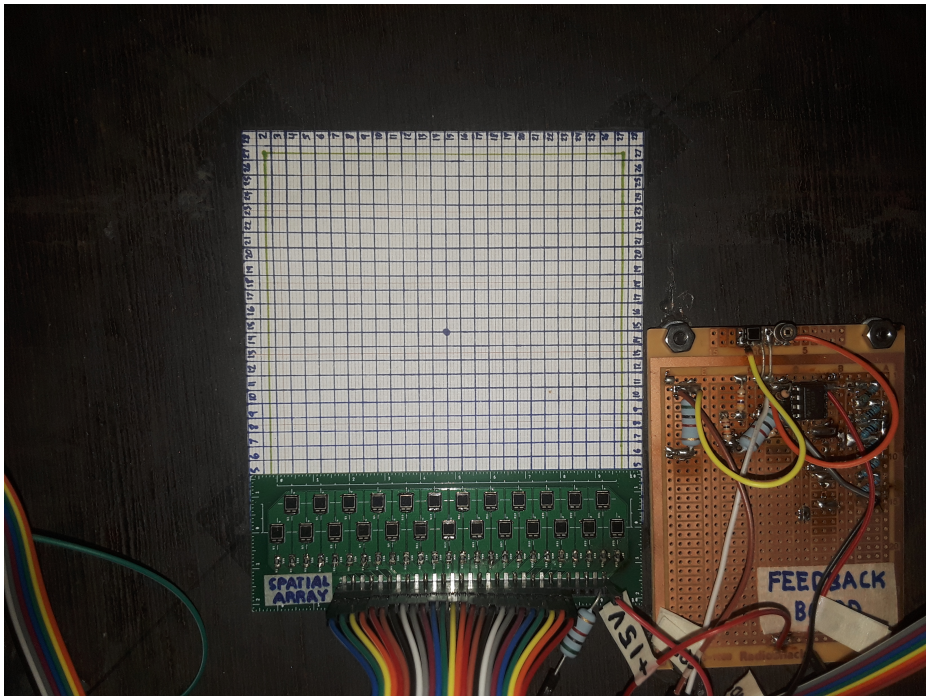

Figure 6.2: Location of Feedback Board Relative to Test Plane

Spectral analysis data was acquired by averaging the last 1000 samples (0.1 s) of data for non-FFT calculations, and the last 10,000 samples (1 s) of data for calculation of FFT coefficients. These numbers were recorded one per second, so the non-FFT parameters reflect a new set of 1000 data points while the FFT coefficients reflect a first in, first out set of 10 chunks of 1000 data points each. The voltage coefficients V_k calculated from the last column of Table 5.6 were used to calculate the average voltage at each wavelength using

$$V_{ave} = V_k D_k \tag{6.1}$$

from the definition of a duty cycle. Data was acquired during a final check of the control law; the first two minutes of collection was designated the warm-up period. It was discovered during testing that the SFH 2201 diode responded well after all to the 280 nm UVC LED, so the SFH 2201 was used as the primary source for the control law and the spectral match data due to the simplicity of using Ohm's Law. V_{ave} was used to calculate the corresponding photogenerated current using the 3.98 kΩ resistance, which was then used to calculate the incident power using the spectral response curve. Incident irradiance was computed from this power using the photodiode active area, and used as the integral of spectral irradiance for the relevant wavelength bin in Equations 3.1 and 3.7.

For S_{NE} classification testing, the spatial array board was tested at each of 27 locations across the test plane, corresponding to the 25x25 spatial matrix plus a margin of 2 to account for the staggered spatial array photodiodes. A grid was drawn using mm graph paper showing the center points of the spatial matrix test positions, and used with the markings on the spatial array board to align it during the testing. This grid, shown in Figure 6.3 had a total of 27x27 test positions of 4 mm square side length, since the two rows of the spatial array board add an extra two required testing locations to cover the central 25x25 grid.

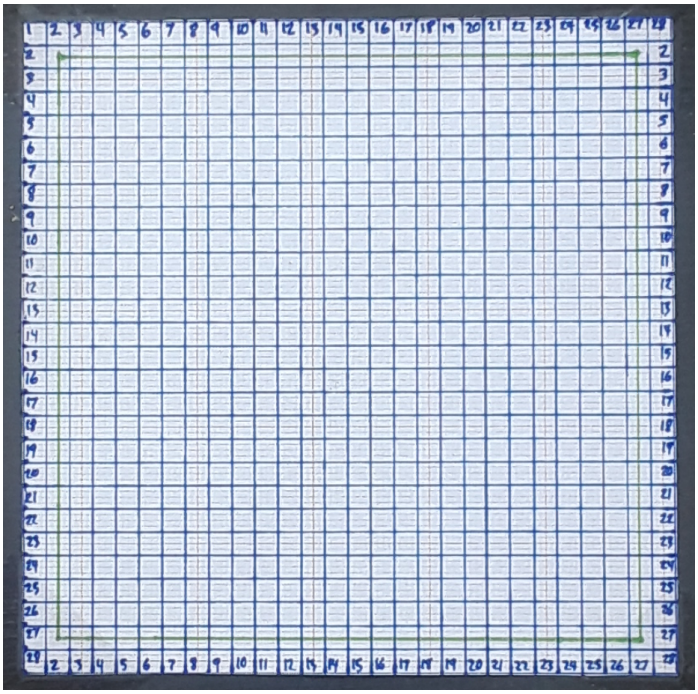

Figure 6.3: Spatial Matrix (Test Plane Outlined in Green)

The simulator was run continuously, replacing the irradiance shield during each data collection run at a test location. Data was collected for 30 s at each position, after allowing one to two minutes for the control law to restabilize the irradiance after replacing the shield. Data from the feedback board photodiodes was collected continuously during the entire procedure. The voltage data from the spatial array photodiodes was averaged directly, and converted to irradiance in the same manner as for the spectral match calculation. Equations 3.2 and 3.4 were then used to evaluate S_{NE}, with the photodiodes on the feedback board serving as the required monitor cells [6][7]. The data contains sufficient information to calculate the spatial uniformity of each wavelength individually, but this is not required for classification under either ASTM E491 or E927 [6][7].

For T_{IE} classification, the data from the spectral match test was reused. The time-series values of the total irradiance formed the data set used with Equations 3.3 and

3.6. If more data is required in the future, the spatial array tests can be used as a source of 27 additional temporal variance tests.

In order to verify that the simulator can be used for its intended purpose of solar cell I-V curve testing, a set of five solar cells was prepared, shown below in Figure 6.4 along with an image of a cell under the simulator. A second DC load, an Agilent 6063B, was used to control the current through the cell, while recording the corresponding voltage values using a Fluke 17B Digital Multimeter. The current was increased in steps of 0.01 A (the minimum resolution of the load) from 0.01 A until it reached its maximum, I_{sc}, and could no longer be increased. This was usually between 0.4 and 0.5 A for these cells.

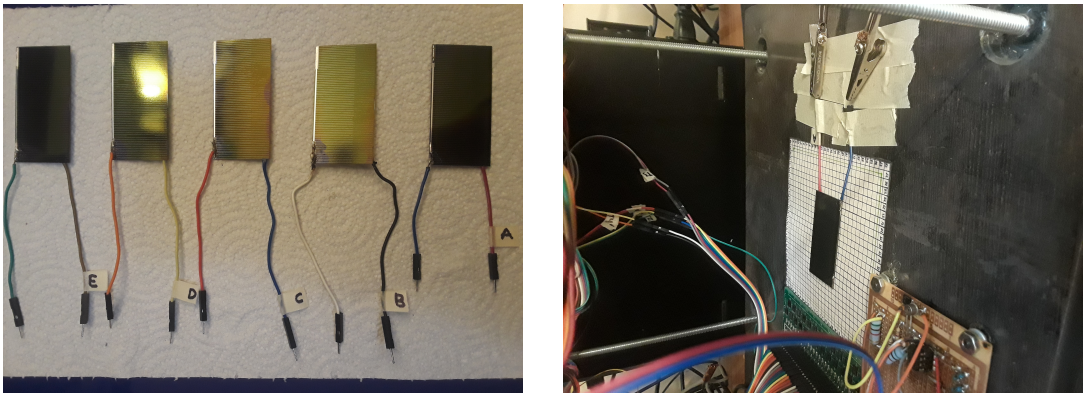

(a) (b)

Figure 6.4: Solar Cells Tested

6.2 Total Irradiance Calibration

In order to accurately calculate the irradiance using data acquired from the photodiodes, some sort of calibration step must be performed. ASTM E491 and E927 reference various standards for such calibration procedures [6][7], such as ASTM E1125-16 [4]. All of them hinge on using a light source of known spectral irradiance, usually with the addition of a previously calibrated reference photodiode. Short of purchas-

ing such a light source, the only other option is to use terrestrial sunlight. E1125 in particular outlines a method for calibrating photovoltaic cells in sunlight using a standardized spectrum such as ASTM E490 [4][5]. E1125 also provides a recommended collimating test fixture, shown in Figure 6.5.

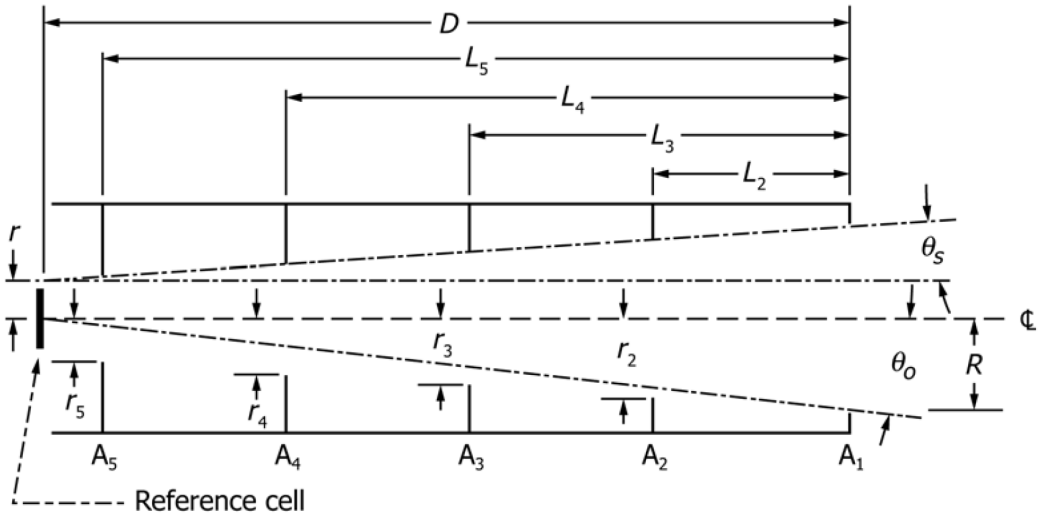

Figure 6.5: ASTM E1125-16 Recommended Collimator Design [4]

A collimator following this design was constructed for an aperture radius r of 5 cm, in order to fit the entire 10 cm wide spatial array. A field of view $FOV = 10° = 2\theta_O$ and slope angle $\theta_S = 2°$ was chosen to imitate common pyrheliometer geometry, as recommended in the standard [4]. The collimator is shown set up in sunlight in Figure 6.6.

(a) (b) (c)

Figure 6.6: Collimator for Photodiode Calibration and Solar Cell I-V Testing

The collimator was used to take steady-state readings from the photodiodes on the spatial array board and the feedback board, using the same software used to run the simulator but with the control loop disabled. Additionally, the solar cells were tested using the same I-V procedure as under the simulator, again in triplicate for each cell. These results are compared to the simulator data in Section 6.3.

In order to calculate an accurate terrestrial solar spectrum, the SMARTS2 software model was used [20]. This is the software model used to produce ASTM Standard G173-03 [8], which uses it to calculate the terrestrial solar spectrum (AM1.5) from the extraterrestrial ASTM E490 (AM0) spectrum and various atmospheric inputs. During the various sunlight tests, local atmospheric and weather conditions were recorded. The AM0 extraterrestrial spectrum was adjusted by a scaling factor based on total irradiance data obtained from the LISIRD database mainainted by LASP at CU Boulder [30]. Atmospheric carbon dioxide concentration was obtained from NOAA's Global Monitoring Laboratory website [48]. The inputs to the SMARTS2 program used for this work are shown in Appendix C.

The spectral irradiance output by SMARTS2 was used in conjunction with the photodiodes' spectral response curves to calculate a correction factor, X: the total measured

current divided by the total expected current. The definition and use of this factor is given in E491 as [6]:

$$X_\lambda = \frac{E_{\lambda,sun,measured}}{E_{\lambda,sun,standard}} \tag{6.2}$$

$$E_{\lambda,sim,calibrated} = \frac{E_{\lambda,sim,measured}}{X_\lambda} \tag{6.3}$$

As used in this work, however, X has no spectral variation, since no spectral information could be measured from the solar irradiation with the available equipment. The correction factor was used to adjust the total irradiance calculations in the simulator testing data. The calibration data and calculated correction factor is shown in Table 6.1.

Table 6.1: Photodiode Correction Factor From Sunlight Calibration

Predicted photocurrent [A]	**Measured photocurrent [A]**
2.647e-3±0.027e-3	1.030e-3±0.001e-3
Calibration function, X [ratio]	0.389±0.004

6.3 Results and Discussion

6.3.1 Spectral Match

The voltage data used to calculate the spectral match is shown in Figure 6.7. The calculated spectrum used to compute R_{SM} is shown in Figure 6.8. The computed R_{SM} values are shown in Table 6.2. The calculated spectral match falls far below the expected benchmark. However, this is mostly due to the error in total irradiance. Due to a combination of poor coastal weather conditions and high smoke plumes during the fall quarter months, the sunlight calibration process was delayed until after the spectral test data was taken. As a result, a temporary value of 0.2 was assigned to

the calibration factor X to determine the voltage set point. If the actual value of 0.39 had been used instead, the total irradiance would instead have been about twice its measured value, which is much closer to the actual solar constant of $S0 = 1366.1\ [\frac{W}{m^2}]$ [5], which was discussed previously in Section 2.2. This impacted the spectral match because the IR lamp irradiance is constant, while that of the LEDs is adjustable. Thus, at an anomalously low LED irradiance, the IR lamp irradiance is too high in comparison. This accounts for the large increase seen in R_{SM} at long wavelengths.

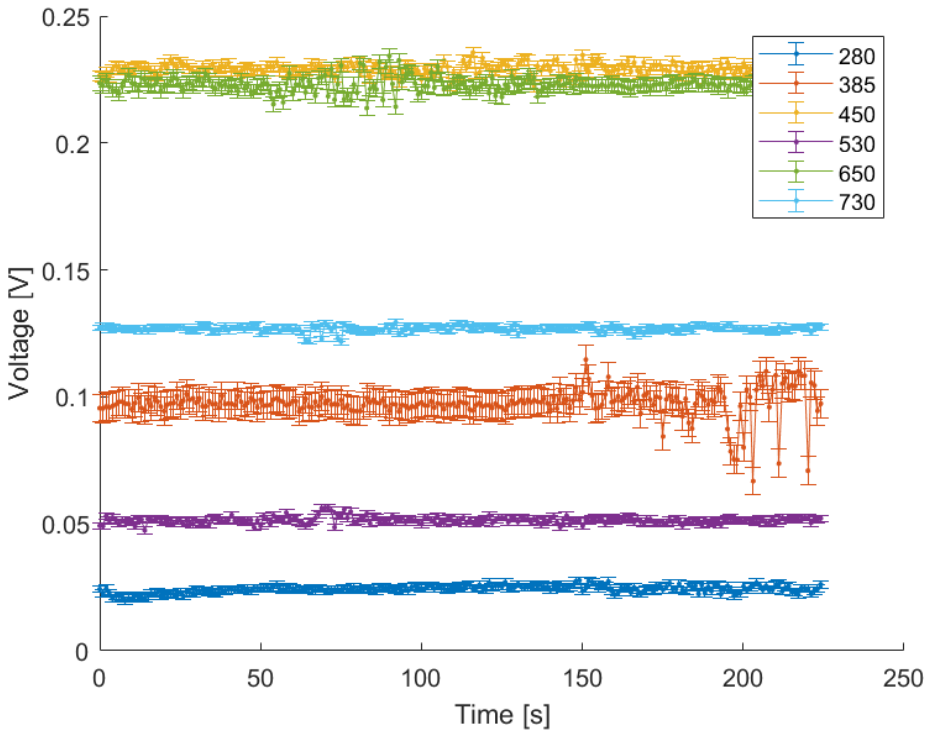

(a)

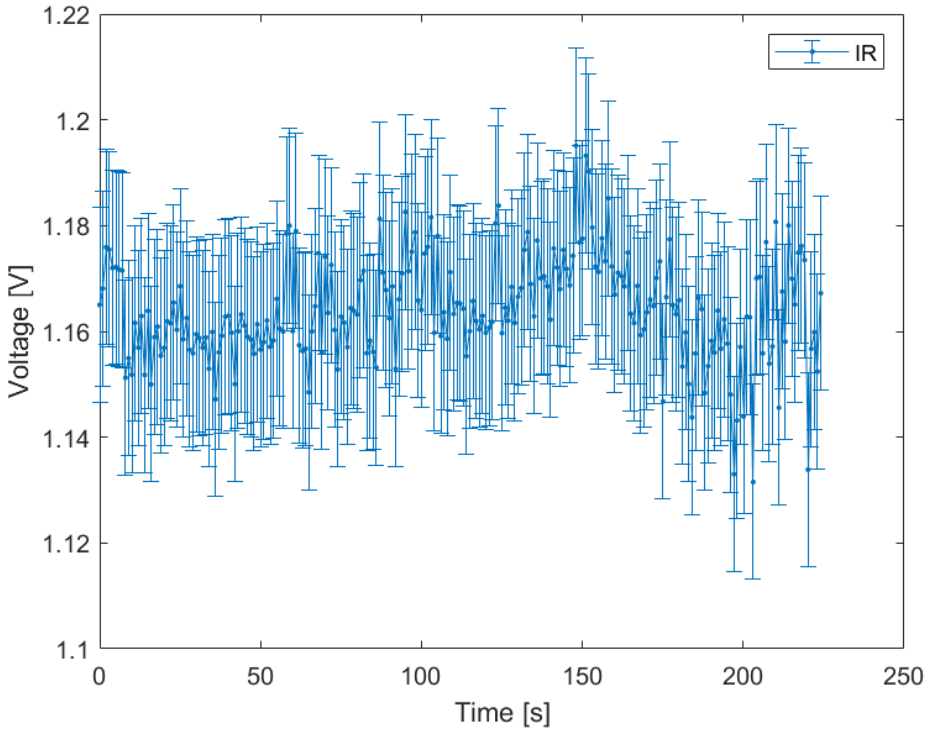

(b)

Figure 6.7: Data for R_{SM} and T_{IE} Calculations: (a) Voltage From LEDs, (b) Voltage From IR Lamp

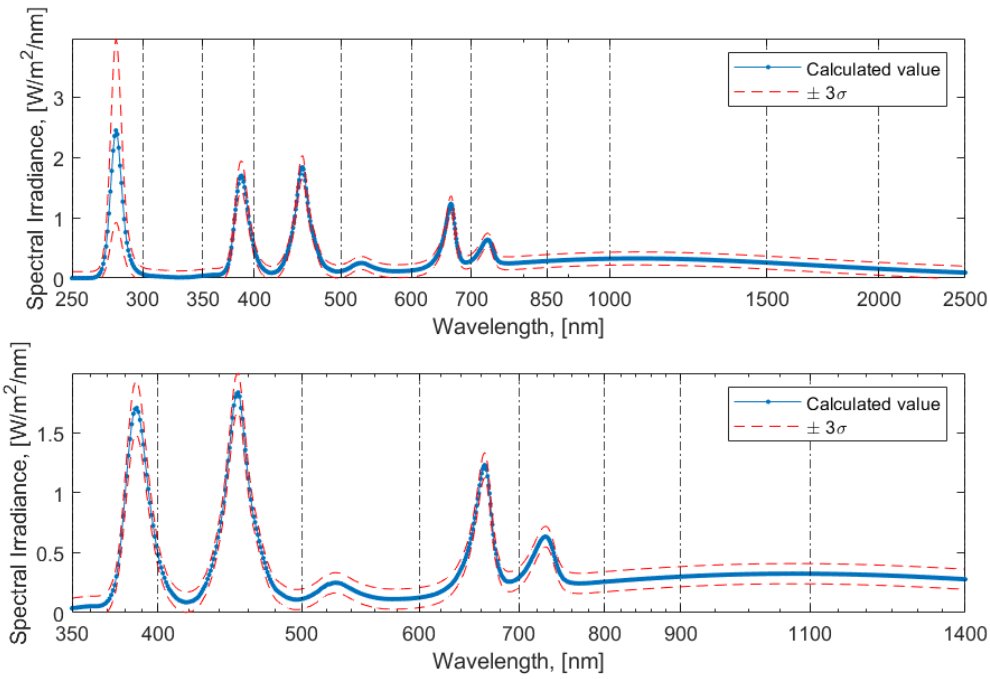

Figure 6.8: E_λ Calculated From Data Shown in Figure 6.7: (top) E491 Bins, (bottom) E927 Bins

Table 6.2: R_{SM} of Spectrum Shown in Figure 6.8

E491 Bin (nm)	R_{SM} (and 3σ CI), Eq. 3.7	R_{SM} (and 3σ CI), Eq. 3.1	**E927 Bin (nm)**	R_{SM} (and 3σ CI), Eq. 3.1
250-300	2.158±0.110 (1.828, 2.488)	4.946±0.253 (4.187, 5.706)	N/A	N/A
300-350	0.031±0.007 (0.011, 0.050)	0.071±0.015 (0.026, 0.115)	N/A	N/A
350-400	0.558±0.007 (0.538, 0.579)	1.280±0.017 (1.230, 1.329)	350-400	1.717±0.019 (1.661, 1.774)
400-500	0.272±0.002 (0.265, 0.278)	0.623±0.006 (0.606, 0.640)	400-500	0.831±0.006 (0.813, 0.850)
500-600	0.085±0.002 (0.080, 0.091)	0.196±0.005 (0.182, 0.209)	500-600	0.261±0.005 (0.247, 0.275)
600-700	0.274±0.002 (0.267, 0.281)	0.629±0.006 (0.611, 0.647)	600-700	0.839±0.006 (0.820, 0.857)
700-850	0.274±0.002 (0.267, 0.281)	0.628±0.006 (0.610, 0.647)	700-800	0.867±0.007 (0.845, 0.889)
850-1000	0.351±0.003 (0.341, 0.361)	0.804±0.008 (0.778, 0.829)	800-900	0.847±0.009 (0.820, 0.873)
1000-1500	0.638±0.003 (0.628, 0.648)	1.462±0.010 (1.432, 1.491)	900-1100	1.304±0.009 (1.277, 1.332)
1500-2000	1.045±0.008 (1.021, 1.070)	2.396±0.022 (2.332, 2.461)	1100-1400	2.027±0.013 (1.990, 2.065)
2000-2500	1.536±0.021 (1.474, 1.598)	3.521±0.049 (3.373, 3.667)	N/A	N/A
Total Irradiance	575.2±2.4 $[\frac{W}{m^2}]$		N/A	359.2±1.1 $[\frac{W}{m^2}]$
# Qualifying	4 of 11	6 of 11	N/A	6 of 8
Result	**Class C**	**Class C**	N/A	**Class U**

The total irradiance mismatch also had a much larger impact on the E491 calculation of R_{SM} than on the E927 calculation, due to the difference in definitions. The E491 equation, 3.7, is defined by the ratio of irradiance to an accepted standard, while the E927 equation, 3.1, is first normalized by the total irradiance [6][7]. When using the E927 formulation over the E491 bins, a much better spectral match is calculated, as shown in column three of Table 6.2.

The other unexpected result of the spectral analysis is the underperformance of the 530 nm Green LEDs. Though expected to be the least efficient compared to the other wavelengths, the calculated irradiance was far below the expected, as can be seen by the very small spectral peak at 530 nm in Figure 6.8. This could be the result of a shift in the frequency of the PCA9685 operating the string, an error in the predicted voltage, unusually low sensitivity of the photodiode, lower than expected radiant efficiency of the LEDs themselves, or faulty wiring causing anomalously high resistance and thus low current.

Expected deficiencies in the spectral match are present as well. The 940 nm IR LEDs, which were not functioning due to the damaged PCA9685, can be seen missing from the appropriate bin in 6.8. This error was offset by the relative increase in IR lamp irradiance, as mentioned above. The 300-350 nm bin is empty by design, as reflected in the E491 spectral match results. The 280 nm UVC LED was received unexpectedly well by the SFH 2201 photodiode, exceeding the predicted spectral response in that wavelength range. The poor match in its wavelength bin is likely due mostly to this difficulty in predicting the spectral response curve accurately in the UV region. Without more accurate spectral response data, it cannot be concluded whether the 280 nm UVC LED is too bright, the photodiode is too sensitive, or a combination of the two.

The overall spectral classification of the simulated spectrum is Class C and U (catch-all categories for any spectrum not meeting the minimum requirements [6][7]), the lowest of both ASTM E491 and E927. Adjusting the voltage set point to reflect the actual calculated X value and taking new spectral readings would most significantly improve the calculated match. An iterative process could also be easily undertaken to increase the specific set point of the 530 nm Green LED and decrease that of the 280 nm UVC LED, which would also have a significant positive effect on the overall spectral match. Implementing these two steps is highly recommended as the next piece of future work on the simulator.

6.3.2 Spatial Non-Uniformity

Spatial non-uniformity calculations are shown in Table 6.3. A visualization of the data is given in Figure 6.9. The calculated S_{NE} was worse than expected, but still sufficient to place the simulator in the Class C ($S_{NE} < 10\%$) category for standard E927 [7]. The Class C rating for E491 is again a catch-all category, for any $S_{NE} > 5\%$. As can be seen in Figure 6.9, there is only a slight trend in the data for irradiance to be highest in the middle and lowest in the corners - in fact, the trend does not appear in the y-direction, only the x-direction. This is the direction that the spatial array board was moved across the test plane in. Oddly, the far left and right edges are brighter than the two apparent dark bands at about one-third and two-thirds of the x dimension.

Table 6.3: Calculated Spatial Non-Uniformity

Standard	S_{NE} [%]	**3σ CI**	**Classification**
E927	8.16±0.60	(6.37, 9.96)	**Class C**
E491	7.95±0.59	(6.18, 9.71)	**Class C**

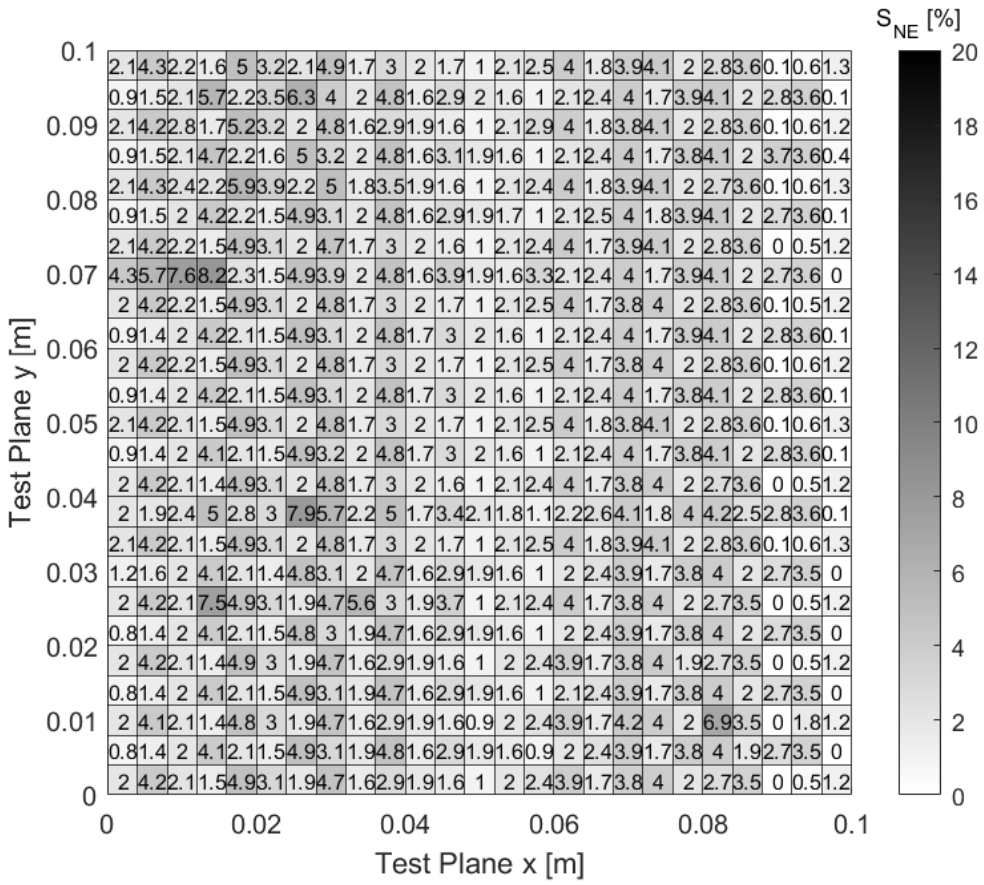

Figure 6.9: S_{NE} **Evaluated Across Spatial Matrix**

Additionally, it is of note that the maximum spatial non-uniformity values appear to be randomly spread, instead of clustered around the expected dark corner regions. While conducting the spatial testing, the jumper wires connecting the spatial array photodiodes to the DAQs had to be retightened periodically. Loose wiring could be to blame for the occurrence of non-uniformity maximums in the observed locations. By averaging repeats of the spatial testing procedure in the future, most of the random noise would be smoothed out over the test plane, particularly if the spatial array was moved right to left and top to bottom instead of only left to right. Regardless, the current value of spatial non-uniformly is acceptable for solar cell testing.

6.3.3 Temporal Instability

Temporal instability results are shown below in Table 6.4. More percent variance was present in these values than was in either S_{NE} or RSM. The 95% confidence intervals in Table 6.4 span from Class A to Class C under both standards E927 and E491 [6][7]. It may be possible to decrease the uncertainty in these measurements in the future by redoing the test with a much longer duration of measurement. If the future work mentioned above to improve the spectral match is undertaken, it would be a simple matter to use the new data to improve the temporal instability calculation. Assuming a normal distribution, there is a 99.86% cumulative probability (satisfying $p < 0.05$) that the temporal instability T_{IE} is $< 5\%$ using the E927 criteria, placing it in Class B. The cumulative probability for $T_{IE} < 3\%$, qualifying for Class B under E491, is 60.17%.

Table 6.4: T_{IE} of Data Shown in Figure 6.7

Standard	T_{IE} [%]	**3σ CI** [%]	**Classification**
E927	2.822±0.730	(0.633, 5.012)	**Class B**
E491	2.812±0.729	(0.627, 4.998)	**Class B or C**

6.3.4 Solar Cell I-V Curves

I-V curve data from the solar cells under sunlight and the simulator are compared in Figure 6.10. As a practical test of the simulator's use in solar cell testing within the space environments lab, the acquired curves indicate strong potential. There is slightly less noise in the IV curves under the simulator than under sunlight. The obvious decrease in short-circuit current under the simulator is primarily due to the mismatch in the total irradiance discussed previously. When illuminated by lower irradiance, open-circuit voltage decreases very slightly while short-circuit current drops dramatically in comparison. This is consistent with the data in Figure 6.10. Note

that the sunlight IV curves represent two different days, with significantly different outdoor temperatures. As a result, there are two clusters in that data set. The higher-temperature readings (A1 and B1) show the typical increase in open-circuit voltage and decrease in short-circuit current consistent with an increase in temperature.

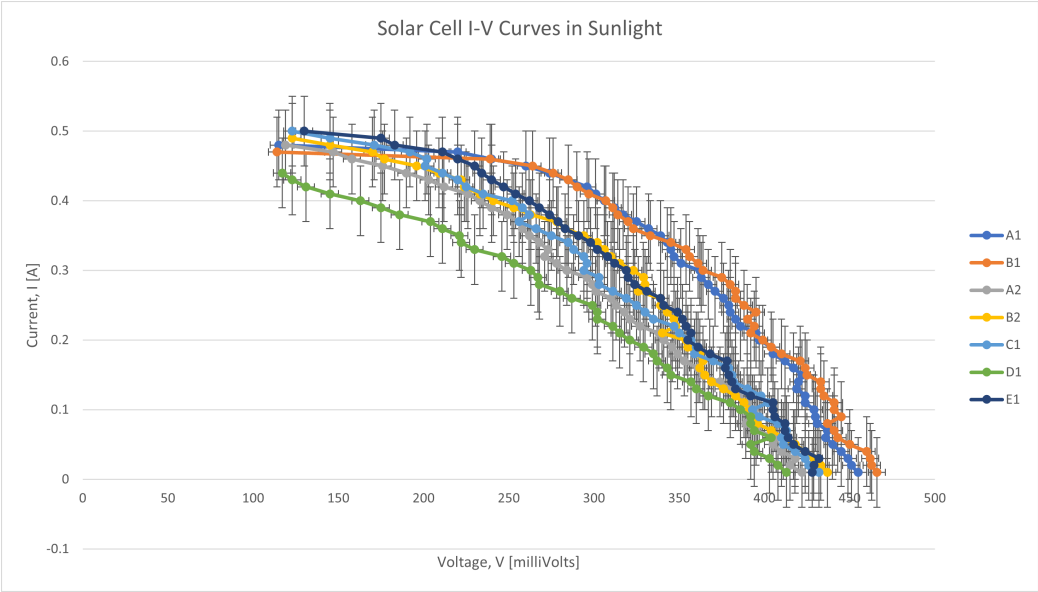

(a)

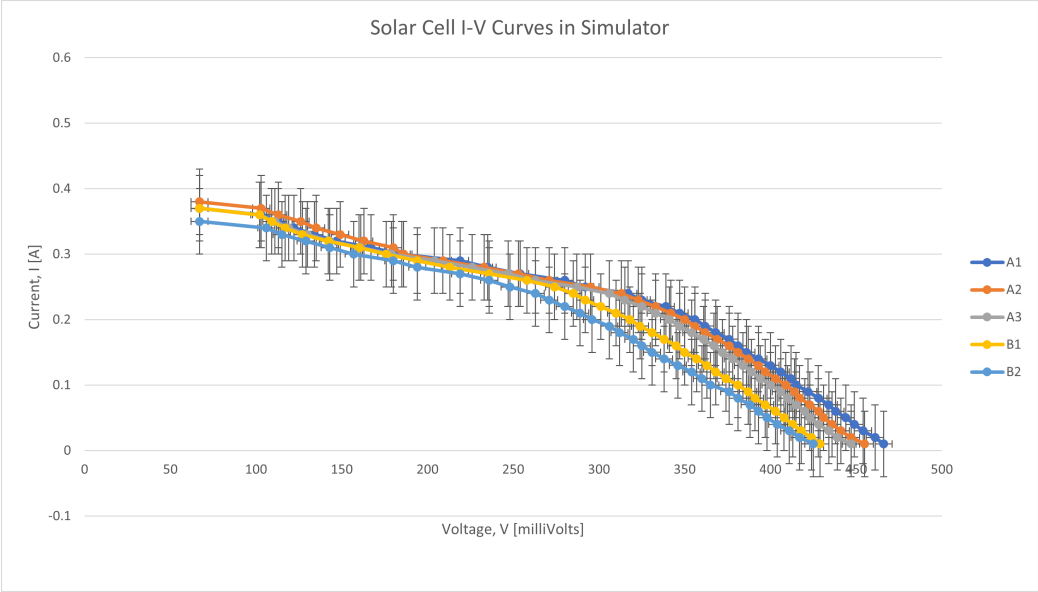

(b)

Figure 6.10: Solar Cell I-V Curves: (a) Sunlight, (b) Solar Simulator

An important detail not reflected in the obtained data is that, when testing the cells under the simulator, there was unexpected difficulty in resolving the current reading at low voltages. The current reading of the power supply used to control the IV sweep was very stable at higher voltages, but at these lower voltages, fluctuated rapidly and widely. This likely reflects the supply having a fast enough response time to attempt to compensate for the individual pulses of the LEDs, but not having a fast enough sampling rate to obtain consistent or accurate measurements of the waveform. If the resulting instability becomes an issue in incorporating the simulator into the space environments classes, it would be necessary to adjust the lab procedure slightly. The least intensive modification would be to add a simple low-pass filter to the setup, with a cutoff frequency of of around 100-300 Hz, which would block the LED modulation frequencies of Table 5.5 from being observed by the power supply. This could likely be accomplished with spare components currently available in the lab, and is highly recommended. An RC circuit might cause a voltage drop due to the series resistor, while an RL circuit might interfere with voltage measurements near open-circuit voltage due to the parallel resistor. However, an LC circuit, which consists of a series inductor and a parallel capacitor, would present neither of these problems. The relation between inductance, capacitance, and the cutoff frequency is given in [52] as:

$$f_c = \frac{1}{2\pi\sqrt{LC}} \tag{6.4}$$

Chapter 7

CONCLUSIONS AND FUTURE WORK

A summary of the classifications presented in Section 6.3 is given in Table 7.1. Overall, the simulator currently qualifies as Class UCB under ASTM E927. However, the spectral match category of U actually means that the simulator fails to qualify as Class C for R_{SM}, providing no lower limit on how bad the match can be in this category [7]. The stricter minimum requirements of ASTM E491 mean that its Class CCC category under this standard is also merely a statement that it failed to meet the minimum requirements, not providing any bound on the lower limit of its performance in all three categories.

Table 7.1: Overall Classification

Standard	**Spectral Match**	**Spatial Non-Uniformity**	**Temporal Instability**
E927	U	C	B
E491	C	C	C

The issues with the spectral match discussed in 6.3.1 point to a few simple changes that should improve the simulator to a Class C under ASTM E927, qualifying it as a Class CCB simulator for solar cell testing. The desktop structure and LabView control have proven reliable, and enable compact storage of the equipment when not in use. Operation of the simulator is straightforward after familiarizing oneself with the layout of the LabView interface and the main power supply. The complexity of the wiring necessitates careful setup, but the only components that must be physically manipulated during a testing procedure are the irradiance shield and IR lamp. Overall, the simulator in its current state requires only minor adjustment before it can be incorporated into space environments laboratory coursework.

7.1 Future Work

Various suggestions were made throughout for future improvements or additions to the simulator. To reiterate, these are, in order of importance:

- Change the assumed total irradiance calibration factor of $X = 0.2$ to its experimental value of $X = 0.39$ within the LabView control software, and obtain new data to update the R_{SM} and T_{IE} calculations with. This will markedly improve both the spectral match and the quality of solar cell I-V curve testing.

- Construct an LC low-pass filter to connect between tested solar cells and the power supply used to conduct their I-V sweeps. This will make the current values much easier to read when near I_{SC} conditions.

- Replace the damaged PCA9685 in position PWM7 on the power distribution board with the spare chip currently mounted on a breakout board. Operation of the 940 nm IR LED string would then be possible.

- Repeat the spatial testing, moving the spatial array right to left and top to bottom instead of the right to left scheme used here, then average all results to update the S_{NE} calculation. This should eliminate some of the non-random error caused by variations between the array photodiodes.

- Change the LabView control to include calculation of the voltage set point based on an input total irradiance. This would enable a simple means of adjusting the simulator output to match the conditions of other solar orbital distances, such as those of Mars or Venus.

- Paint the interior of the irradiance shield with a dark, high-absorptance, low-reflectance coating. The amount of reflected irradiance on the test plane would be greatly reduced.

- Create a new structure to attach the array mounting board in front of a vacuum chamber porthole, allowing projection of the irradiance into the chamber. This would be simplest for the Thing 1 and 2 chambers - setting the simulator on top projecting downwards is extremely similar to its current setup. Testing solar cells under vacuum conditions would then be a possibility.

- Add another set of eight 530 nm Green LEDs to the blank spaces on the LED node PCBs. Some adjustments would be necessary to the power wiring to split the current line in two, adding a second current-setting resistor for the new line. The spectral match would be improved, and various benefits would result from the decrease in required duty cycle of the green LEDs during operation.

- Add surface-mount optics to the LEDs. This may be possible using the existing LED node PCBs, depending on the size of the optics chosen. The height of the array mounting board would likely have to be adjusted, but the spatial uniformity would be improved.

- Add more LED wavelengths to improve the spectral match. A good place to start would be choosing wavelengths from the bins of the ASTM E491 Class A spectrum requirements. This would be an extensive undertaking requiring redesign of the LED node PCBs, but the spectrum would be significantly improved.

BIBLIOGRAPHY

[1] Cal Poly Github. http://www.github.com/CalPoly.

[2] Adafruit. CircuitPython. https://github.com/adafruit/circuitpython, 2020.

[3] Agilent Technologies. *Operating Manual - Agilent 603xA Family Autoranging System DC Power Supplies, Update 2*, September 2004. http://ridl.cfd.rit.edu/products/manuals/agilent/power%20supplies/cd1/model/603xoper.pdf.

[4] ASTM E1125-16. Standard Test Method for Calibration of Primary Non-Concentrator Terrestrial Photovoltaic Reference Cells Using a Tabular Spectrum. Standard, ASTM International, West Conshohocken, PA, 2016. http://www.astm.org/cgi-bin/resolver.cgi?E1125-16.

[5] ASTM E490-00a. Standard Solar Constant and Zero Air Mass Solar Spectral Irradiance Tables. Standard, ASTM International, West Conshohocken, PA, 2019.

[6] ASTM E491-73. Standard Practice for Solar Simulation for Thermal Balance Testing of Spacecraft. Standard, ASTM International, West Conshohocken, PA, 2015.

[7] ASTM E927-19. Standard Classification for Solar Simulators for Electrical Performance Testing of Photovoltaic Devices. Standard, ASTM International, West Conshohocken, PA, 2019.

[8] ASTM G173-03. Standard Tables for Reference Solar Spectral Irradiances: Direct Normal and Hemispherical on 37° Tilted Surface. Standard, ASTM

International, West Conshohocken, PA, 2020. http://www.astm.org/cgi-bin/resolver.cgi?G173-03(2020).

[9] A. Bazzi, Z. Klein, M. Sweeney, K. Kroeger, P. Shenoy, and P. Krein. Solid-state solar simulator. *Industry Applications, IEEE Transactions on*, 48:1195–1202, 07 2012.

[10] M. Bliss, T. R. Betts, and R. Gottschalg. Advantages in using leds as the main light source in solar simulators for measuring pv device characteristics. In *Optics + Photonics for Sustainable Energy*, 2008.

[11] Bureau International des Poids et Mesures. *Convocation of the General Conference on Weights and Measures (26th meeting)*, Versailles, France, 2018. Bureau International des Poids et Mesures.

[12] M. Cerna and A. F. Harvey. *Application Note 041 - The Fundamentals of FFT-Based Signal Analysis and Measurement*. National Instruments, July 2000. https://www.sjsu.edu/people/burford.furman/docs/me120/FFT_tutorial_NI.pdf.

[13] H. Chen, D. Lin, S. Tan, and S. Y. Hui. Chromatic, photometric and thermal modeling of led systems with nonidentical led devices. *IEEE Transactions on Power Electronics*, 29(12):6636–6647, Dec 2014.

[14] CIE S 010/E:2004 (ISO 23539:2005). Photometry - The CIE system of physical photometry. Standard, Commission Internationale de L'Eclairage, 2005.

[15] CREE. *Applications for Cree LED Components*. https://www.cree.com/led-components/applications.

[16] Cree, Inc. *Cree XLamp XP-G3 LEDs, Rev 4*, 2019. https://www.cree.com/led-components/media/documents/dsXPG3.pdf.

[17] J. Dong and G. Zhang. Identification and robust control of the nonlinear photoelectrothermal dynamics of led systems. *IEEE Transactions on Industrial Electronics*, 64(3):2215–2225, March 2017.

[18] R. P. Eddy. Design and construction of the 15-ft-beam solar simulator SS15B. Technical report, NASA, Jet Propulsion Lab., Caltech; Pasadena, CA, 1968.

[19] Future Lighting Solutions. *Usable Light Tool 2.4*. `http://www1.futurelightingsolutions.com/ult/default.aspv`.

[20] C. Gueymard. *SMARTS2: a simple model of the atmospheric radiative transfer of sunshine: algorithms and performance assessment*. Florida Solar Energy Center Cocoa, FL, 1995. `http://www.fsec.ucf.edu/en/publications/pdf/fsec-pf-270-95.pdf`.

[21] C. A. Gueymard. *SMARTS code, version 2.9.2 USER'S MANUAL*. Solar Consulting Services, Bailey, CO, March 2003. Retrieved from `https://www.nrel.gov/grid/solar-resource/smarts.html`.

[22] J. W. Harrell and M. J. Largould. The 25-ft space simulator at the Jet Propulsion Laboratory. Technical report, NASA, Jet Propulsion Lab., Caltech; Pasadena, CA, 1969.

[23] IEEE Power Electronics Society. Standards Committee and Institute of Electrical and Electronics Engineers and IEEE-SA Standards Board. *IEEE Std 1789-2015*. IEEE, March 2015.

[24] S. Jang and M. Shin. Thermal optimization of high power led arrays with a fin cooling system. *Optical and Quantum Electronics*, 42(11-13):679–684, 10 2011.

[25] JLCPCB. PCB Prototype & PCB Fabrication Manufacturer. https://jlcpcb.com/.

[26] K. A. Kim, N. Dostart, J. Huynh, and P. T. Krein. Low-cost solar simulator design for multi-junction solar cells in space applications. In *2014 Power and Energy Conference at Illinois (PECI)*, pages 1–6. IEEE, 2014.

[27] A. Kitai. *Principles of Solar Cells, LEDs and Related Devices: The Role of the PN Junction, 2nd ed.* John Wiley and Sons, Ltd, 2018. https://onlinelibrary.wiley.com/doi/abs/10.1002/9781119450986.

[28] D. Kolberg, F. Schubert, N. Lontke, A. Zwigart, and D. Spinner. Development of tunable close match led solar simulator with extended spectral range to uv and ir. *Energy Procedia*, 8:100–105, 12 2011.

[29] R. Koshel. *Illumination Engineering: Design with Nonimaging Optics*. Wiley, 2012. https://books.google.com/books?id=6GiENtLO3eQC.

[30] Laboratory for Atmospheric and Space Physics (LASP), University of Colorado Boulder. LISIRD TSIS-1 Total Solar Irradiance. http://lasp.colorado.edu/lisird/data/tsis_tsi_24hr/.

[31] G. P. Leary. *Comparison of Xenon lamp-based and LED-based solar simulators*. 2016. https://scholarworks.montana.edu/xmlui/handle/1/9837.

[32] LED/Optoelectronics — DigiKey Electronics. *LED/Optoelectronics*. https://www.digikey.com/products/leds-optoelectronics/en/.

[33] LEDSupply. *LEDs*. https://www.ledsupply.com/.

[34] Lumileds. *Lumileds LED Lighting*. https://www.lumileds.com/.

[35] Lumileds. *Luxeon C Color Line*, 2019.
https://www.lumileds.com/uploads/571/DS144-luxeon-c-color-line-datasheet-pdf.

[36] Lumileds. *LUXEON IR Domed Line*, 2019.
https://www.lumileds.com/uploads/685/DS191-luxeon-ir-domed-line-datasheet-pdf.

[37] Luminus Devices. *SST-10-FR Far Red LED, Rev 05*, 2017.
https://download.luminus.com/datasheets/Luminus_SST-10-FR_Datasheet.pdf.

[38] Luminus Devices. *SST-10-UV Surface Mount UV LED, Rev 02*, 2018.
https://download.luminus.com/datasheets/Luminus_SST-10-UV_Datasheet.pdf.

[39] Luminus Devices. *XST-3535-UV Surface Mount UVC LED, Rev 01*, 2019.
https://download.luminus.com/datasheets/Luminus_XST-3535-UV_Datasheet.pdf.

[40] LuxeonStarLEDs. *Luxeon Star High Brightness LEDs.*
https://www.luxeonstar.com/.

[41] Marktech Optoelectronics. *MT03-023 Series 4 Photodiode*, 6 2017.
https://marktechopto.com/pdf/products/datasheet/MT03-023.pdf.

[42] Microchip Technology. *MCP2221A USB 2.0 to I²C/UART Protocol Converter with GPIO*, 2017.
http://ww1.microchip.com/downloads/en/devicedoc/20005565b.pdf.

[43] I. Moreno, M. Avendaño-Alejo, and R. I. Tzonchev. Designing light-emitting diode arrays for uniform near-field irradiance. *Appl. Opt.*, 45(10):2265–2272, Apr 2006.

[44] I. Moreno and C.-C. Sun. Modeling the radiation pattern of leds. *Opt. Express*, 16(3):1808–1819, Feb 2008.

[45] National Instruments. *USB-6008 - 8 AI (12-Bit, 10 kS/s), 2 AO (150 Hz), 12 DIO USB Multifunction I/O Device*, September 2017. `https://www.ni.com/pdf/manuals/375295c.pdf`.

[46] National Instruments. *USB-6009 - 8 AI (14-Bit, 48 kS/s), 2 AO (150 Hz), 13 DIO USB Multifunction I/O Device*, September 2017. `https://www.ni.com/pdf/manuals/375296c.pdf`.

[47] G. Nellis and S. Klein. *Heat Transfer*. Heat Transfer. Cambridge University Press, 2009.

[48] NOAA, US Department of Commerce. Global Monitoring Laboratory - Carbon Cycle Greenhouse Gases, Oct 2005. `https://www.esrl.noaa.gov/gmd/ccgg/trends/gl_data.html`.

[49] NXP Semiconductors. *PCA9685 16-channel, 12-bit PWM Fm+ I^2C-bus LED controller, Rev. 4*, April 2015. `https://datasheetspdf.com/pdf/650892/NXPSemiconductors/PCA9685/1`.

[50] OSRAM Opto Semiconductors. *OSRAM Products*. `https://www.osram.com/cb/products/index.jsp`.

[51] OSRAM Opto Semiconductors. *SFH 2201 TOPLED Silicon PIN Photodiode with Enhanced Blue Sensitivity, Version 1.2*, 12 2019.

https://media.osram.info/media/resource/hires/osram-dam-6303770/SFH+2201_EN.pdf.

[52] G. Rizzoni. *Principles and Applications of Electrical Engineering*. McGraw-Hill Higher Education, 2004.

[53] M. Stuckelberger, B. Perruche, M. Bonnet-Eymard, Y. Riesen, M. Despeisse, F. Haug, and C. Ballif. Class aaa led-based solar simulator for steady-state measurements and light soaking. *IEEE Journal of Photovoltaics*, 4(5):1282–1287, Sep. 2014.

[54] J. Tan, K. Yang, M. Xia, and Y. Yang. Analysis of uniform illumination system with imperfect lambertian leds. *Optica Applicata*, XLI, No. 3, 2011.

[55] Thorlabs. *Light Emitting Diodes (LEDs)*. https://www.thorlabs.com/navigation.cfm?guide_id=2101.

[56] Ushio Opto-Semiconductors Inc. *epitex(R) Spectro Series LEDs*. https://www.ushio.com/product/epitex-spectro-series-leds/?gclid=CjwKCAiAzuPuBRAIEiwAkkmOSKuZqg954KK7HTmzBMZ4FDAKTE5PAAkg_dvPHKTeUoYsfyABfeKlihoCUBMQAvD_BwE.

[57] W. Wang and B. Laumert. *Simulate a "Sun" for Solar Research: A Literature Review of Solar Simulator Technology*. 2014. http://urn.kb.se/resolve?urn=urn:nbn:se:kth:diva-154262.

[58] H. Yang, J. W. M. Bergmans, T. C. W. Schenk, J. M. G. Linnartz, and R. Rietman. Uniform illumination rendering using an array of leds: A signal processing perspective. *IEEE Transactions on Signal Processing*, 57(3):1044–1057, March 2009.

APPENDICES

Appendix A

ASTM E927-19 MEASUREMENT DETAILS

Spectral irradiance measurements must be integrated numerically using the trapezoid method to give a normalization irradiance [7]. The numerical integral over each wavelength interval defined in Table 3.2 on page 17 is computed and divided by the normalization irradiance to give a percentage value. This normalized interval value is divided by the target value for this interval, as computed from ASTM E490-00a data in a similar manner; this ratio is the spectral match for that interval, R_{SM}.

The ASTM E490-00a target percentages are also given in Table 3.2. The spectral match classification of the simulator is determined by the range in Table 3.1 on page 16 which contains all of the calculated R_{SM} values.

The detector cells can be assembled in an array if they are wired such that each cell's short circuit current, I_{SC}, can be measured independently. If an array is used, I_{SC} must be measured for each cell in the array, and normalized to the maximum value to obtain calibration values. A separate monitor cell must be illuminated by the simulator, and its position held constant while each test position has its I_{SC} calculated. These currents are normalized to the I_{SC} of the monitor cell at the time of measurement, and all cells must be maintained at a constant temperature. If a cell array was used, the I_{SC} values at each test position must also be calibrated using the calibration values previously obtained. The test position I_{SC} values are collected into a matrix $\mathbf{I}_S$. Finally, the spatial non-uniformity must be calculated with Eq. 3.2, and visualized with a simple x-y plot of $\mathbf{I}_S$ [7].

To determine temporal instability, t_{DAQ} is divided by a minimum of 20 to determine the required spacing between data points, δt. Additionally, the t_{DAQ} value must be during steady-state, after some defined start-up time has passed to allow the equipment to reach equilibrium [7]. A t_{DAQ} on the order of seconds enables this characterization on a very small time scale, which would ultimately depend on the sampling frequency of the hardware used. A t_{DAQ} on the order of minutes or tens of minutes provides characterization in the temporal range the simulator is most likely to be used. A t_{DAQ} of about an hour provides insight into any longer-term drift that might be present. Regardless of the actual t_{DAQ} used, the rest of the test procedure is the same. A detector solar cell must be mounted in the test plane, and its short-circuit current must be measured while ensuring its temperature remains constant. I_{SC} is then sampled at intervals equal to δt, to obtain an array of measurements, $\mathbf{I}_T$. In a similar fashion as spatial non-uniformity, temporal instability is then calculated as a percentage.

Note that Eqs. 3.2 and 3.3 equate to half of the percent difference between min and max values. This is in contrast to the similar expressions from ASTM E491-73 in App. B [7].

Appendix B

ASTM E491-73 MEASUREMENT DETAILS

In addition to the class A, B, and C requirements outlined in Table 3.3, more stringent classifications are given for solar beam divergence angle, as well as for another characteristic, the change in irradiance with depth, which is measured in $\frac{\%}{m}$ and not defined for class A, B, or C simulators. These higher classifications are denoted as 2A up through 5A, and their requirements are listed below in Table B.1.

Table B.1: ASTM E491-73 2A-5A Solar Simulator Classification [6]

Test Volume Characteristics	**Class 5A**	**Class 4A**	**Class 3A**	**Class 2A**
Solar Beam Divergence Angle	0.125°	0.25°	0.5°	1°
Change in E with depth ($\frac{\%}{m}$)	0.3	0.5	1	2

For measurements of irradiance, ASTM E491-73 recommends maintenance of a reference pyrheliometer to calibrate all other detectors. The standard recommends calibrating this reference instrument using the International Pyrheliometric Scale, maintained by the World Meteorological Organization (WMO). The detector requirements that ASTM E491-73 would impart on a photoelectric detector are that it must

- withstand one solar constant (1353 $\frac{W}{m^2}$)
- have resolution and repeatability of 0.01 solar constant (14 $\frac{W}{m^2}$)
- have a limited field of view to shut out reflected radiation, though it must be larger than the subtense angle of the apparent solar source.

Additionally, the irradiance detector must be measured by a voltmeter that can resolve the signal to 0.1% and has an accuracy of 0.25% of full scale. Selection of an irradiance detector for measurements under vacuum must also take these guidelines into account.

Uniformity of irradiance, E_u, must be measured by a detector whose largest linear dimension is smaller than the smallest part of a test specimen that is relevant to thermal modeling; it is stated that a 2x2 cm solar cell is usually sufficient [6]. Using the guidelines from ASTM E927-19 discussed previously to choose a detector cell size to also characterize the simulator for thermal test articles is acceptable, since the 2.83 mm cell side length derived is more than sufficiently small. The uniformity of irradiance is calculated as a percentage of the mean total irradiance, $\bar{E}$.

During all uniformity of irradiance measurements, a monitor detector must be kept in a constant location to correct for temporal instability. The temperature of all detectors should also be tracked. In addition to reporting the numerical classification of the uniformity, an isoirradiance plot should be produced [6]. The isolines may be absolute irradiance or a percentage of one solar constant. This plot is effectively identical whether [7] or [6] is used, again simplifying the reporting of the results of this work.

For stability of irradiance E_t characterization, measurements must be taken at time intervals corresponding to the thermal time constants of the intended test article. Similarly to Eq. 3.4, a maximum and minimum measured value of irradiance are used to calculate the stability of irradiance.

In Table 3.4 on page 21, four large intervals are defined in the column "Wavelength Interval." If the test article's absorptance varies linearly with wavelength, calculating one ratio for the whole interval is sufficient. If the absorptance has strong peaks or other nonlinear characteristics, these large intervals must be subdivided according

to the column "Number of Bands." A certain number of these subintervals must fall within the overall requirements, listed in the column "Ratio per Bandwidth." Additionally, if it is deemed important, spectrally dependant forms of Eq. 3.4 and 3.6 can be used to determine uniformity and temporal stability of spectral irradiance, respectively.

In wavelength bands appropriate for the desired classification, measurements of spectral irradiance of a standard source should be taken. Using the Standard of Spectral Irradiance maintained by the National Bureau of Standards is recommended. This is a 1000-W incandescent bulb, equivalent to a General Electric DXW-1000 [6]. A transfer function, X, is created from these measurements according to

$$X_\lambda = \frac{S_{\lambda,std}}{E_{\lambda,std}} \tag{B.1}$$

where S_{std} is the measurement of the standard source taken by the spectrometer or equivalent device, and E_{std} is the known spectral irradiance of the standard source. Measurements of the solar simulator's spectral irradiance, S_{SS}, are then converted to the simulator's actual spectral irradiance, E_{SS}, using

$$E_{\lambda,SSI} = \frac{S_{\lambda,SS}}{X_\lambda} \tag{B.2}$$

The spectral irradiance should be remeasured occasionally to monitor any changes; the frequency of such testing depends on the expected decay of the light source's spectrum with time.

Large divergence angles lead to increased innacuracy of shadow geometry. This leads to error in simulating the thermal environment on highly inclined surfaces with significant incidence angles, on test articles with self-shadowing, and on test articles

extending through a significant test volume depth. The required divergence angle classification for these cases is given below in B.2.

Table B.2: ASTM E491-73 Divergence Angle Requirements [6]

Characteristic	**Required Divergence Angle**
Incident Angle	
$\simeq 0°$	C
$< 20°$	B
$20 - 35°$	A
$35 - 55°$	2A
$55 - 70°$	3A
$70 - 80°$	4A
$80 - 85°$	5A
Depth of Irradiated Components	
$< 5\%$ of beam diameter	C
$5 - 10\%$ of beam diameter	B
$10 - 15\%$ of beam diameter	A
$< 1m$	2A
$< 2m$	3A
$< 4m$	4A
$< 8m$	5A
Shadowing Appendages	
$D < 0.2L$	C
$0.2L < D < 0.4L$	B
$0.4L < D < 0.7L$	A
$0.7L < D < 1.4L$	2A
$1.4L < D < 3L$	3A
$3L < D < 6L$	4A
$6L < D < 12L$	5A

At each desired point on the test plane, a minimum of four measurements must be taken to extreme edges of the apparent source, allowing the calculation of the subtense angle at each point. If the source is not symmetrical, this must be used to characterize the smallest and largest subtense angles. If the source does not have sharp edges, these measurements should be taken considering the area from which 95% of the total power issues. For calculation of the divergence angle, a point in the area representing the mean power must be chosen. An example spatial test matrix for a cylindrical test volume has one center point, twelve points at radial distances of $\frac{1}{3}$, $\frac{2}{3}$, and $\frac{3}{3}$ of the beam radius at 0, 90, 180, and 270° azimuthal angle, and four additional points at the edge of the beam at 45, 135, 225, and 315° [6].

The radiation-environment temperature is calculated using the Stefan-Boltzmann equation by solving

$$\varepsilon\sigma T_a^4 = 1.0\sigma T_e^4 \tag{B.3}$$

for T_e, the equivalent blackbody temperature. T_a is the actual chamber wall or shroud temperature, ε is the chamber wall or shroud emittance, and σ is the Stefan-Boltzmann constant. The most significant error as a result of both reflected irradiance and the radiation-environment temperature is felt by inclined surfaces, the requirements of which are shown below in Table B.3.

Chamber pressure must be verified with calibrated gages in accordance with ASTM E926 [6]. It is required that conductive heat exchange with the residual gas be 1% or less of the radiative heat exchange. ASTM E491-73 provides guidelines valid for an 80K shroud, corresponding to liquid nitrogen, and test articles satisfying $\varepsilon D \leq 1.0$, where ε is the emittance and D is the article's characteristic dimension in meters; these are outlined below in Table B.4.

Table B.3: ASTM E491-73 Incidence Angle Requirements[6]

Incident Angle	Reflected Irradiance	Environment Temperature
$\simeq 0°$	C	C
$< 20°$	C	B
$20 - 35°$	B	B
$35 - 55°$	A	A
$55 - 70°$	A	A
$70 - 80°$	A	A
$80 - 85°$	A	A

Table B.4: ASTM E491-73 Pressure Sensitivity Requirements [6]

εD	Temperature	Chamber Pressure
≈ 1	≥ 300 K	Class C ($< 10^{-4}$ torr)
≥ 0.2	≥ 300 K	Class B (10^{-5} torr)
≥ 0.03	≥ 250 K	Class A (10^{-6} torr)

Appendix C

SMARTS2 INPUTS

Refer to the SMARTS2 user's manual [21] for definition of the inputs below, which are the cards read by the SMARTS2 program. Version 2.9.2 was used for this thesis work. Newer versions are available; version 2.9.2 was used here because of its use in ASTM G173.

Settings used to generate the standard AM1.5 reference spectrum in G173 [8]:

```
Card 1      'ASTM_G 173_Std_Spectra'
Card 2      1
Card 2a     1013.25 0.
Card 3      1
Card 3a     'USSA'
Card 4      1
Card 4a
Card 5      1
Card 5a
Card 6      1
Card 6a
Card 6b
Card 7      370
Card 7a     1
Card 8      'S&F_RURAL'
Card 8a
Card 9      0
Card 9a     0.084
Card 10     38
Card 10a
Card 10b    1
Card 10c    38 37. 180.
Card 10d
Card 11     280 4000 1.0 1367.0
Card 12     2
Card 12a    280 4000 .5
Card 12b    2
```

Inputs used to represent conditions during solar cell testing on 9/30/2020 in Oceano, CA:

```
Card 1      '9_30_2020'
Card 2      1
Card 2a     1013.55 0.011
Card 3      0
Card 3a     21.11 15 'Summer' 20.78
Card 4      2
Card 4a
Card 5      1
Card 5a
Card 6      0
Card 6a2
Card 6b
Card 7      410.45
Card 7a     1
Card 8      'S&F_MARIT'
Card 8a
Card 9      0
Card 9a     0.084
Card 10     33
Card 10a
Card 10b    1
Card 10c    18 -999 -999
Card 10d
Card 11     280 4000 1.0 1361.6797
Card 12     2
Card 12a    280 4000 .5
Card 12b    14
Card 12c    1 2 3 4 5 6 7 8 9 10 11 12 13 14
Card 13     1
Card 13a    2 5 0
Card 14     0
Card 14a
Card 15     0
Card 16     0
Card 17     3
Card 17a    2020 9 30 12.33 35.09799468 -120.60181016 -8
Card 17a    2020 9 30 12.73 35.09799468 -120.60181016 -8
```

Inputs used for spatial array photodiode calibration on 11/16/2020:

```
Card 1      'Sunlight Calibration - Spatial Array 11_16_2020'
Card 2      1
Card 2a     1013.377 0.011
Card 3      0
Card 3a     29.2 16 'Winter' 19.12
Card 4      2
Card 4a
Card 5      1
Card 5a
Card 6      0
Card 6a     2
Card 6b
Card 7      413.49
Card 7a     1
Card 8      'S&F_MARIT'
Card 8a
Card 9      0
Card 9a     0.084
Card 10     33
Card 10a
Card 10b    1
Card 10c    18 -999 -999
Card 10d
Card 11     280 4000 1.0 1361.772
Card 12     2
Card 12a    280 4000 .5
Card 12b    9
Card 12c    1 2 3 4 5 9 10 11 14
Card 13     1
Card 13a    2 5 0
Card 14     0
Card 14a
Card 15     0
Card 16     0
Card 17     3
Card 17a    2020 11 16 14.39 35.09799468 -120.60181016 -8
```

Inputs used for feedback board photodiode calibration on 11/16/2020:

```
Card 1      'Sunlight Calibration - Feedback Board 11_16_2020'
Card 2      1
Card 2a     1013.885 0.011
Card 3      0
Card 3a     30.3 12 'Winter' 19.12
Card 4      2
Card 4a
Card 5      1
Card 5a
Card 6      0
Card 6a     2
Card 6b
Card 7      413.49
Card 7a     1
Card 8      'S&F_MARIT'
Card 8a
Card 9      0
Card 9a     0.084
Card 10     33
Card 10a
Card 10b    1
Card 10c    18 -999 -999
Card 10d
Card 11     280 4000 1.0 1361.772
Card 12     2
Card 12a    280 4000 .5
Card 12b    9
Card 12c    1 2 3 4 5 9 10 11 14
Card 13     1
Card 13a    2 5 0
Card 14     0
Card 14a
Card 15     0
Card 16     0
Card 17     3
Card 17a    2020 11 16 13.36 35.09799468 -120.60181016 -8
```

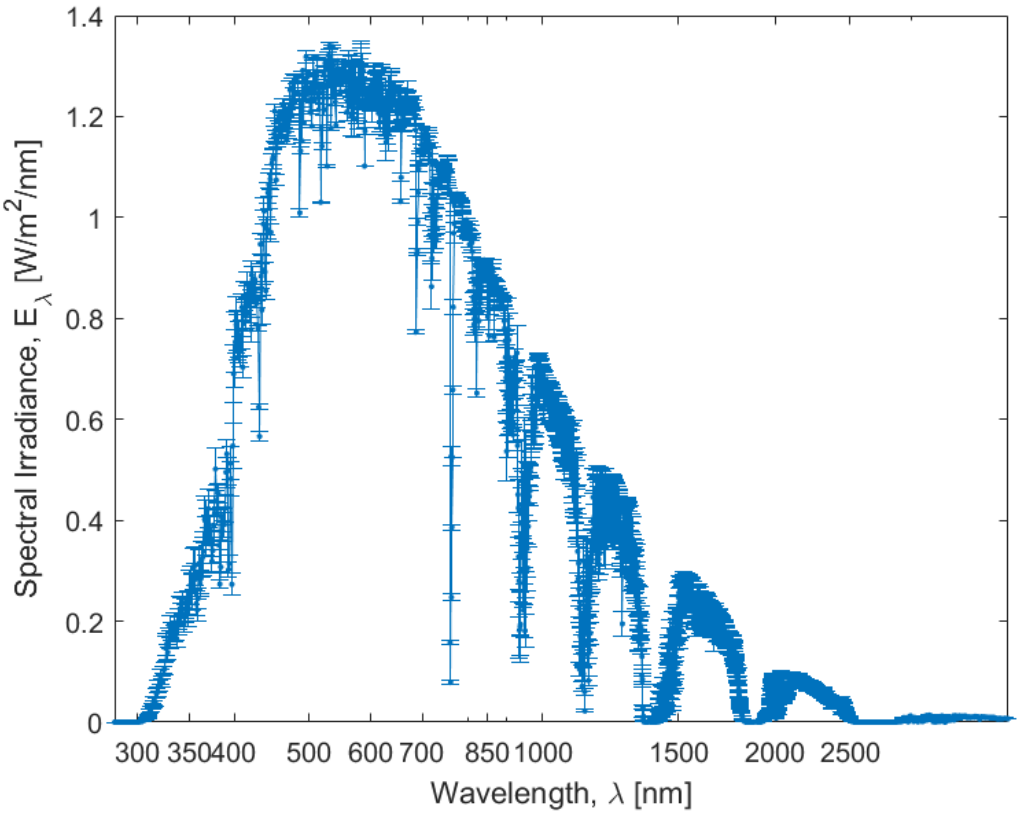

Figure C.1: SMARTS2 Output Used to Calibrate Photodiodes

An example output from SMARTS2 is shown below in Figure C.1, using the *'Sunlight Calibration – Feedback Board* 11_16_2020′ input cards.

The uncertainty in the output of SMARTS2 is discussed in [20]. For the inputs used in this work, the most appropriate estimate of uncertainty was the error in Figure C.2 below.

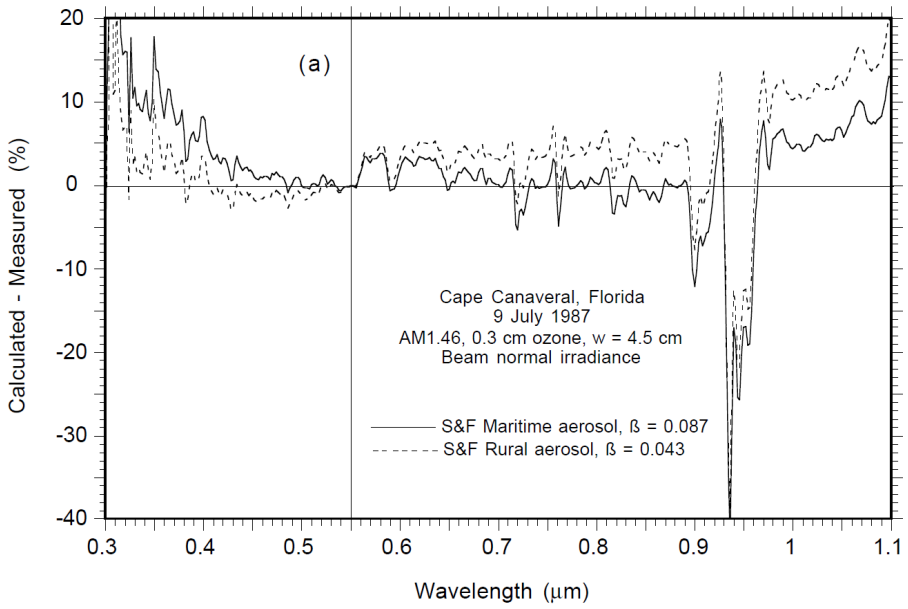

Figure C.2: Percent Difference Between SMARTS2 and Experiments [20]

Appendix D

SIMULATOR OPERATING PROCEDURE

1. Set Up LabView

    1.1 Power on the designated PC.

    1.2 From the desktop, open the "SolarSimulator" folder, then the "LabView" folder.

    1.3 Open the newest version of the VI named "Control_vXX.vi".

    1.4 Ensure all settings are correct on the various tabs.

        1.4.1 "LED Power" should be set to "OFF".

        1.4.2 In the Spectral Analysis tab, "FFT window" should be set to "Hanning," and "Subtract Noise?" should be set to "no".

        1.4.3 In the Control Panel tab, "Manual Ctrl" should be set to "auto," "Python override" should be set to "N," "LED Duty Cycles" should be set to all 0, and "Cmd freq" and "Act freq" should be chosen and calibrated appropriately.

        1.4.4 In the Setup/Debug tab, verify that the paths to "ResistanceMeasurements.xlsx" and the most recent version of "solarism_vXX.py" are correct, and that the toggle labeled "T = all DAQs; F = only DAQ1" is set to "True".

    1.5 In the Control Panel tab, change "Voltage Set Point" to the desired spectrum if different from the average extraterrestrial default.

    1.6 In the Control Panel tab, use the "Save Path" control to select the desired save location for the data files.

2. Set Up Simulator Electrics

    2.1 Verify that the HP 6038A Power Supply is OFF.

    2.2 Verify that the DISCHARGE switch on the capacitor bank is set to ON.

        2.2.1 If it was set to OFF, switch it to ON and wait 1 minute before proceeding.

    2.3 Double-check all electrical connections.

    2.4 Verify that all DAQs show a blinking green LED.

    2.5 Verify that the MCP 2221A USB-C to I2C breakout board displays a solid green LED.

    2.6 Set up any test articles.

    2.7 Place the shielding box over the simulator.

    2.8 Position the IR lamp in the hole in the array board above the test plane.

    2.9 All individuals in the room must don eye-protecting PPE.

        2.9.1 Any individuals who will be manipulating test articles while the simulator is illuminating the test plane must also don long sleeves and gloves to cover any exposed skin.

3. Run Simulator (NOTE: THE SOFTWARE RECORDS AT 10kHz – ENSURE ALL PARTICIPANTS ARE PREPARED TO PROCEED EFFICIENTLY TO AVOID UNNECESSARILY LARGE DATA FILES)

    3.1 Press LabView's "Run" button in the upper left toolbar.

    3.2 Enter a name for the data files from this run, then select "OK" to continue.

    3.3 All plots and values should begin updating.

    3.4 Set the DISCHARGE switch on the capacitor bank to OFF.

3.5 Turn ON the HP 6038A Power Supply (It should default to CURRENT control on startup) (refer to Figure D.1 for an image of the front panel display).

3.5.1 Check that CURRENT is selected in the OUTPUT ADJUST section on the bottom right of the front panel (The LED next to CURRENT should be lit).

3.5.2 While holding down the DISPLAY SETTINGS button to the bottom left of the digital output display, use the OUTPUT ADJUST knob to increase the max current setting to 10 Amps, then release the DISPLAY SETTINGS button.

3.5.3 Press the button in the OUTPUT ADJUST section to switch to VOLTAGE control mode (The LED next to VOLTAGE should light up).

3.5.4 While holding down the DISPLAY SETTINGS button to the bottom left of the digital output display, use the OUTPUT ADJUST knob to increase the voltage to 30 Volts, then release the DISPLAY SETTINGS button.

3.6 Check that the power supply's readout displays at least 30.0 V, and that the "Vs" graph display on the Output tab in LabView also reads close to 30 V (ideally 29.8-29.9).

3.7 Wait a second or two to ensure the power supply has stabilized.

3.8 Note the current time in LabView (displayed on every graph with time on the x-axis) so it is easy to identify this point in the data later.

3.9 Turn on the IR Lamp.

3.10 Wait 10 seconds so that there is plenty of data to calculate a start-point reading of the baseline voltage of the photodiodes when analyzing the results later.

3.11 Toggle the "LED Power" switch to ON within LabView. The simulator will begin increase the duty cycle of the LEDs to match the voltage set point.

3.12 Wait for the duty cycle to stabilize (should take around 1 minute).

3.13 Acquire desired data from test articles.

4. Shut Down Simulator

4.1 Once testing is complete, toggle the "LED Power" switch to ON within LabView. The LEDs should switch off within 1 second.

4.2 Note the current time in LabView (displayed on every graph with time on the x-axis) so it is easy to identify this point in the data later.

4.3 Wait 10 seconds to allow the data readings to stabilize and provide an end-point reading on the baseline voltage of the photodiodes.

4.4 Turn off the IR Lamp.

4.5 Switch off the HP 6038A Power Supply.

4.6 Set the DISCHARGE switch on the capacitor bank to ON.

4.7 Wait 1 minute, monitoring the Vs graph reading on the Output tab in LabView to ensure the voltage has dropped down to about 0.1 Volts and is no longer decreasing.

4.8 Toggle the "STOP (Esc)" button in LabView to stop recording data.

4.9 All test participants may now doff eye-protecting PPE.

4.10 Remove the shielding box from the simulator.

4.11 Remove any test articles.

4.12 Repeat from 2.6 if any other tests are to be conducted.

Figure D.1: HP 6038A DC Power Supply Front Panel